Integrated Optical Interferometric Sensors on Silicon and Silicon CMOS

A Dissertation
Presented to
The Academic Faculty

By

Mikkel A. Thomas

In Partial Fulfillment
Of the Requirements for the Degree
Doctor of Philosophy in the
School of Electrical & Computer Engineering

Georgia Institute of Technology
December 2008

Integrated Optical Interferometric Sensors on Silicon and Silicon CMOS

Approved by:

Dr. Nan Marie Jokerst, Advisor
School of Electrical & Computer Engineering
Duke University

Dr. Joy Laskar, Co-Advisor
School of Electrical & Computer Engineering
Georgia Institute of Technology

Dr. Alan Doolittle
School of Electrical & Computer Engineering
Georgia Institute of Technology

Dr. Stephen Ralph
School of Electrical & Computer Engineering
Georgia Institute of Technology

Dr. Thomas Michaels
School of Electrical & Computer Engineering
Georgia Institute of Technology

Dr. Clifford Henderson
School of Chemical & Biomolecular Engineering
Georgia Institute of Technology

Date Approved: September 29, 2008

This work is dedicated to my parents, Jimmie and Mary Thomas, who always believed in me and supported me at my highest and lowest moments. Without them, I would have never known I could accomplish what I have.

Acknowledgements

I would like to express my appreciation and gratitude to my thesis advisor, Dr. Nan Marie Jokerst, for her support during my tenure at Georgia Tech. I would also like to thank my committee members, Dr. Joy Laskar, Dr. Alan Doolittle, Dr. Thomas Michaels, Dr. Stephen Ralph, and Dr. Clifford Henderson for giving their time and experience. I would also like to thank my parents, Jimmie and Mary Thomas for their never wavering support during my time here. I would also like to thank the staff and students of the Mircoelectronics Research Center Cleanroom for their tireless efforts. Finally, I would like to thank the past and present members of the Integrated Optoelectronics Research Group as well as the students of the BOSS research project. Without their counsel and support, this work would have never been completed.

Table of Contents

List of Tables

List of Figures

List of Abbreviations

1. ADC – Analog-to-digital converter
2. ALDS – Apollo Photonics laser diode simulator
3. APSS – Apollo Photonics solutions suite
4. BCB – Benzocyclobutene
5. BER – Bit error rate
6. BJT – Bipolar junction transistor
7. CCD – Charge coupled device
8. CMOS – Complementary metal-oxide semiconductor
9. CW – Continuous wave
10. FFT – Fast Fourier transform
11. GRINSCH – Graded-index separated-confinement heterostructure
12. HFAPNB - Bis-trifluoromethyl carbinol-substituted polynorbornene
13. ICP – Inductively coupled plasma
14. I/O – Input/Output
15. LI – Intensity vs. current
16. MFC – Mass flow controller
17. MOVPE – Metal organic vapor phase epitaxy
18. MSM – Metal-semiconductor-metal
19. MQW – Multiple quantum well
20. MZI – Mach-Zehnder interferometer
21. NRZ – Non-return-to-zero

22. OEIC – Optoelectronic integrated circuit

23. PECVD – Plasma enhanced chemical vapor deposition

24. PPBV – Parts per billion vapor

25. PPMV – Parts per million vapor

26. QCM – Quartz crystal microbalance

27. PRBS – Pseudorandom binary (bit) stream

28. PSG – Phosphosilicate glass

29. RIE – Reactive ion etcher

30. RMS – Root mean square

31. RTP – Rapid thermal processing

32. SCCM – Standard cubic centimeter

33. SCH – Separate confinement double heterostucture

34. Si – Silicon

35. SNR – Signal-to-noise ratio

36. TCE - Trichloroethylene

37. TE – Transverse electric

38. TIR – Total internal reflection

39. TM – Transverse magnetic

40. ULTEM – Polyetherimide

41. VCSEL – Vertical cavity surface-emitting laser

42. VLSI – Very large-scale integration

43. WFC – Wedge-induced facet cleaving

Summary

The main objective of this research is to fabricate and characterize an optically integrated interferometric sensor on standard silicon and silicon CMOS circuitry. An optical sensor system of this nature would provide the high sensitivity and immunity to electromagnetic interference found in interferometric based sensors in a lightweight, compact package capable of being deployed in a multitude of situations inappropriate for standard sensor configurations. There are several challenges involved in implementing this system. These include the development of a suitable optical emitter for the sensor system, the interface between the various optically embedded components, and the compatibility of the Si CMOS with heterogeneous integration techniques. The research reported outlines a process for integrating an integrated sensor on Si CMOS circuitry using CMOS compatible materials, integration techniques, and emitter components.

Chapter 1

Introduction

The main objective of this research is to fabricate and characterize an integrated optical interferometric sensor on standard Si CMOS circuitry. An optical sensor system of this nature would provide the high sensitivity and immunity to electromagnetic interference found in interferometric based sensors in a lightweight, compact package capable of being deployed in a multitude of situations inappropriate for standard sensor configurations. There are several challenges involved in implementing this system. These include the development of a suitable optical emitter for the sensor system, the interface between the various integrated optical components, and the compatibility of the Si CMOS with heterogeneous integration techniques. The research detailed herein examines a process for integrating an embedded sensor on Si CMOS circuitry using CMOS compatible materials, integration techniques, and emitter components.

1.1 Dissertation Methodology

The integrated sensor system consists of an optical emitter launched directly into a SiO_2/Si_3N_4 interferometer through an integrated waveguide. Signals from the output waveguide are detected by CMOS detectors fabricated as part of the Si CMOS circuit. Signal processing of the detected interferometric pattern is performed by on-chip analog-to-digital converters in the CMOS circuit. The integrated optical emitter consists of a thin-film edge emitting laser. Experimentally, the research concentrates on the development of the thin-film laser, the characterization of the optical interface of the integrated structures, and the integration of the laser and sensor components onto the

CMOS circuitry. The research also examines the theoretical performance of a sensor of this type.

A modular approach was used to design the integration sequence for the sensor. Each of the optical components was developed and tested independently before integration. The research was broken down into the following areas: 1. Development of the thin-film edge emitting laser; 2. Development of the waveguiding structures; 3 Development of thin-film laser integrated with a waveguide structure; 4. Integration of waveguide structures on Si CMOS; 5. Integration of the sensor on the Si CMOS; 6. Test of the integrated sensor/circuit; 7. Examination of theoretical results vs. experimental results.

A standard quantum well structure was used for the laser material. A layer of AlAs was grown between the growth substrate and the laser structure. This selective etch layer was used to separate the laser epilayer from the substrate during the thin-film process. Standard photolithography methods were used to pattern laser bars on the wafer. The bars were isolated in a mesa etch and the substrate was removed by laterally etching through the AlAs sacrificial layer. A modified version of the wedge-induced facet cleave method was used to cleave the bars into individual devices. The lasers were placed on a transfer diaphragm, where they were transferred to various substrates for testing and integration. Individual lasers were characterized in terms of threshold current, output power, efficiency, and spectral characteristics.

Waveguiding layers consisting of silicon dioxide cladding layers and a silicon nitride core layer were deposited on silicon substrates. Core layer thickness was varied based upon to the requirements of the sensor integration. Test waveguide structures and

interferometers were fabricated from these substrates. The test waveguides were used to characterize the loss found in the waveguides using the optical fiber scanning method. The interferometers were tested using a commercial laser and a CCD camera array to characterize their performance. Interferometric sensors were constructed and their operation has been tested and verified.

Upon completion of laser development and waveguide characterization, a process suitable for Si CMOS integration was developed for the waveguide, sensor, and laser integration process. The effects of integrating the laser with a waveguide structure were examined, as well as the coupling efficiency between the laser and the waveguide. A basic model of this interface was developed.

In a parallel effort, waveguides were integrated with Si CMOS VLSI circuits. During the integration, care was taken since the waveguide structures were constructed using some of the same materials (e.g. SiO_2) used in the circuit fabrication. Very precise etch steps were developed in order to avoid over etching the circuit, and thus, damaging electrical components during the waveguide fabrication. It was also necessary to protect exposed circuit components such as the input/output (I/O) pads in order to ensure that they were not damaged during integration. To address this issue, all sensitive components on the circuit were protected underneath a sacrificial polymer layer. This layer allowed components to be protected, while enabling easy removal of the polymer layer upon completion of the integration. Upon successful completion of these steps, circuit performance after integration was characterized. Light was launched into the waveguides using a commercial laser and the onboard Si CMOS detectors were used to

detect the optical output signal from the waveguides. Detector responsivity was characterized and overall circuit performance was evaluated.

The work proposed above involved several graduate students working together. Each student was responsible for a different area integral to the project. The division of labor this project can be seen in Table 1.

Table 1 Division of labor for the interferometric sensor project among the graduate students.

Students	Affiliated Professor	Tasks
Mikkel A. Thomas	Dr. Nan Marie Jokerst	1. All heterogeneous integration processes a. Interferometer on Si b. Interferometer on Si CMOS c. Emitter on Si embedded in interferometer d. Emitter on Si CMOS embedded in interferometer 2. Simulation of coupling in and out of interferometer/sensor 3. Thin-film laser development and testing 4. Theoretical vs. experimental analysis for coupling from optoelectronic and optical devices 5. Interferometer test and development 6. Test setup 7. Interferometric circuit testing
Jeffrey Lillie	Dr. Stephen Ralph	1. Interferometer sensor simulation 2. Interferometer test and development 3. Test setup 4. Test chamber development 5. Interferometric sensor testing
Karla Dennis Benita Comeau	Dr. Clifford Henderson	1. Chemical sense layer development and characterization 2. Test setup – chemical delivery system 3. Interferometric sensor testing

Table 1 Continued		
Dae-Ik Kim	Dr. Martin Brooke	1. CMOS photodetectors 2. Si CMOS circuit design and development 3. Circuit testing 4. Interferometric sensor testing

1.2 Dissertation Outline

This dissertation investigates the feasibility of an interferometric biological/chemical sensor using heterogeneously integrated optoelectronic and optical components.

Chapter 2 examines integrated sensor technology. This chapter is divided into two main sections. One section looks at the thin-film laser, while the second section investigates hybrid optoelectronic and waveguiding technology in sensors. The chapter begins by looking at the underlying theory behind the semiconductor laser. A closer examination is then performed on gain-guided multiple quantum well lasers. Emphasis is placed on the gain mechanism of the lasers and the threshold current calculations. Concluding the laser section is an overview of the current state of relevant laser technology. The second section starts with a brief overview of basic waveguiding theory. It then continues with a review of previous reports dealing with the integration of waveguides with Si CMOS technology. It concludes with a review of heterogeneous integration of optoelectronic devices with waveguides.

Chapter 3 reviews interferometric sensor technology. The underlying theory behind an interferometric sensor is reviewed. This review is followed by an examination

of the Hartman biosensor. This sensor exemplifies the fundamental design that was employed in this work.

Chapter 4 examines the design, fabrication, and performance of the technologies used in the sensor fabrication. The design decisions for the interferometric sensors are discussed, and the performance of the resulting devices is examined. Testing methodologies for the sensors are also outlined. Thin-film laser design is then discussed, followed by an examination of the results measured after fabrication. An overall integration scheme for the sensor system is also detailed and evaluated.

Chapter 5 is a theoretical examination of the feasibility of the sensor outlined in this work. The first section examines the semiconductor lasers of this work theoretically. The laser model used to simulate the laser devices is presented in detail. The results of this model are reviewed and discussed. These results are then compared with the experimental results detailed in Chapter 4. The second section looks at coupling between the thin-film lasers and the interferometric structure. The governing equations behind this analysis are presented and the results obtained from the model are discussed.

Chapter 6 completes the thesis with the overall conclusions from the work and some future directions for this research.

Chapter 2

Integrated Sensor Circuit Technology

Hybrid optoelectronic integrated circuits (OEICs) combine optical components such as lasers and detectors with separate electronics such as Si CMOS. By separating these components from each other, each component can be adjusted to deliver optimal performance. OEICs have been shown to have an important role in the future of optical transmission and data processing systems. OEICs provide low noise, high-speed operation because parasitic inductances and capacitances associated with wire bonding and wiring are significantly lower than current technology. OEICs also lend themselves to low-cost mass production because of their reproducibility, reliability, and compactness. These characteristics lend themselves ideally to sensor design. Sensors have typically been slow and high noise systems. By integrating optical components with Si CMOS photodetectors and analog-to-digital converters (ADCs), a fast, low noise, high sensitivity sensor can be realized. The main hindrance to the development of OEICs is the development of an integration scheme that can account for the inherent structural and technological differences between the individual components.

Optical structures integrated onto circuits must possess a fabrication process that is compatible with the circuitry. For example, any high temperature step involved in the integration of a waveguide must fall within the thermal process tolerance of the circuits. For this reason, any optical structure used should be relatively simple to fabricate and require no processing steps that would damage the host substrate upon which they are

being integrated on. Active optical devices should also be designed to minimize their power consumption and heat dissipation.

An optical interferometric sensor would present several difficulties in its realization as an OEIC. The implementation of the sensor can be broken down into two main challenges. A suitable optical source has to be developed. For this research, a thin-film edge emitting laser is being used. Additionally, an integration scheme for the waveguide and sensor on the Si CMOS must also be developed. An understanding of the interfaces and interactions between the active components and the interferometer has to be achieved. The following section reviews the current trends involving these pertinent areas.

2.1 Thin-Film Lasers

2.1.1 Semiconductor Laser Device Operation

The underlying principle behind semiconductor lasers is the p-n junction. In its simplest form the p-n junction consists of a p-type material in contact with an n-type material. When the materials are separate, the Fermi levels of these two materials do not match due to the difference in carrier concentration between the two materials. In order to accommodate this difference in the Fermi levels, holes diffuse across the junction from the p-type material to the n-type material, while electron will diffuse from the n-type material to the p-type material. These diffusing electrons and holes combine in the junction between the materials, until a steady state condition is reached in the material. An internal electric field in the depletion region causes a drift current that opposes the diffusion current between the two materials. At this point, the Fermi level is flat. The

energy band structure for a p-n junction of a single material composition can be seen in Figure 1.

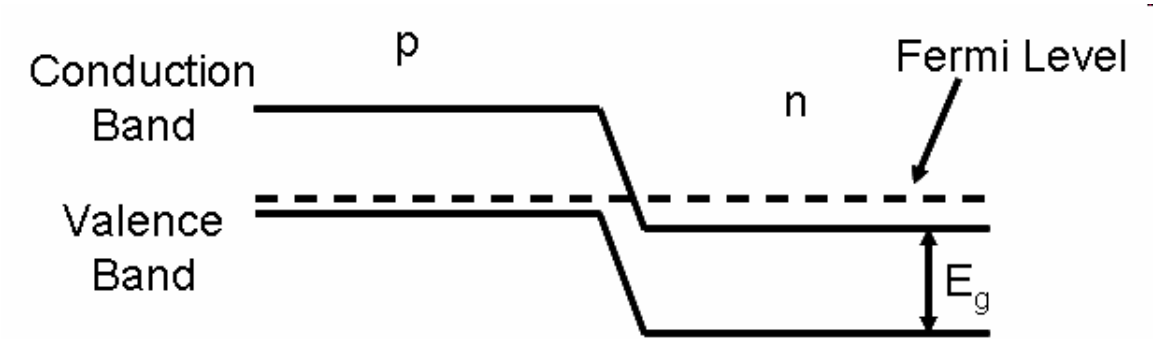

Figure 1. Energy band diagram of a p-n junction at zero bias

By applying a positive electrical voltage to the p side of the junction relative to the n side, the internal electric field can be reduced. This reduction in the electrical field allows the diffusion of carriers between the two materials. Again, some of the carriers will recombine in the junction. Some of the holes and electrons will recombine radiatively; the energy of their recombination is released in the form of a photon. The photons will have energy E_g, where E_g is the energy difference between the conduction and valence bands of the material. Some of these photons are emitted as light, while other photons are reabsorbed into the material, producing further electron-hole pairs. When the probability of the stimulated emission exceeds the probability of absorption, the condition known as population inversion occurs. This condition is a condition for lasing in semiconductor lasers. When population inversion occurs, the quasi-Fermi level separation exceeds the band gap energy of the structure, $E_{fn} - E_{fp} \geq E_g$. This is known as the Bernard-Duraffourg relationship. [1] The laser structure wil then experience optical gain in the energy range from E_g to $E_{fn} - E_{fp}$.

The relationship between the emission wavelength and the energy is given by the equation below, where h is Planck's constant, c is the speed of light, and E is the band gap energy.

$$\lambda = \frac{hc}{E} \qquad [1]$$

For p-n junction constructed of similar materials, population inversion can be difficult as carrier can move through the junction easily from one side to the other due to the similar band structures. In order to confine the electrons in the conduction band and the holes in the valence band to the depletion region better, a junction of dissimilar materials, called a heterostructure, can be constructed. The energy band structure of this material can be seen in Figure 2. Under forward bias, carries will diffuse into the junction, but they can not easily diffuse into the other side due to the large potential barrier due to differences between the band gaps of the two materials. This double heterostructure junction under forward bias can be seen in Figure 3. The presence of larger quantities of carriers in the junction increases the probability of radiative recombination between holes and electrons and makes population inversion easier to achieve.

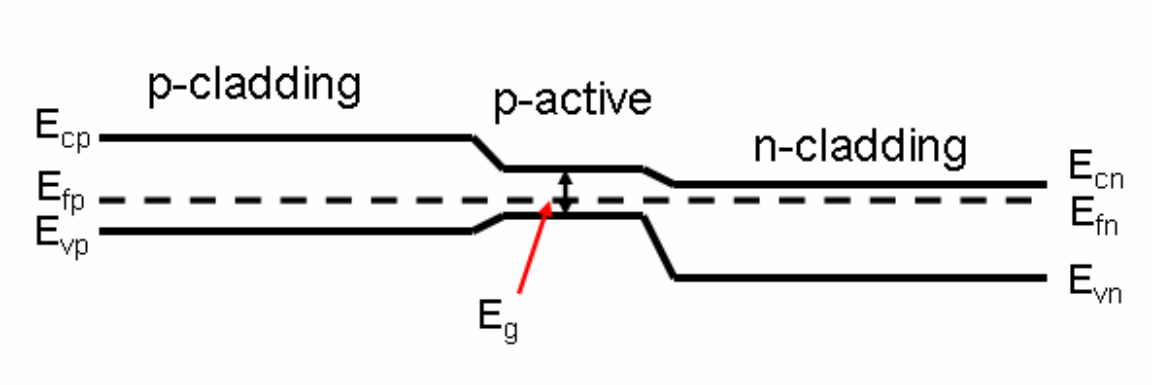

Figure 2 Energy band diagram of a double heterostructure semiconductor laser under zero bias.

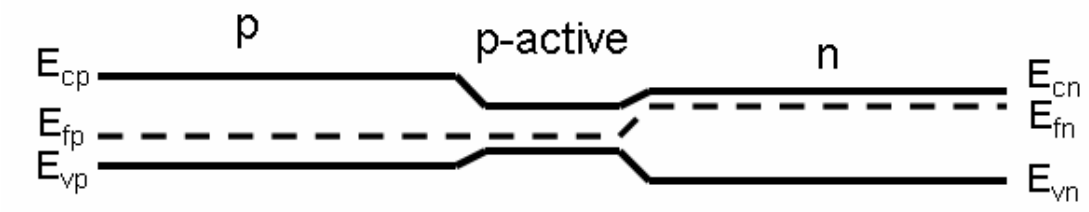

Figure 3 Energy band diagram of a double heterostructure semiconductor laser under forward bias.

2.1.1.1 Gain-Guided Multiple Quantum Well Semiconductor Lasers

One of the most common laser structures fabricated is the gain-guided semiconductor laser. Unlike broad area contact lasers, which inject current over the entire surface of the semiconductor structure, gain-guided lasers restricts the injection of electrical current to a small region along the junction plane of the laser. This small change in laser design has several important advantages. [2] By injecting current into a small area, the threshold current is greatly reduced, even during continuous wave (CW) operation in comparison to broad area lasers. The lower operating current leads directly to a lower operating temperature. Temperature is an important consideration due to the negative impact that high temperatures can have on laser operation. The heat is generated by the nonradiative recombination of caries in the laser structure. [3, 4] This

recombination is enhanced at the laser facets due to surface recombination. There are more recombination regions in the facets of a semiconductor laser due to mechanical stress from cleaving and thermal stress during laser operation. [5] As the heat increases in the laser, the band gap will shrink. The reduction in band leads to in increase of the absorption coefficient of the laser. An increase in the absorption coefficient will lead to a further increase of the recombination current in the laser, and thusly, more heat. At some temperature T_o, this feedback mechanism becomes catastrophic to the laser operation and the temperature will cascade out of control. This condition is known as thermal runaway and it can actually lead to the facets of the laser melting due to the high recombination current in these regions. Cooling while still essential for some laser operation, should be avoided if possible since it adds to the system cost. The decreased heat stress on the laser also leads to a longer device lifetime and reliability. [6-8] Lifetime and reliability are two factors that have to be considered when deploying any system.

The fabrication of a gain-guided laser can be relatively simple. In its simplest implementation, the p-side of the semiconductor is masked with an insulating material, such as silicon dioxide or a polymer. A via is then etched in this insulation layer down to the semiconductor in order to create a stripe contact. The stripe is on the order of a few tens of microns. A broad area contact can then be applied, contacting the semiconductor only in the stripe region. A broad area contact is applied to the n-side of the semiconductor to complete the fabrication. This design can be seen schematically in Figure 4. Other gain-guided laser designs have been implemented to more tightly confine the current injection into the laser structure. [9-11] These structures restrict current spreading in the laser through novels means such as ion implantation.

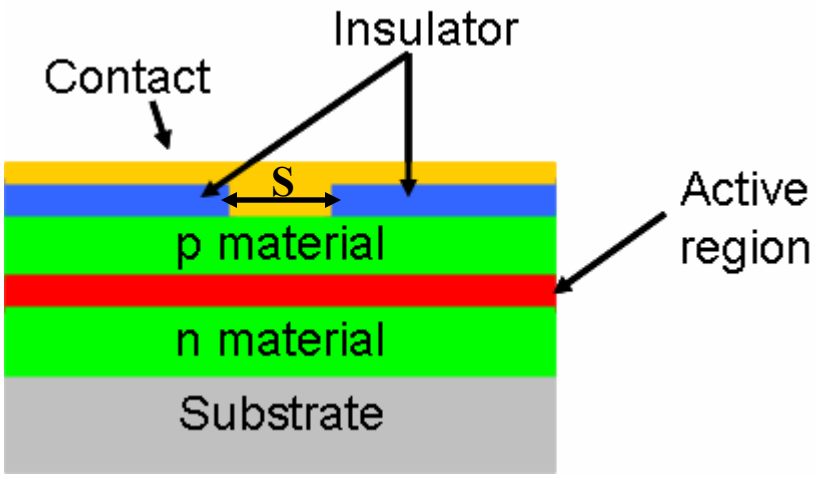

Figure 4 Simple gain-guided laser schematic.

Current injected into a gain-guided laser spreads along the lateral direction of the device. Accordingly, the carrier distribution within the laser is related directly to the current spreading. Thus, the pumped gain region within the laser is larger than the size of the stripe and is nonuniform across the width of the laser. This nonuniformity provides the guiding mechanism for the optical mode confinement in the lateral direction. Since the carrier distribution is nonuniform, the optical lasing mode will only exist in regions where the carrier density is sufficient enough to support stimulated emission. The injected current density of a gain-guided laser can be approximated by the following equation

$$J(y) = \begin{cases} J_0 & |y| \le S/2 \\ J_0 e^{-K(|y|-S/2)} & |y| \ge S/2 \end{cases} \qquad [2]$$

In this equation, y is the lateral position of interest and S is the size of the laser stripe, as seen in Figure 4. K is a factor which accounts for the current spreading within the structure. This equation indicates that the current density is uniform directly under the center of the stripe. At a distance of S/4 from the center in either direction, the density begins to spread and decay exponentially. The speed of this decay is determined by the current spreading factor K.

The carrier distribution within the laser is defined as

$$n(y)=\begin{cases} N_0\left[1-\dfrac{KL_n}{1+KL_n}e^{-S/2L_n}\cosh\left(\dfrac{y}{L_n}\right)\right] & |y|\le S/2 \\ \dfrac{N_0}{1+KL_n}\left[-KL_n\left(e^{-S/2L_n}\cosh\left(\dfrac{S}{2L_n}\right)+\dfrac{KL_n}{1-KL_n}\right)e^{-\left(|y|-S/2\right)/L_n}+\dfrac{1}{1-KL_n}e^{-K\left(|y|-S/2\right)}\right] & |y|\ge S/2 \end{cases} \quad [3]$$

where L_n is the diffusion length of the carriers. This equation may be simplified if current spreading outside the stripe region is ignored. Current spreading outside the stripe region is small and has a marginal impact on the overall carrier distribution. By ignoring its effect, a more compact and usable equation can be realized without sacrificing much in accuracy. Under these conditions, the spreading factor, K, would approach infinity. The carried distribution function would then simplify to

$$n(y) = N_0 \begin{cases} \left[1 - e^{-S/2L_n} \cosh\left(\frac{y}{L_n}\right)\right] & |y| \le S/2 \\ \sinh\left(\frac{S}{2L_n}\right) e^{-|y|/L_n} & |y| \ge S/2 \end{cases} \quad [4]$$

2.1.1.2 Optical Gain in Gain-Guided Multiple Quantum Well Lasers

In this research, the lasers that are implemented are multiple quantum well (MQW) lasers. Most early semiconductor lasers were double heterostructure devices. These structures consist of a single material active layer region (0.1-0.3 μm) sandwiched between two cladding layers which have a larger band gap than the active region. When the active region thickness of a laser approaches the de Broglie wavelength ($\lambda \cong$ h/p), the structure begins to exhibit quantum mechanical effects. These quantum mechanical effects will have a large impact on the absorption and the emission characteristics of the laser, as well as the carrier movement throughout the device. [12-14]

Several theoretical models have been employed to describe how gain is governed in MQW lasers. [15-17] The model detailed by Kasemset et al. is an appropriate model when considering the laser structures detailed in this work. [18] In all quantum lasers, the energy levels for the electrons and holes in the valence and the conductions bands becomes quantized as the quantum well width, L_z, approaches the order of the de Broglie wavelength. These energy levels can be found by solving the eigenvalue equation

$$\left[\frac{m_2}{m_1}\left(\frac{V - \Delta E_n}{\Delta E_n}\right)\right]^{1/2} = \tan\left(\frac{m_1 \Delta E_n L_z}{2\hbar^2}\right)^{1/2} \quad [5]$$

where V is the finite potential barrier, ΔE_n is the quantized energy of the nth level measured from the band edge, m_1 is the effective mass of the carriers in the well, and m_2

is the effective mass of the carriers in the barriers. Assuming simple parabolic bands with infinite barriers, the density of states in the conduction band can be derived as

$$\rho_c(E) = \frac{m_c}{\pi\hbar^2 L_z}\left[Int\left(\frac{E - E_c}{\Delta E_{l,c}} \right)^{1/2} \right] \qquad [6]$$

where $\Delta E_{l,c}$ is the energy difference between the lowest confined electron state and the conduction band edge, m_c is the effective mass of the carriers in the conduction band, and Int(x) is the integer function. The total electron density, n, in the quantum well structure can be found by summing over all the discrete subbands in the energy band structure, and is identified in equation 7.

$$n \approx \frac{4}{\sqrt{\pi}}\left(\frac{m_c kT}{2\pi\hbar^2} \right)^{3/2}\left(\frac{\Delta E_{l,c}}{kT} \right)^{1/2} \sum_{n=1}^{\infty} \ln\left[1 + e^{\frac{F_n - E_{n,c}}{kT}} \right] \qquad [7]$$

where F_n is the quasi-Fermi level, k is the Boltmann constant and T is the temperature. A similar procedure can be performed to define the hole density of the quantum well

The optical gain of the quantum well for band-to-band recombination with the k selection rule can be given by [19]

$$g(E) = \frac{\pi\hbar c\mu e^2}{nm^2 E}|M|^2 \rho_{red}(E)\left(f_c - f_v \right) \qquad [8]$$

where $|M|^2$ is the matrix element for optical transitions, $\rho_{red(E)}$ is the reduced density of states for one direction of spin, μ is the electron mobility. and f_n and f_p are the occupational probabilities for the conduction and valence bands given by [20]

$$f_c(E) = \frac{1}{1 + e^{\frac{(E - F_n)}{kT}}}$$

$$f_v(E) = \frac{1}{1 + e^{\frac{(E - F_p)}{kT}}} \qquad [9]$$

Gain occurs in the quantum well structure when $f_c > f_v$. Under these conditions, population inversion occurs and lasing begins within the structure.

2.1.1.3 Threshold Current in Gain-Guided Multiple Quantum Well Lasers

Threshold current is one of the most important physical characteristics of semiconductor lasers. The current necessary for powering a semiconductor laser has a direct impact on the power budget of the optoelectronic system the laser is being used in. When designing a laser, it is important to ensure that the structure designed has a threshold current that falls within specifications of the desired power budget. The threshold current of a semiconductor laser can be given by [21]

$$I_{th} = \frac{wLn_w J_0}{\eta} e^{\left[\frac{1}{n_w \Gamma_w g_0}\left(\alpha + \frac{1}{2L}\ln\frac{1}{R_1 R_2}\right) - 1\right]} \qquad [10]$$

In this equation, w is the width of the contact stripe, L is the length of the cavity, n_w is the number of the wells, η is the internal quantum efficiency of the injection current, J_0 is the initial current density in the quantum well, Γ_w is the optical confinement factor per well, g_0 is the initial gain in the quantum well structure, α is the internal optical loss, and R_1 and R_2 are the mirror reflectivities of the respective facets.

From this equation, it can be determined that the cavity length of the laser has a large impact on the threshold current of the laser. Due to it presence in the first term of

equation 10, it can be seen that the threshold increases linearly with the cavity length. By the same token, the exponential term decreases with increasing cavity length. These two conditions result in an optimal cavity length, L_{opt}, which will minimize the threshold current of the laser given by [21]

$$L_{opt} = \frac{1}{2}\frac{1}{n_w \Gamma_w g_0}\ln\left(\frac{1}{R_1 R_2}\right) \qquad [11]$$

A similar dependency can be explored for the number of well in the quantum well structure. If the assumption is made that the device parameters in equation 11, such as loss, efficiency, optical confinement, initial gain, and initial current density are independent of quantum well number, then minimum threshold current can be achieved when n_w is given by [21]

$$n_{opt} = \frac{1}{\Gamma_w g_0}\left[\alpha + \frac{1}{2L}\ln\left(\frac{1}{R_1 R_2}\right)\right] \qquad [12]$$

By using equations 11 and 12, it is possible to design a MQW laser with a low threshold current, and thus low power consumption in the system.

2.1.2 Reported ELO Thin-Film Lasers Research

A few groups have completed work in the area of thin-film lasers formed by separating an epitaxial laser from the growth substrate. Concerns regarding performance degradation, material handling, and the formation of the mirrored facets on the lasers have made this approach particularly challenging. [22-26] For example, one of two design choices can be made when forming the laser facets. The facets can be formed prior to substrate removal or the facets can be formed after substrate removal. Cleaving thin-film devices has proven difficult because of the fragile nature of the devices. Similarly, cleaving the devices before the substrate is removed also suffers from

challenges. Once the lasers are cleaved and the facets are formed, the resultant devices are so small that subsequent processing steps become complicated. The majority of the reported research discusses the design choices made and the fabrication of the lasers.

	Layers	Thickness (μm)
7	p^+ - GaAs	0.2
6	p - $Al_{0.30}Ga_{0.70}As$	1.5
5	GaAs	0.2
4	n - $Al_{0.30}Ga_{0.70}As$	1.5
3	n^+ - GaAs	1.5
2	AlAs	0.05
1	GaAs Substrate	

Figure 5 Layer structure of the first demonstrated thin-film laser. The laser was a double heterostructure.

The first reported thin-film laser was epitaxially lifted-off and was reported by Yablonovitch *et al*. in 1989. [25] In this work, a GaAs/AlGaAs double heterostructure laser was grown on a GaAs substrate. A sacrificial layer of AlAs was grown between the laser and the substrate. All of the laser fabrication steps were performed before substrate removal. P-type metal contacts were patterned on the top of the laser (TiAu). A trench was then etched down to the n-type contact layer of the laser using $H_2SO_4/H_2O_2/H_2O$

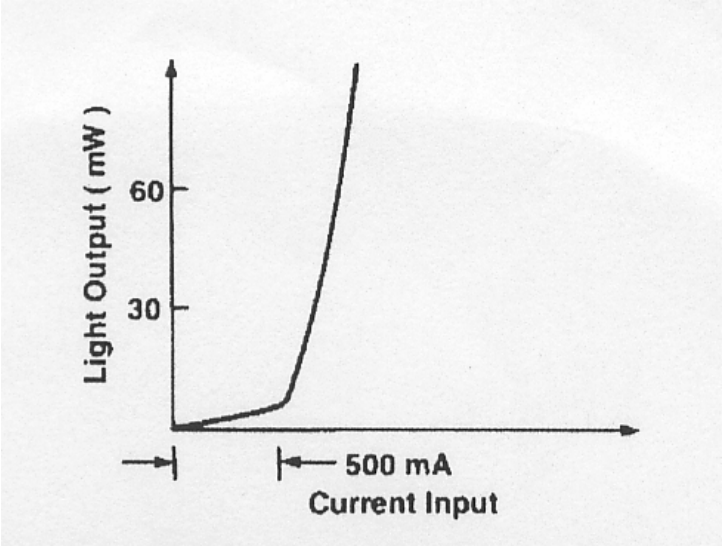

Figure 6 LI Curve of the first reported thin film heterostructure laser [25].

(1:8:500) for 30 minutes. AuGe contacts were patterned in this trench. These two contacts formed two stripes along the surface of the wafer. This stripe pattern was repeated over the surface of the wafer. The laser structure can be seen in Figure 5. Upon completion of the contact metallization and an anneal, the wafer was coated with Apiezon

W black wax and diamond cleaved into 0.55 x 5 mm samples. A sample of this size contained approximately 20 lasers with a 550 μm cavity length. Epitaxial lift-off was performed by immersing the lasers in 10% dilute HF at 0° C for 1 hour and then the

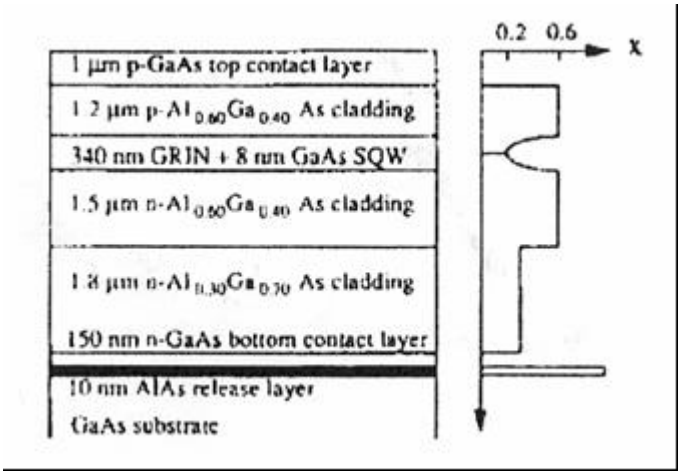

Figure 7 Layer structure of a GRINSCH SQW laser [23].

sample was bonded to a glass or a silicon substrate. The wax allowed these very small, thin samples to be handled. The lasers were then tested using a 1 KHz duty cycle and a 400 ns electrical pulse duration. A typical LI curve can be seen in Figure 6. This performance was similar to the performance of the lasers on wafer and typical of lasers utilizing this design.

While Yablonovitch's lasers were cleaved prior to substrate removal, Pollentier *et al.* demonstrated a fabrication technique where the lasers were cleaved after substrate removal. [23] In this work, graded-index separated-confinement heterostructure GRINSCH) lasers were developed. The structure was grown by metal organic vapor phase epitaxy (MOVPE) and can be seen in Figure 7. Part of the laser processing was completed before the substrate removal step. Laser bars were mesa etched on the wafer

using $H_2SO_4/H_2O_2/H_2O$ (1:8:11). A 50 μm AuZn stripe contact was deposited and patterned. A moat etch was then performed to protect the $Al_{0.60}Ga_{0.40}As$ layers from the subsequent substrate removal etch. The resulting structure was encapsulated in black wax and immersed in $HF:H_2O$ (1:5) solution at 0° C. After the structures were released from the GaAs substrate, an AuGe/Ni ohmic contact was deposited on the released side

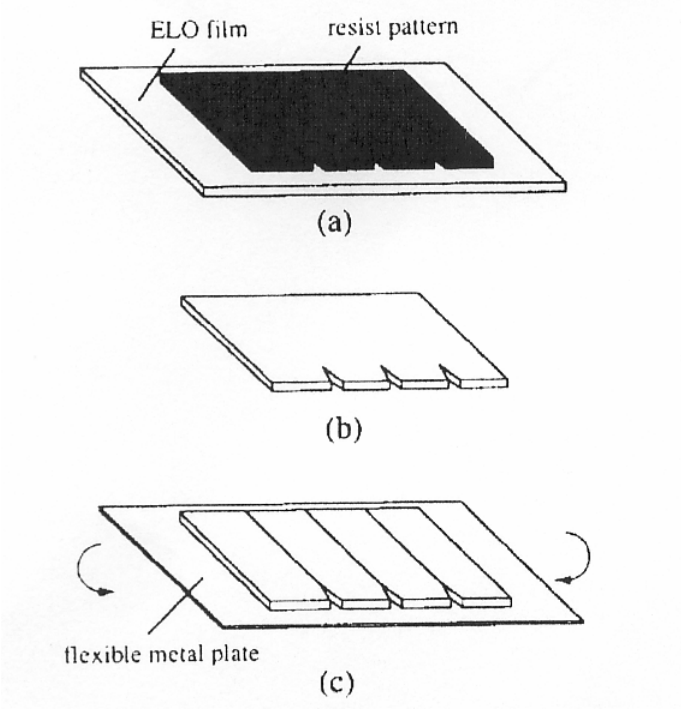

Figure 8 Wedge-induced facet cleaving method. (a) A photoresist pattern is used to mask epitaxial laser film. (b) Wedges are etched out of the epitaxial film and the film is removed from the carrier substrate. (c) The laser film is mounted on a piece of thin flexible metal. The metal is flexed and the material is cleaved into laser bars [23].

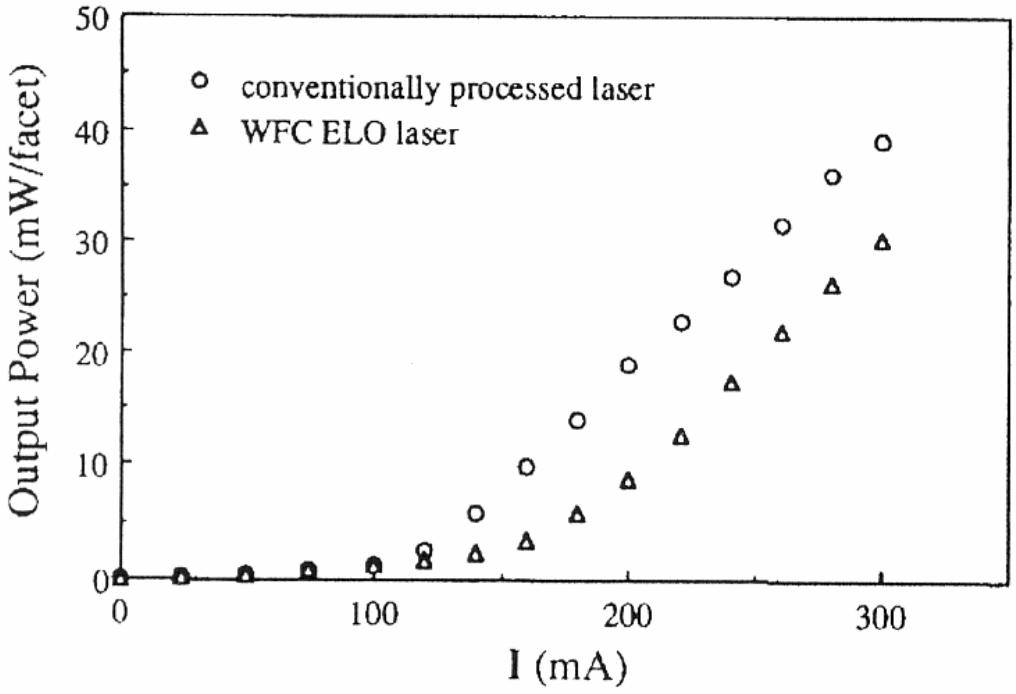

Figure 9 LI curves of a conventional processed GRINSCH SQW laser and a thin-film GRINSCH SQW laser [23].

Of the lasers. The lasers were then prepared for cleaving. Cleaving was achieved through wedge-induced facet cleaving (WFC), the method used to cleave lasers in this work. This technique is based on a wedge-induced microcrack formation technique used in GaAs-on-Si growth. [27] In this process, wedge-shaped notches are introduced into a substrate. As long as the wedges are aligned with the crystal plane of the substrate, the substrate will preferentially cleave at the wedge locations when stressed. Using this method, it is possible to achieve cavity lengths smaller than can be achieved by standard substrate cleaving. This allows for greater flexibility in the laser design in order to minimize the threshold current. The cleaving process is illustrated in Figure 8. The lasers were mounted on a GaAs carrier substrate and the wedges were defined photolithographicly. The wedges were 20 μm deep and 7 μm wide. The wedges were

then etched out using a four-step etch process, using both wet and dry etch steps. Upon completion of the etches, the lasers were removed from the GaAs carrier and mounted on a wax-coated piece of flexible metal. The metal plate was flexed and the lasers were cleaved at the wedge locations. Individual lasers were tested using a 20 kHz duty cycle and a 1 μs pulse duration. The resulting LI curve for a laser with a 250 μm cavity is seen in Figure 9. For comparison, an on-wafer laser of the same cavity length was also shown. The authors believe that the difference in the curves is due to some slight variations between the structures of the two lasers.

A different approach to the thin-film process was presented by Yanagisawa *et. al.*. [26] In this work, a thin-film AlGaAs ridge-waveguide laser diode was fabricated. As in the Pollentier work, the laser was designed as a graded-index separate confinement heterostructure. Unlike that work, though, these lasers were multiple quantum well structures. The laser wafer was metallized with AuGe/Ni/Au ohmic contacts. Three

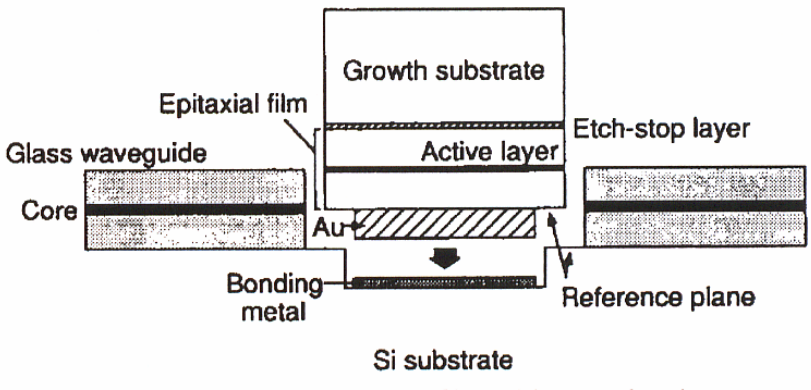

Figure 10 Schematic detailing the integration scheme of a thin-film AlGaAs laser diode with a glass waveguide. [26]

microns of gold was then plated on these contact metals. The laser wafer was then cleaved into individual devices with a 300 μm cavity length. A 1 μm thick bonding metal pad of AuSn was deposited on a Si substrate and the laser was bonded to this pad.

After bonding, the substrate of the laser was removed by etching it away using H_2O_2/NH_4OH (30:1) to an AlAs etch-stop layer. The AlAs layer was then removed with 10% dilute HF. After substrate removal, standard laser processing techniques were performed to form a ridge-waveguide laser. For this work, the laser was embedded with a glass waveguide and can be seen schematically in Figure 10. The threshold current of this laser was 63 mA and the LI curve can be seen in Figure 11.

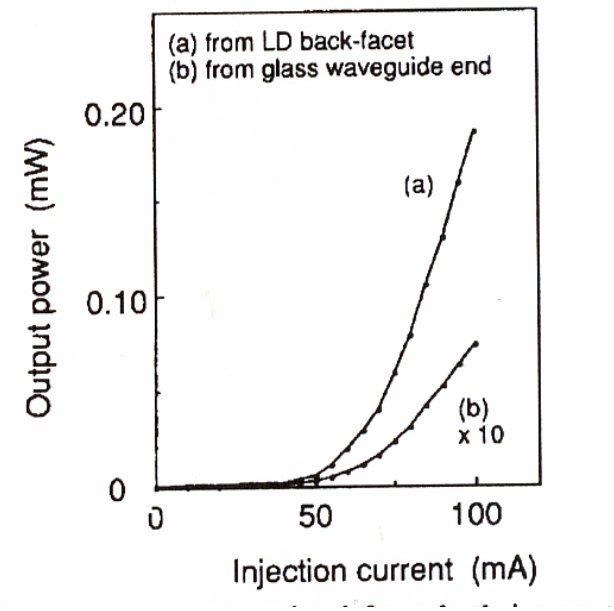

Figure 11 LI curves of a thin-film AlGaAs laser. (a) Power output from a laser facet. (b) Power. [26]

A related thin-film process used in laser fabrication involves the bonding of the epitaxial laser growth to a host substrate different from the growth substrate. By bonding the epitaxial layers to a host substrate such as silicon, the handling issues revolving around the thin epitaxial layer are solved and standard processing techniques can be used to fabricate the lasers once they have been transferred to a host substrate. Shieh *et al.* fabricated an InGaAsP ridge-waveguide laser using this method. [24] The laser structure can be seen in Figure 12. In this process, a metallic solder layer consisting of

Ti/Au/Sn/Au/Sn/Au (50/200/200/200/200/200 nm) was deposited on the laser substrate and the host silicon wafer. The laser wafer was aligned with the Si wafer and the two

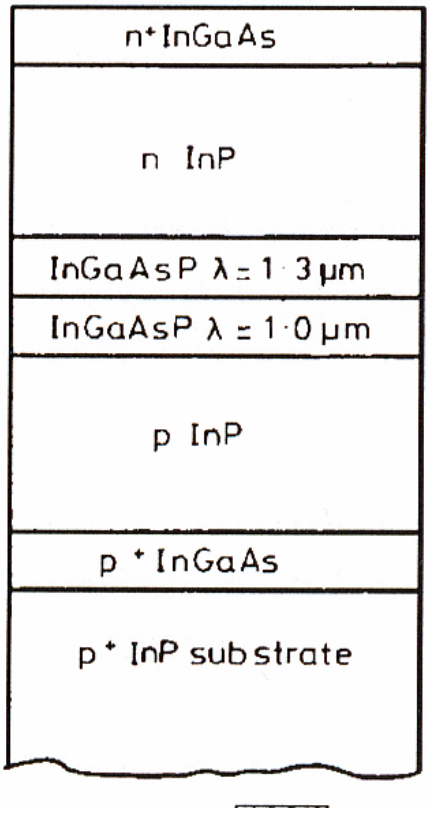

Figure 12 Structure of an InGaAsP laser growth. [24]

wafers were held together for 20 minutes at 420° C to completely bond the two wafers together. After the bonding, the InP substrate was removed by immersing the structure in HCl. Upon substrate removal, ridge-waveguide lasers were fabricated using traditional techniques. The wafer was thinned to a thickness of 125 μm and was cleaved into individual devices with a 300 μm cavity length. Lasers were tested with a 1 KHz duty cycle and a 650 ns pulse duration. The lasers operated with a 24 mA threshold current and the resulting LI curve can be seen in Figure 13. This Figure also shows the output of a laser grafted on a GaAs host substrate. This laser had a 28 mA threshold current. Similarly, Fan *et. al.* demonstrated a GaAs/InGaAs ridge-waveguide laser bonded to Si.

[22] The laser was a GRINSCH single quantum well structure. Traditional fabrication techniques were used to develop ridge-waveguide lasers on the surface of the laser wafer. The wafer was encapsulated in black wax and the entire wafer was immersed in diluted 10% HF to etch an AlAs sacrificial layer. The epitaxial layers were released from the GaAs substrate. The Si host substrate was metallized with Pd/Ge/Pd (1000Å/1300Å/250Å). The Si wafer was then lapped down to a thickness of 100 μm and a 5000Å thick layer of aluminum was deposited on the backside. The laser epitaxial layers were bonded to the Si wafer by Van der Waals bonding. The bonded structure was then heated to 400°C to anneal the contacts. The grafted structure was then cleaved into lasers with an 800 μm cavity length. The LI for these lasers can be seen in Figure 14. These lasers had a 16.3 mA threshold current and a 0.4 W/A slope efficiency. An on-wafer laser is presented for comparison with the epitaxially lifted-off laser. The lift-off techniques demonstrated in this paper are used to fabricate the thin-film devices presented in this work.

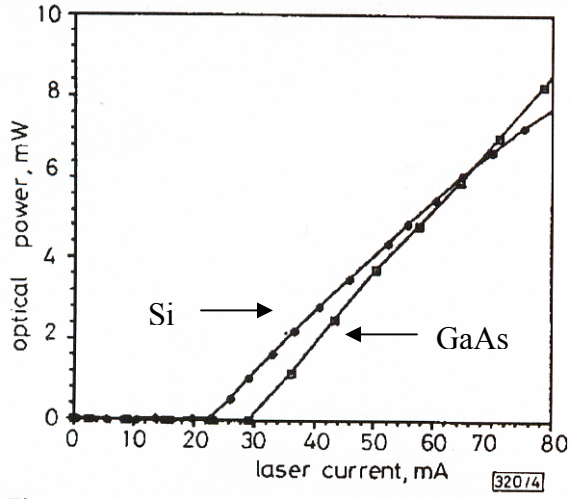

Figure 13 LI curves of thin-film InGaAsP lasers grafted to GaAs and Si. The silicon grafted laser has a threshold current of 24 mA, while the GaAs grafted laser has a threshold of 28 mA. [24]

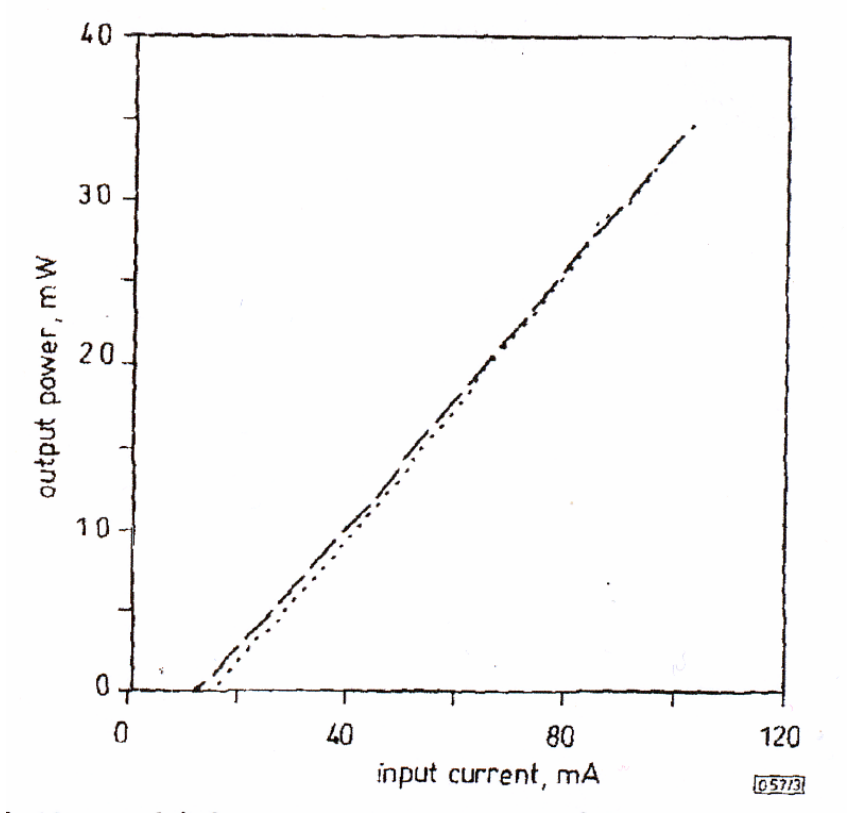

Figure 14 LI curve for a GaAs/InGaAs laser grafted to a silicon wafer. The dashed line is an on-wafer laser of the same material. The dotted line is the laser on silicon. [22]

2.2 Optically Embedded Interferometric Sensor Component Technology

2.2.1 Optical Waveguide Theory

The theory of optical waveguides has been reported in many different sources. [28-31] This section will give a brief overview of some of the important aspects concerning optical waveguides. This section will examine an optical ray model which can be used to understand how light propagates in a waveguide.

A quantitative relationship has been put forth that explains the propagation of light in a waveguide [32]. In this analysis, only the TE polarization is taken into account. TE polarization is dominant in unstrained MQW lasers, the optical sources used in this research. By considering the step index waveguide parameters n_f (film index), n_c (cover

film index), n_s substrate index, and W (waveguide film thickness) with regard to dispersion in the waveguide, a model can be constructed. First, a zigzag ray model for reflection between two waveguide boundaries must be considered when describing the pulse path in the waveguide. Dispersion is bounded by the transverse resonance condition that says that the sum of all phase shifts perpendicular to the direction of propagation in the waveguide must be a multiple of 2π for one zigzag period in the waveguide. The implication of this rule is that the total phase shift of the wave must be an integer multiple of 2π. One transverse passage through the waveguide results in a phase shift of $kn_fW\cos\theta$, where $k = 2\pi/\lambda$. A full period consists of two transverse passages. Phase shifts of $-2\theta_c$ and $-2\theta_s$ occur due to the total internal reflection (TIR) at the cover and substrate boundaries. The phase shift could then be defined as shown below:

$$\left(2kn_fW\cos\theta\right) - 2\theta_c - 2\theta_s = m(2\pi) \qquad [13]$$

$$\theta_c = \tan^{-1}\left[\frac{\left(n_f^2\sin^2\theta - n_c^2\right)^{1/2}}{n_f\cos\theta}\right] \qquad [14]$$

$$\theta_s = \tan^{-1}\left[\frac{\left(n_f^2\sin^2\theta - n_s^2\right)^{1/2}}{n_f\cos\theta}\right] \qquad [15]$$

Since the total phase change must be a multiple of 2π, only distinct, discrete angles will satisfy Equation 13. These allowed angles make up the set of guided modes which are supported by the waveguide.

The angle of incidence, θ, is an important factor in meeting the conditions for total internal reflection. A simple waveguide interface can be seen in Figure 15. Light incident on the interface can either be refracted or it can be reflected. At every interface,

there exists a minimum angle at which all light is reflected and total internal reflection occurs. In order to achieve TIR, the incidence angle must exceed this minimum value, θ_c, known as the critical angle. The critical angle is given by the following equation

$$\sin\theta_c = \frac{n_2}{n_1} \qquad [16]$$

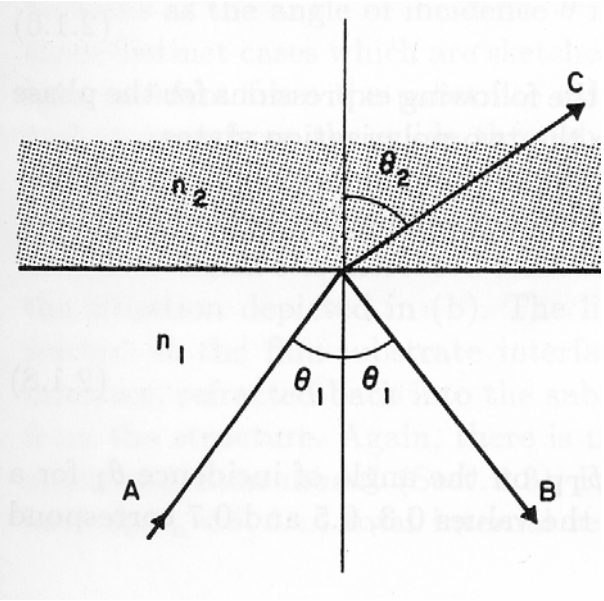

Figure 15 Simple waveguide interface.

Figure 16 illustrates three different situations that can occur depending on the value of the incidence angle. In scenario a, the incidence angle is less than the critical angle at the waveguide, cover layer interface. There is partial reflection and partial refraction of the incident light. The refracted light escapes from the waveguide and is called a radiation mode. In scenario b, the incident angle exceeds the critical angle at the waveguide and cover layer interface, but is less than the critical angle at the waveguide-substrate interface. In this situation, again the light is partially reflected and partially refracted. The light that escapes into the substrate is known as a substrate mode. In scenario c, the incidence angle is greater than the critical angles at the cover-waveguide

interface and at the substrate –waveguide interface. In this situation, all of the light is reflected at the boundaries and total internal reflection occurs.

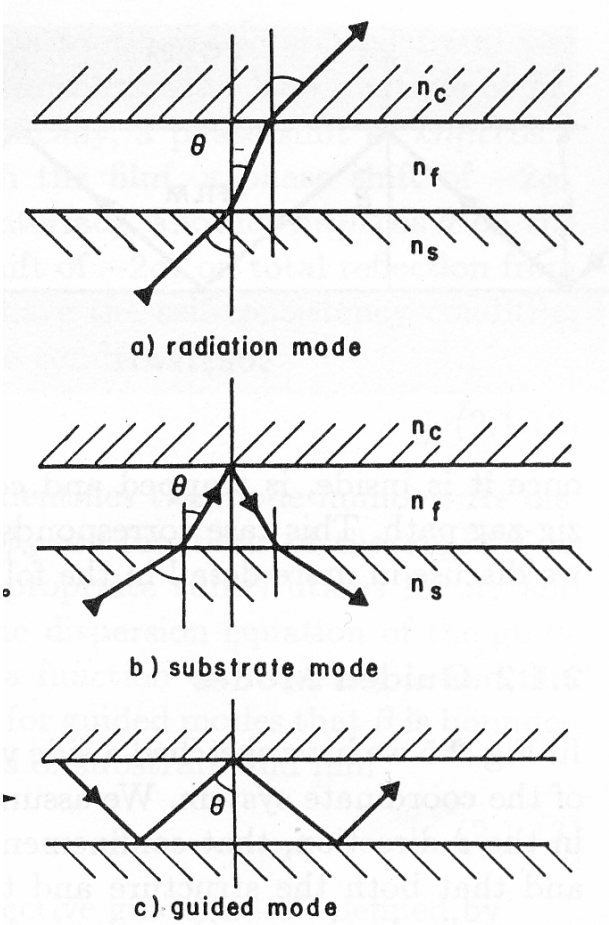

Figure 16 Examples of various radiation modes in a waveguide. (a) Radiation mode. (b) Substrate mode. (c) Guided mode.

2.2.2 Waveguides Integrated on CMOS

The growing feasibility of optical interconnects has generated a great deal of interest in optical components on Si CMOS. To maintain the growth rate dictated by Moore's law, circuit designs must become smaller and more tightly confined. At these scales, problems such as cross-talk, skew, power requirements, and dissipation become dominant. [33] Optical links offer high packing density, low power dissipation, wide

bandwidth, and low latency. [34, 35] The greatest challenge to this endeavor is developing a structure that is compatible with the CMOS circuits. [36, 37] Any component integrated onto a CMOS circuit must have no process step that will damage the circuit. To this end, two distinct methods have been developed. The first method involves monolithically integrating passives during the CMOS process itself. This approach has the advantage of being extremely compatible since the fabrication can be done during the CMOS fabrication. Unfortunately, the optical components must be constructed out of materials available in standard CMOS processing. This limits the choices available during design and the achievable performance of the optical links. Alternatively, it is also possible to integrate waveguides following the CMOS process. This technique enables optimization of all materials and high performance due to the individual optimization of the system components. Unfortunately, it also requires post-processing of the CMOS circuits and has to be designed carefully to be compatible with the circuit technology.

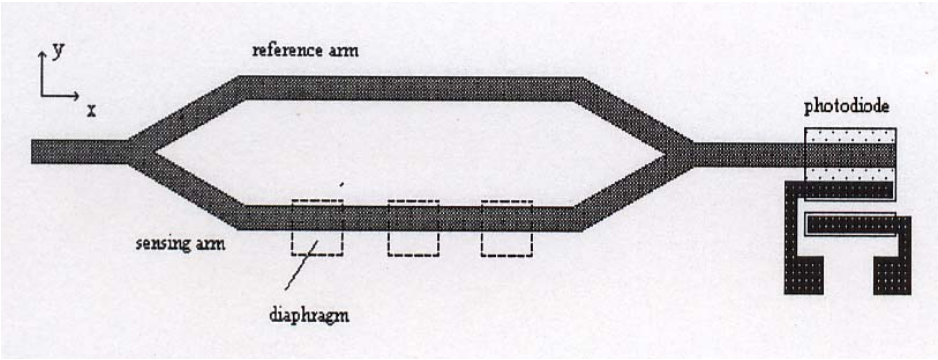

Figure 17 Schematic drawing of an interferometric pressure sensor. [38]

CMOS ready waveguide structures constructed with "CMOS process compatible" materials have been demonstrated by a large number of research groups. Several of those results will be reviewed here. An opto-mechanical pressure sensor base on a Mach-

Zehnder interferometer (MZI) has been demonstrated. [38] The sensor consists of a two channel MZI. One channel was treated as a reference arm, while the other channel was integrated with three diaphragms. Deflections in the diaphragms caused changes in the propagation constants in that channel of the interferometer. These changes were detected at the end of the interferometer using a photodiode. Pressure readings can be made from these outputs. A schematic drawing can be seen in Figure 17. Several different waveguide material systems were examined for this work. Silicon nitride, silicon carbide and silicon oxynitride (SiON) were used to construct waveguide. Each material is readily available during the CMOS process. Depending on the needs of the desired sensor (operating wavelength, flexibility, fabrication restraints), each material system was suitable for some version of the sensor.

Another demonstration of this monolithic integration scheme was reported by Hilleringmann *et al.* [39] This work examines suitable technologies for a monolithic design of optical interconnects on silicon and discusses design considerations that must be made for the most reliable system. The authors considered Si_3N_4, phosphosilicate glass (PSG), and SiON as viable waveguide core layers. Silicon oxynitride was selected as the most suitable core because its index of refraction may be adjusted by changing the gas mixture during its deposition. Several integration arrangements, seen in Figure 18, were examined to determine the best coupling scheme between the waveguides and the detectors. Scenario (c), using turning mirrors to couple light into the detector, was chosen as the best option. This scenario was better suited than the others because of the high coupling efficiency demonstrated by the arrangement, the CMOS compatible process used to fabricate the required structures, and the mirrors easily reproducibility

and fabrication using standard dry etching techniques. To verify these conclusions, the authors integrated a SiON waveguide on a silicon substrate with a photodetector and a transimpedence amplifier. The waveguide had a measured 0.5 dB/cm propagation loss. The efficiency of the coupling between the waveguide and the detector was shown to be strongly coupled to the mirror etch depth. The further the mirror extended into the guiding region, the larger the amount of light coupled into the detector. As long as the system was fabricated modularly, there was no recorded degradation in the CMOS component performance. When then the entire system was fabricated at the same time, there was significant variation in CMOS performance. Further studies would be necessary to make the process fully monolithic.

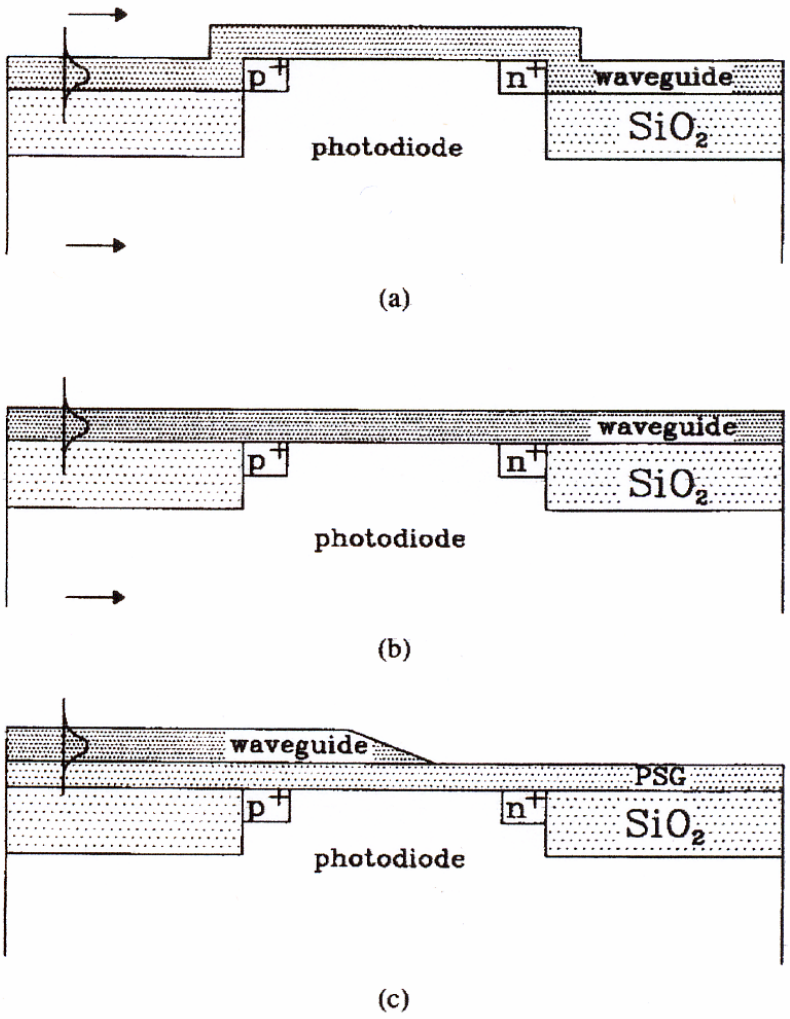

Figure 18 Three coupling schemes for waveguides integrated monolithically on Si CMOS. (a) Butt coupling. (b) Evanescent coupling. (c) Coupling using mirrors. [39]

Post-processing CMOS circuits to integrate optical links has also been studied. Most efforts in this area are focused on the integration of polymer waveguides on CMOS circuitry. [40, 41] One of the early reported CMOS circuits integrated with waveguides was fabricated by the Integrated Optoelectronics Group at Georgia Tech. Polymer waveguides consisting of a benzocyclobutene (BCB) cladding/planarization layer and a polyetherimide (ULTEM) core were integrated on Si CMOS photodetector arrays. Planarization of the BCB was improved through multiple spin coatings and repeated

etches in an inductively coupled plasma etcher. Two different CMOS circuits were integrated. One circuit consisted of Si detector arrays of various sizes, while the other circuit consisted of Si detectors connected to sigma-delta analog to digital converters (ADCs). These two circuits were test circuits for the integrated sensor implementation. The sigma-delta circuit is shown in Figure 19, integrated with polymer waveguides. Light from a HeNe laser was propagated through the waveguides integrated on both circuits. The results from these tests can be seen in Figure 20 and Figure 21. The detector current at various optical outputs launched into the detector array circuit can be seen in Figure 20. [41] The dark current of the detector array is also included for reference. The output generated by the sigma-delta circuit is shown in Figure 21. [41] The output of the sigma delta ADCs is a discrete multi-bit value which corresponds to the analog photocurrent generated by the embedded detectors. The circuits showed an increase in the mean of the bit stream samples with increasing power, which was the expected result.

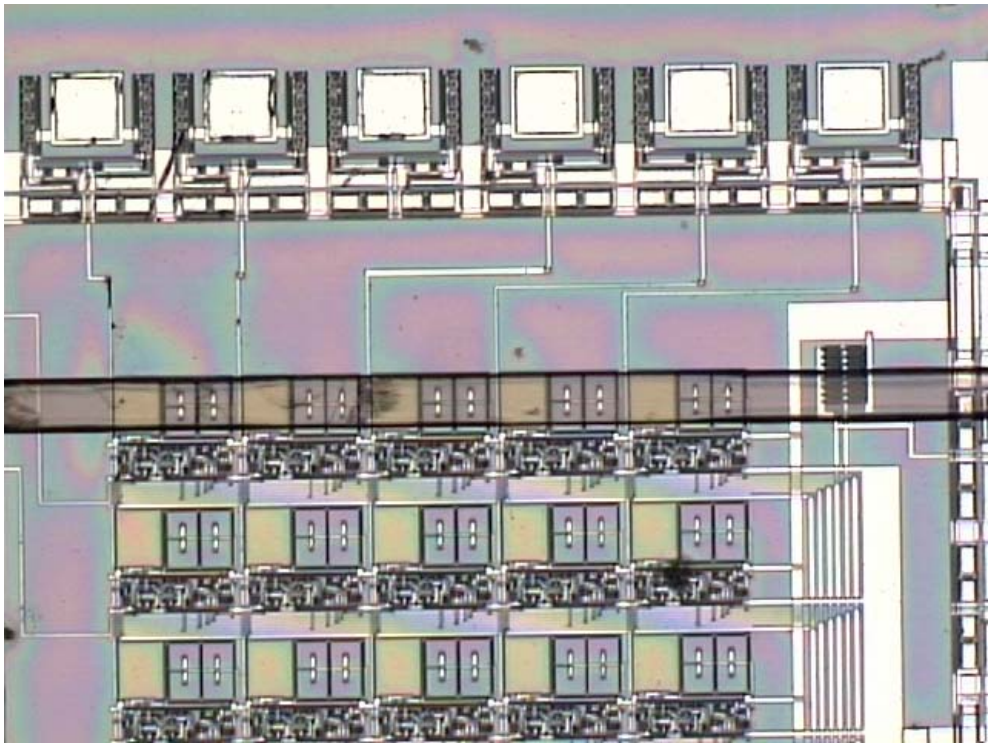

Figure 19 Sigma-delta ADC circuit integrated with a BCB\ULTEM channel waveguide.

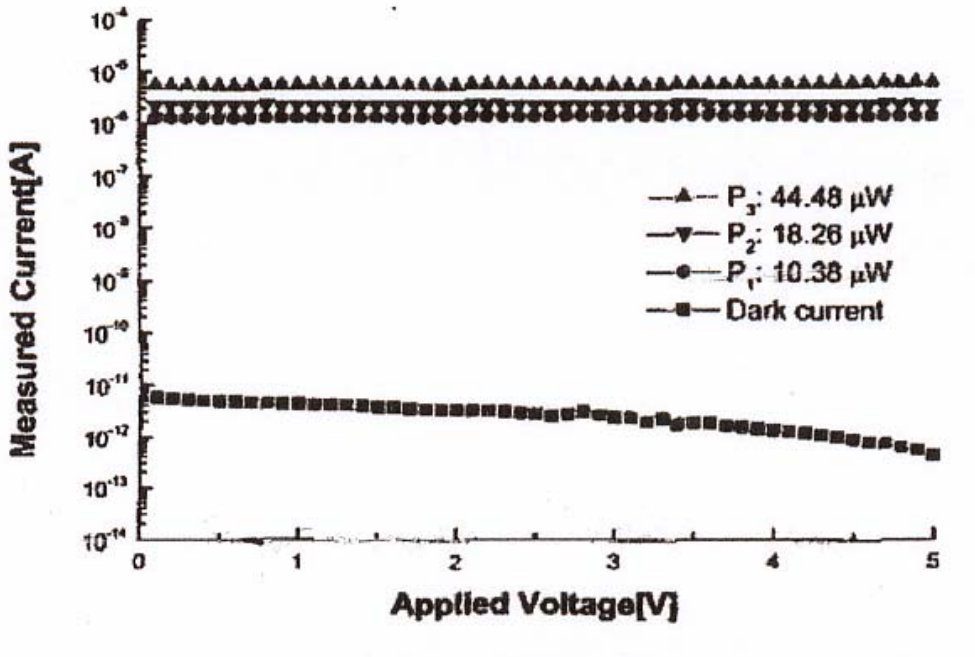

Figure 20 Measured photocurrent from the detector array circuit at various optical input powers. A HeNe laser was used. [41]

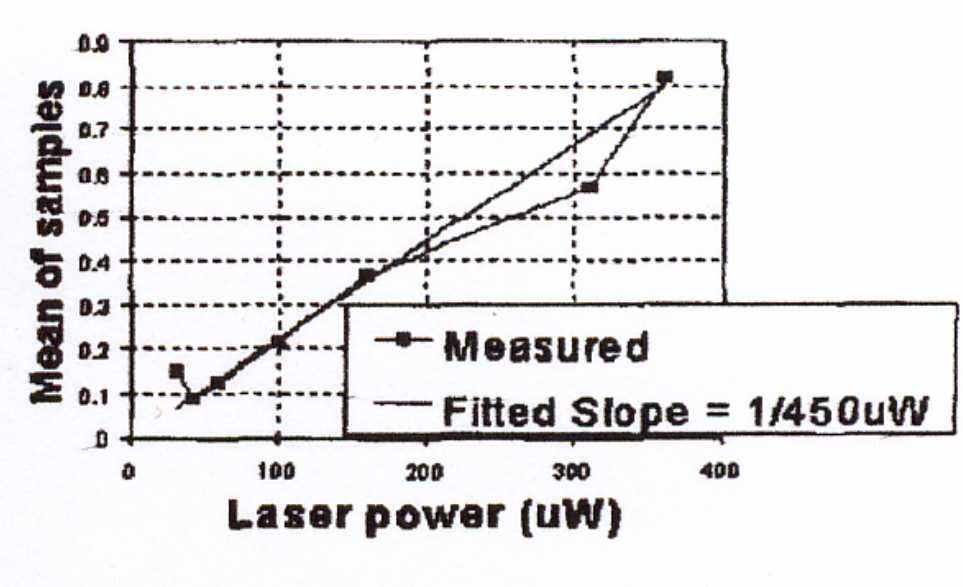

Figure 21 Plot of the output of the sigma-delta ADC circuit. [41]

2.2.3 Embedded optics in waveguides

The growing interest in optical interconnects has created a need to understand the relationship between waveguides and active devices integrated with or embedded within the waveguides. The selection of the optical emitter type will dictate the required optics for coupling into the waveguide. Edge emitting devices such as edge emitting lasers do not require turning elements as they can launch light directly into a waveguide. Coupling is achieved through butt coupling, free space coupling, or embedding the device directly in the waveguide. Implementations using sources such as vertical cavity surface-emitting lasers (VCSELs) require the addition of a beam-turning element, such as a turning mirror, to couple light into the waveguide. [40, 42, 43] For embedded sources, it is also necessary to consider the fact that physically placing a device into a waveguide will affect the physical characteristics of the device. The reflectivity of the mirrors can be affected by the embedding process, and the index of refraction difference between the waveguide material and air must also be considered. Surface-emitting sources have been

the popular choice for integrated emitters because of their low power consumption, high-speed operation, and small beam divergence. [43, 44] Recent efforts have begun to examine the feasibility of integrating edge emitting sources. [45-49]

Integrated detector research generally has concentrated on the coupling efficiency between the detector and the waveguide. For most optical links, the power budget for the system is small and the efficiency of the coupling between the waveguide and the detector can be the deciding factor between a successful link and a failure. The primary mode of coupling employed in most links is evanescent coupling. Ease of fabrication makes this method the most popular choice, but it suffers from one major shortcoming. A long coupling length is required because of the low coupling efficiency vertically between the detector and the waveguide. [50] This long coupling length requires larger detectors, which becomes restrictive in high-speed applications because of an increase in detector capacitance with increasing detector size. This fact has led to an increasing use of MSM photodetectors since they have a smaller capacitance than standard PiN detectors of the same size. [51] Work has also been done to investigate the use direct coupling in optical links. [52-55] Efforts have also been made to increase the coupling efficiency by using turning optics and butt coupling into the detector. These changes enable the use of more standard detector technology by reducing the detector size requirements. Increased efficiency also reduces the necessary power budget for the link.

Several research groups have reported VCSELs embedded in waveguides for use in optical links. [42-44] Mederer *et al.* have reported an optical link capable of speed of 3 Gb using an integrated VCSEL in polycarbonate polymer waveguides. [44] An 850 nm VCSEL was used as the optical source. The active diameter of the VCSEL was 8 μm. It

had a threshold current of 0.8 mA and a maximum output power of 8.2 mW at 12 mA. Two different waveguide structures were used in the experiment. One waveguide was a standard channel waveguide, while waveguides with a trapezoidal cross-section were also used. The different cross sections were used to examine the impact of waveguide shape on the experiment. The maximum loss of the polymer waveguides was measured as 1.7 and 0.5 dB/cm, respectively, for the two waveguides tested. Free space optics were used to launch the VCSEL output into the waveguide. A BER of 10^{-11} was achieved for a 3 GB/s PRBS NRZ signal with a 2^{31}-1 word length.

Several groups have reported varying schemes for fabricating optical links using embedded photodetectors. [42, 45, 52-54] One such scheme has been reported by Liu *et al.*. [35] They reported GaAs MSM photodetectors integrated with polymer waveguides. Coupling was achieved through the use of 45° total internal reflection (TIR) micromirror couplers. The polymer waveguides were fabricated from polyimide spin-coated onto the MSMs. This material was chosen for its high optical transparency, high thermal stability, and ease of fabrication. The polyimide used was photosensitive so the waveguides could be formed using standard photolithographic techniques. The waveguides fabricated were 50 μm in width and approximately 12-13 μm in height. Two different varieties of the polyimide were used as a core and cladding layer and they had indexes of refraction of 1.56 and 1.54 at 850 nm. These indexes could be slightly tailored through variations in the process conditions. The fabricated channel waveguides had a loss of 0.21 dB/cm at 850 nm and 0.58 dB/cm at 632.8 nm. The TIR micromirrors were formed by placing the waveguides in an RIE at a 45° angle. An Al mask was used to protect the rest of the waveguides and the mirrors were etched out over the MSM locations. Figure 22 shows

the waveguide channels with etched TIR micromirrors. After polishing the endface of the channel waveguides, a single mode fiber was used to butt couple light into the waveguides. The generated photocurrent was monitored and the system was determined to have a 3 dB bandwidth at 2.648 GHz.

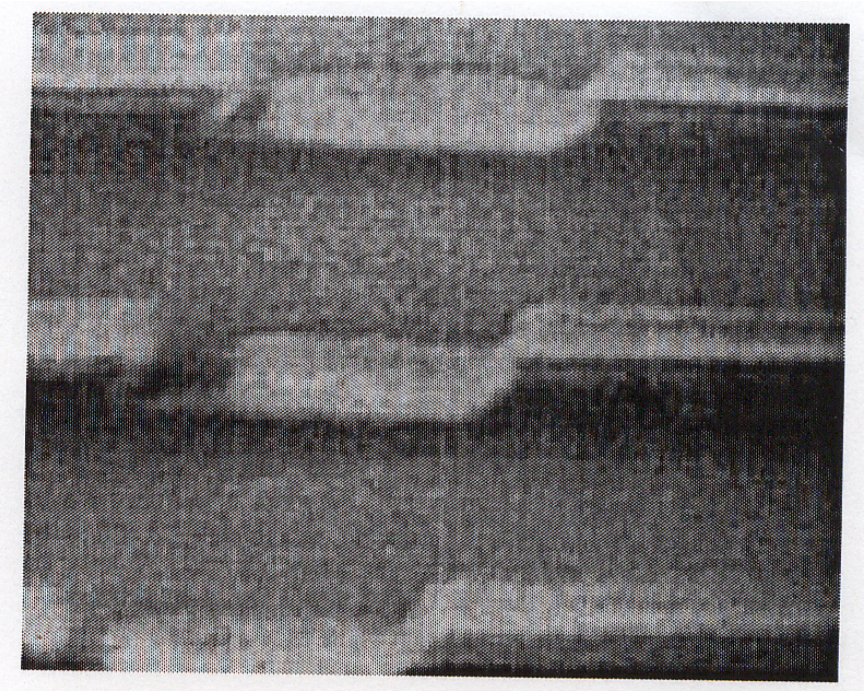

Figure 22 SEM microphotograph of a polymer channel waveguide array with embedded 45° TIR micromirror couplers. [35]

2.3 Summary and Discussion

This chapter reviewed the relevant technology needed in order to complete the work detailed in this dissertation. The first section of this chapter investigated semiconductor lasers. In particular, gain-guided lasers were presented. Following a brief discussion of basic semiconductor laser operation, the gain mechanism and the threshold conditions of gain-guided lasers were investigated. A review of thin-film lasers was then presented. Several authors have demonstrated the feasibility of this technology in the optoelectronics field.

The second section of this chapter dealt with the waveguide technology necessary for the work presented in this dissertation. First, a review basic waveguide theory was presented. The next two subsections reviewed relevant research to this work. A review of waveguides used in conjunction with CMOS circuitry was presented. Following this, a subsection reviewing integrated and embedded active photonic devices in waveguides was included. Included in these results were reports of both detectors and lasers embedded in waveguides in order to created an integrated optical system.

Chapter 3

Biological\Chemical Sensor Background

3.1 Interferometric Sensors

Interferometric structures used as chemical and/or biological sensors have been researched by several different groups. [56-61] Interferometers are used to interfere two or more light sources. When source interfere with each other, the maximum intensity of the resultant light may exceed the sum of the intensities of the light sources or be less than the sum of the intensities of the light sources. When the resultant intensity is greater than the sum of the intensities, it is known as constructive interference. When the resultant intensity is less than the sum of intensities, it is known as destructive interference. For interference to occur between the light sources, three conditions have to be met. [31] The light sources have to have the same polarization. The light sources have to oscillate at the same frequency. There must also exist a constant phase relationship between the light sources. At any point along the interference region, the phase difference between the light sources must remain constant. Light sources meeting these conditions are known as coherent light sources. Optical sensors of this nature offer several benefits over similar electrical sensors. Optical sensors offer higher sensitivity than electrical sensors. [59] They are also immune to electromagnetic interference. The passive nature of these sensors also makes them desirable when dealing with explosive or combustible materials. [59]

A popular interferometer is the Mach-Zehnder interferometer (MZI). The MZI is an amplitude splitting interferometer. A single light source is split by a beam splitter into

two or more beams. The sum of the light intensities out of the beam splitter will equal the light intensity of the original light source. The light beams continue along their path or arm until they are recombined and collected. Since the paths the light travels are independent of each other, variation in one path will create a phase difference between the beams of light. Since this phase difference is directly related to the variations in the paths, it has the potential to be used in various sensor systems.

An interferometric sensor operates by detecting changes in the index of refraction in one arm or path of the interferometric sensor. The index of refraction change is induced by a sensing layer which interacts with the light in the sensing arm causing a phase change in the light. The index of refraction change is directly related to the phase change between the arms, so monitoring the phase change is an important aspect of the sensor operation. In its simplest implementation, there are two arms in the interferometric sensor. One arm is the sensing arm and the other arm is the reference arm. The arms of the sensor should be generally identical. In a balanced implantation, a sensing layer is applied to both arms of the interferometer. This is done to isolate the actual phase change in the sensing arm. Since both arms experience the sense layer, any phase change between the two arms is due to changes in the sensing layer such as index of refraction. In this arrangement, it simple to extract out the sensor information, the index of refraction, as any change detected is directly attributable to changes in the sensing layer. The only difference between the two arms is that a silicon dioxide cladding layer is applied to the reference arm to isolate it from the environment. This arrangement can be seen in Figure 23. In an unbalanced system, the two arms do not experience identical paths. This can be seen in Figure 24. In this implementation, there is

a phase difference between the two arms that is not due to an index change in the sensing layer. The sensing arm is impacted by the sensing layer in Figure 24, but the reference arm is not due to the silicon dioxide cladding. In this arrangement care must be taken to account for the phase difference between the two arms due to this unbalanced structure. Prior to sensor operations, the sensor must be calibrated so the phase change caused by this design can be subtracted out of the final signal in order to isolate the phase change due to the index change in the sensing layer. The unbalanced approach involves more data processing than the unbalanced approach, but both are still valid techniques.

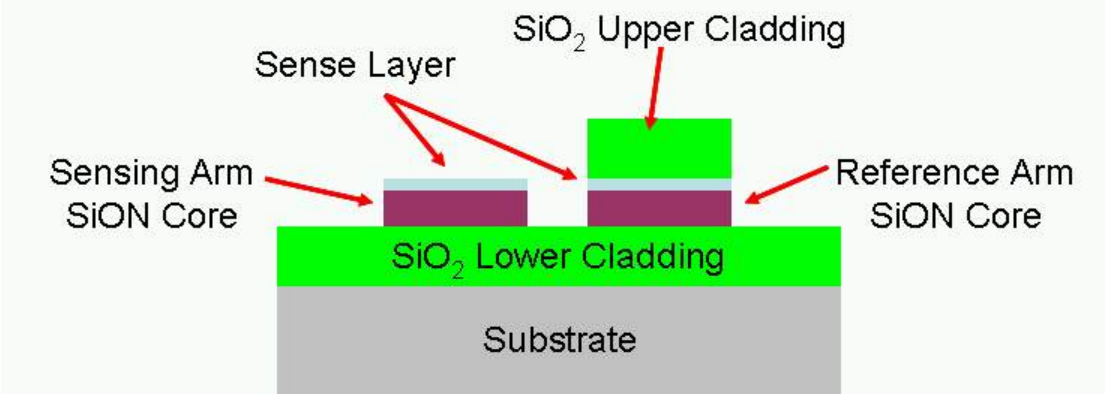

Figure 23 Cross-section of balanced interferometric sensor.

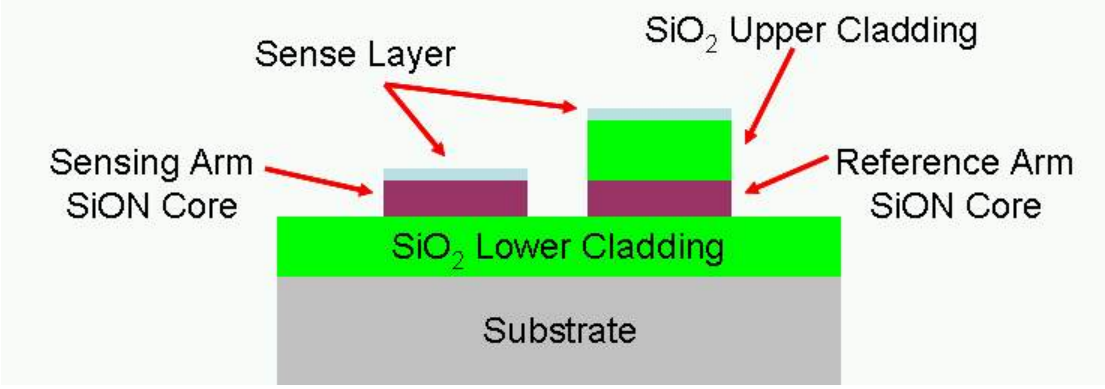

Figure 24 Cross-section of an unbalanced interferometric sensor.

The chemically selective film used to coat the sensing region is key to this detection. Optical signals transmitted down the waveguide have an evanescent field that penetrates the region above the waveguide, the chemically selective region. This effect is illustrated in Figure 25 [62]. The extension of this field into the sensing region allows the optical pulse to be sensitive to any change in the refractive index of the chemically selective film. Changes in the index of refraction (n) in this film alter the phase of the propagating wave. Antibody/antigen reactions, chemical reactions, or polymeric swelling, depending on the material used for the film, can change the index of the film. These reactions would occur when the agent that the sensor is designed to detect comes into contact with the chemically active region. These phase changes can be detected by interfering the phase-shifted pulse in the sensing arm with the unperturbed pulse in the reference arm.

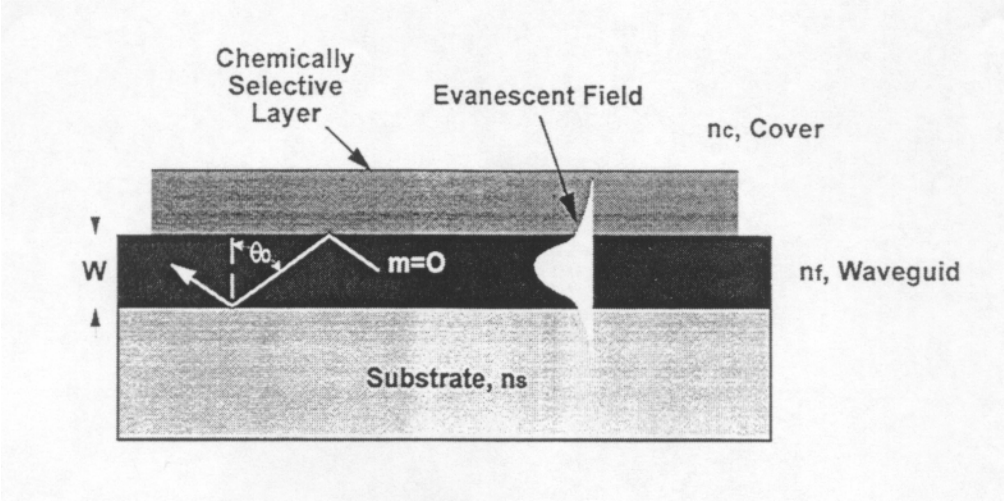

Figure 25 Cross-sectional view of light propagating down the sensing arm of an interferometric sensor. [62]

Using Equations 13-15 and 17, it is possible to calculate the phase shift of the sensor. I_1 and I_2 are the intensities of the light in the two arms, while I is the intensity of

the interferometer output. Using those three values which can be experimentally calculated, the phase shift, δ, can be calculated from Equation 17. [31] This value can be substitute into Equation 13 as $\delta = kn_f W\cos\theta$. Substituting Equations 14 and 15 into Equation 13, n_c, the cover index or the sensing layer index, can be calculated. If the index of refraction of the sensing layer is known before the test is done, it is possible to calculate the change in refractive index of the sensing layer, N_{eff}. This change in refractive index can also be seen in the equation governing the interferometer output represented in Equation 18 [32]

$$I = I_1 + I_2 + 2\sqrt{I_1 I_2}\cos(\delta) \qquad [17]$$

$$I = \frac{I_o}{2}\left[1 + \cos\left[\frac{\pi}{2} + \frac{2\pi}{\lambda}L(\Delta N_{eff})\right]\right] \qquad [18]$$

The change in refractive index can then be used to sense and identify contaminants in the environment. For this research, sensor development was based on the work done by Nile Hartman. A detailed discussion of the Hartman sensor is given in the next section.

3.2 Hartman Sensor

The design of the Hartman biosensor can be seen in Figure 26 [62]. The key components in this design include an IO interferometer chip, a diode laser, and a photodiode detector. Another important component that is excluded from this figure is the signal processing electronics that would be needed to process the biosensor's collected data. The grating couplers are used to couple the diode laser output into the waveguide and out of the waveguide into the photodiode. The gratings also serve the purpose of easing alignment. Using gratings, little alignment is actually needed. As long as the gratings are in the light path, they will turn the beam into the waveguide or into the detector. Traditional

coupling methods such as butt coupling and prism coupling are highly sensitive to XYZ alignment. The gratings are relatively insensitive to XYZ positioning and only require a rough angular alignment. [62] This feature lowers packaging cost and makes it easier to replace these chips in the field.

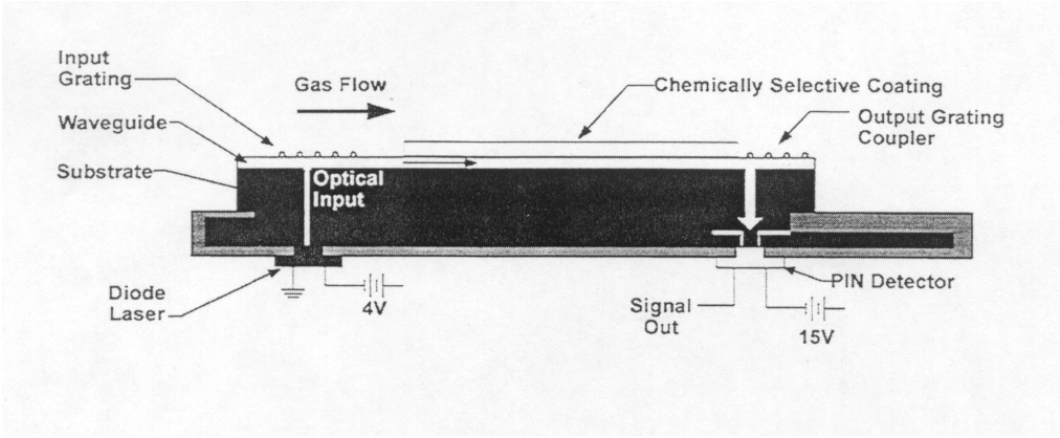

Figure 26 Cross-sectional view of the Hartman biosensor package. [62]

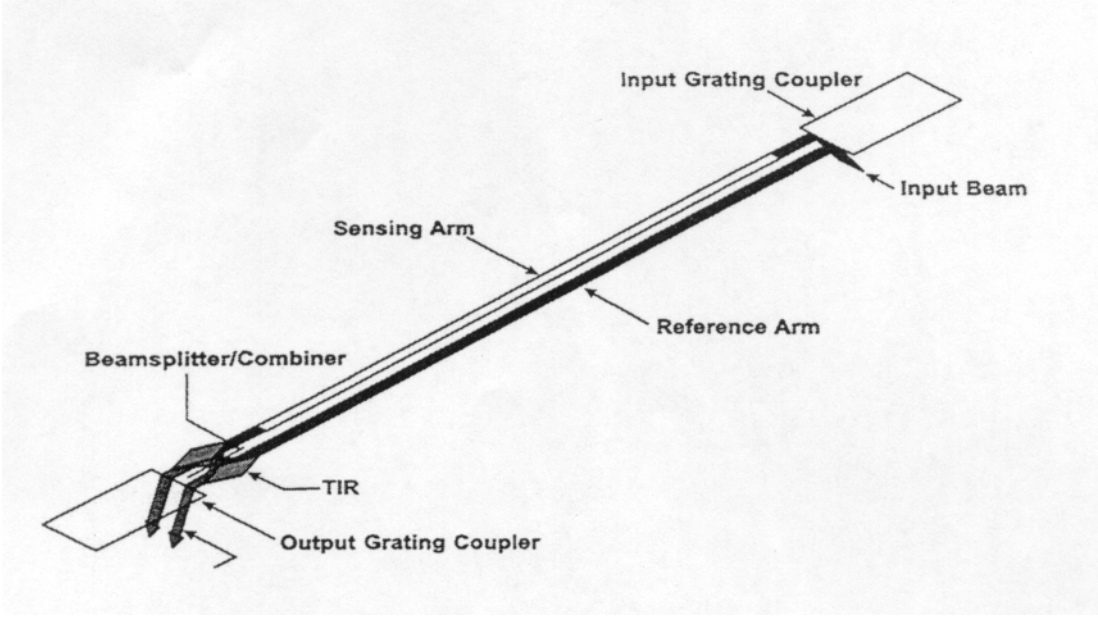

Figure 27 Single-channel IO interferometer configuration.[62]

A single interferometer channel is seen in Figure 27 [62]. The main parts of this design include the grating couplers, the waveguide film, and the beam combining/splitting elements. An optical signal is coupled into the structure using the grating couplers. The optical signal travels down the sensing and reference arms that are defined on the waveguide surface. Interference is generated at the beam combining/splitting elements by dividing and mixing the signal in the two arms. This interference is used to calculate the change in the refractive index in the waveguide.

The biosensor is fabricated using simple processing techniques. The grating couplers are first produced by etching a 0.7 μm period grating into an optically transparent substrate surface. The gratings are patterned using precision lithography methods such as holography or e-beam lithography. Once patterned, the gratings can be etched in a dry etching tool such as a RIE or an ICP, depending on the substrate material. The waveguiding film, such as Si_3N_4, is then deposited using plasma-enhanced chemical vapor deposition (PECVD). This film typically measures 0.14 μm in thickness. [62] The beam splitter/combiners are constructed from total internal reflecting (TIR) mirrors and a beam splitter. The TIR mirrors are fabricated by dry etching a 40 μm trough completely through the waveguiding layer. The beam splitter is formed by etching a 0.05 μm trough into the waveguiding layer. The entire surface, excluding the sensing region, is then coated with silicon dioxide (SiO_2). This layer isolates the fabricated components from the environment to provide operational isolation. The chemical sensing layer is then bound covalently or electrostatically to the sensing region. A laser diode and photodiode are wire bonded into the system and aligned with the input and output grating couplers. The entire system is then packaged with the signal processing electronics. An example of

this packaging is found in Figure 28. The entire package measures 2.5 x 3.0 x 6.5 inches [32, 62-64].

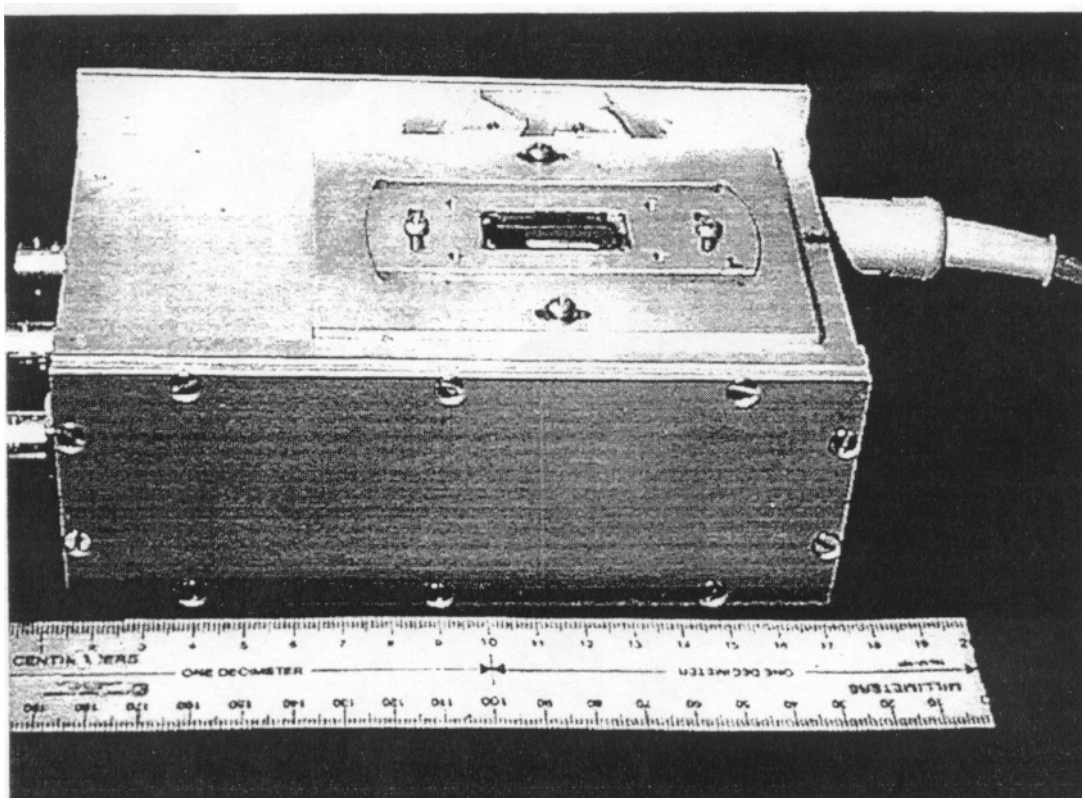

Figure 28 Example of a packaged biosensor. [62]

3.3 Summary and Conclusion

This chapter reviewed the relevant biological/chemical sensor technology used in this dissertation. The first section detailed the general operating principles of interferometric sensors. A basic framework for sensor operation was presented. A very specific sensor was used for the basis of the research presented in this dissertation. This implementation is known as the Hartman sensor. The Hartman sensor design is

presented. A discussion of the fabrication methodology and the packaging of the completed sensor unit is also detailed.

Chapter 4

Integrated Sensor Circuit Fabrication and Results

A modular approach has been taken toward the work in this thesis. The project has been broken down into four areas. The first component involves the development of the interferometric sensor. The second component deals with the integration of the optical components with the Si CMOS circuitry. The third area involves the development of the laser. The final component of the work involves the theoretical modeling of the optical performance of the system.

4.1 Interferometric Sensor Development

The first decision that had to be made regarding the interferometer development dealt with the material system that would be used to fabricate the structures. Any material used would have to be low loss at the operating wavelength (850 nm), resistant to any chemical it would be exposed to, and compatible with standard silicon CMOS circuitry. Silicon oxynitride and silicon dioxide both meet these requirements, while also being inexpensive and easy to fabricate using a PECVD. Theses two materials were selected as the material system to be used for all interferometers in this research. Silicon oxynitride was used as the core material of the interferometers and silicon dioxide was used as the cladding layers. These types of single-mode sensors interferometric sensors have been widely reported in the literature. [65-68]

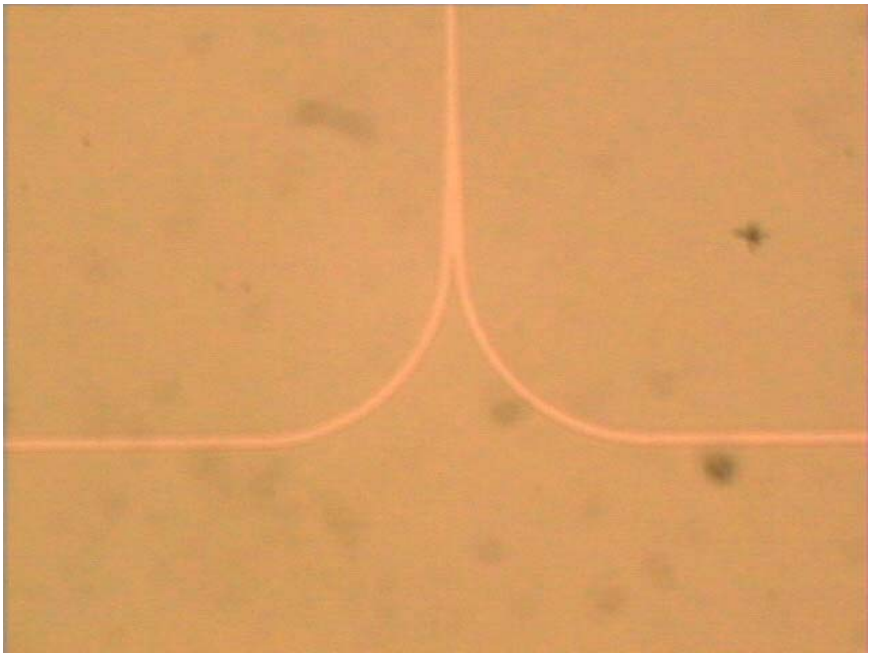

Figure 29 Photomicrograph of the waveguide used to determine the waveguide loss using the scanning fiber method.

The waveguide materials were then characterized using the optical fiber scanning method. In this method an optical beam at 850 nm is endface coupled into the end of a SiO_xN_y/SiO2 waveguide. The waveguide fabricated for these tests can be seen in Figure 29. These waveguide structures consisted of a silicon dioxide (n = 1.465) cladding layer varying in thickness from 1-3 μm and a silicon oxynitride (n = 1.922) core layer 1 μm in thickness. The waveguide was fabricated on a silicon substrate. Coupling alignment was facilitated by the use of an infrared camera. Once the fiber was coupled to the waveguide, the top surface of the waveguide was scanned at different points along the waveguide in order to determine the loss associated with the waveguide materials. A large core optical fiber was used to perform the surface scan. The large core fiber was used in order to ensure all the light radiating out of the top of the waveguide was collected. This multimode fiber had a core diameter of 600 μm and a numerical aperture

of 0.37. This fiber was used to collect the scattered light from the surface of the waveguide and this light was measured using a calibrated indium gallium arsenide photodetector connected to a Newport 1835 optical power meter. The separation between the waveguide and the fiber was optimized to maximize the light collected by the fiber. While maintaining a uniform separation between the scanning fiber and the waveguide surface (+/- 1 mm), 300 scanning points were measured perpendicular to the waveguide at intervals of 10 μm. This data set constituted one scan line during the test. Three hundred total scan lines were performed on the waveguide, at increments of 10 μm along the direction of the waveguide. Precise movements of the fiber were achieved using a Coherent motorized micro-positioner. In order to compensate for losses due to the horizontal alignment during the scan, the measured optical power was averaged using the multiple scan lines. This averaged data was then used to calculate the propagation loss of the waveguide by calculating the slope of the linear least square regression of the averaged collected optical power from the waveguide before the detector. Two of the plots generated for this thesis can be seen in Figure 30. From these figures, it was calculated that the SiO_xN_y/SiO2 waveguide had a loss of 0.76 dB/cm when the oxide cladding layer was 1 μm thick and 0.4 db/cm when the oxide cladding layer was 2.0 μm thick. The difference between these two values can be attributed to the underlying silicon substrate and its absorption at 850 nm. These values are comparable to reported propagation loss measurements found in the literature. [69, 70]

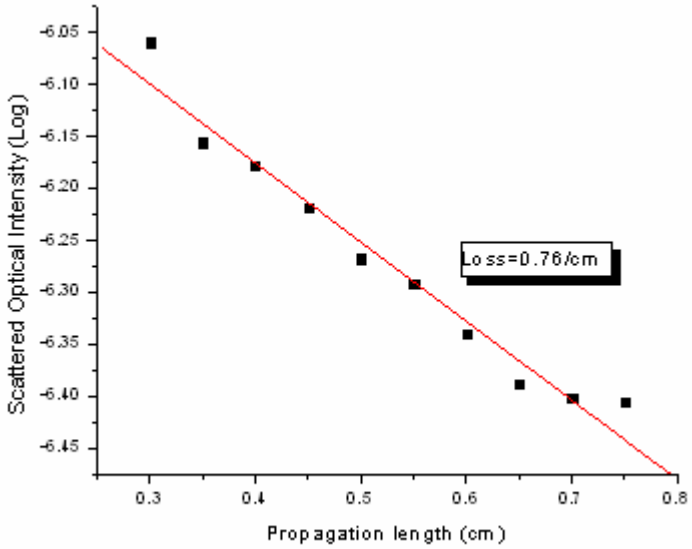

(a)

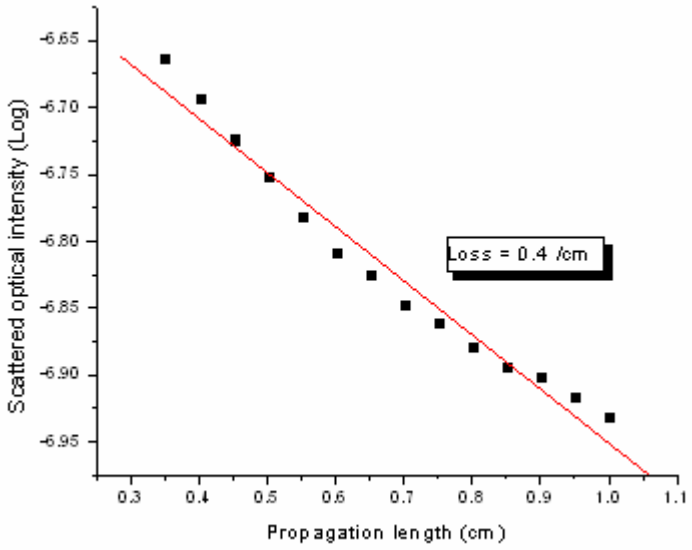

(b)

Figure 30 Plot of waveguide loss for two different waveguides. (a) Waveguide with a 1 µm bottom cladding. (b) Waveguide with a 2 µm bottom cladding

Channel waveguides were fabricated prior to interferometer fabrication. The fabrication process began with the deposition of the waveguiding layers on silicon

substrates. Plasma-enhanced chemical vapor deposition was used to first deposit a 1 μm layer of SiO_2. This cladding layer was followed by a layer of SiO_xN_y. The thickness of the nitride was varied from 0.2 – 1.0 μm. A final 1 μm thick layer of SiO_2 was deposited as an upper cladding layer. This final cladding layer also served as an isolation layer for the sensing arm on the interferometers. Following the material deposition, standard photolithography techniques were used to pattern a thick photoresist mask defining the multimode channel waveguides on the silicon substrate. Channel widths used were 50, 100 and 250 microns. A PlasmaTherm ICP etcher was used to define the waveguide structures. The etch gas used in this step was 30 standard cubic centimeter (sccm) CF_4, which is a common gas used to etch silicon dioxide and silicon oxynitride. The fabrication of the channel waveguides was completed upon the removal of the photoresist mask using acetone. Photoresist stripper was sometimes also used if the photoresist became hardened by the plasma etching process.

Two wavelengths of light were used to test the interferometers. The ends of the channels were cleaved to provide a clean endface for coupling. Light was coupled into the waveguides using a λ=632 nm semiconductor laser or a λ=840 nm semiconductor laser. Both of these lasers were fiber coupled into a single mode fiber (core = 5.5 μm, numerical aperture = 0.12) tapered at its output. A tapered fiber was used to improve the coupling between the fiber and the interferometers. The tapered output was coupled into the waveguide. The resulting modal pattern out of the interferometer end facet was imaged using a CCD camera and can be seen in Figure 31. The modal pattern observed was single mode in the vertical direction and multimode in the horizontal direction. This arrangement was selected specifically for this application. The multimode nature of the

waveguide facilitates coupling between the laser and the waveguide and increases the sensing area of the sensor. [71] The downside of the multimode waveguide was that the data analysis of the complex modal structure was challenging and required increasing processing power for increasing modal complexity. By designing the waveguide to be single mode in the vertical and multimode in the horizontal, it was possible to optimize the waveguide sensor for sensor area and coupling efficiency, without the need for a tremendous amount of data processing circuitry. After successful fabrication and coupling in channel waveguides, interferometer fabrication began.

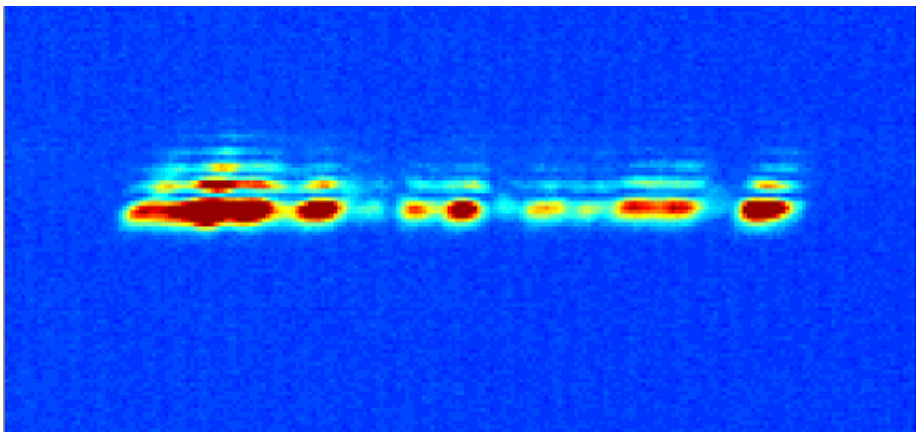

Figure 31 Modal pattern capture from the endface of a 50 µm wide, 1.1 µm thick channel waveguide. The guide was illuminated with an 840 nm fiber-coupled

The fabrication of the interferometer was similar to that of the channel waveguides. A PECVD was used to deposit $SiO_2/Si_3N_4/SiO_2$ waveguiding layers on a bare silicon substrate. The same thicknesses used in the channel waveguides were used in the interferometer structure. Standard photolithography was used to define a photoresist mask of the interferometers. The interferometers were defined by etching in

an ICP etcher using CF_4 plasma. Residual photoresist from the mask was removed using acetone or photoresist stripper. At this point in the fabrication it was necessary to define the sense arm on the interferometer. A thick photoresist mask was patterned over the interferometers. The mask opened a window over one arm of each interferometer. The silicon dioxide cladding over that arm was etched using the CF_4 recipe in the ICP etcher. The etch rate of silicon dioxide in the ICP was well known, so the proper etch depth was achieved through precise timing. The photoresist was removed again by using acetone or photoresist stripper. The final Mach-Zehnder interferometer structures were 4500µm long and have 100µm wide waveguides. The interferometer arms were 2000 µm in length. Approximately 300 modes were supported in the horizontal direction in the waveguide with this configuration. [71] The interferometer was then ready for application of a sense agent or testing.

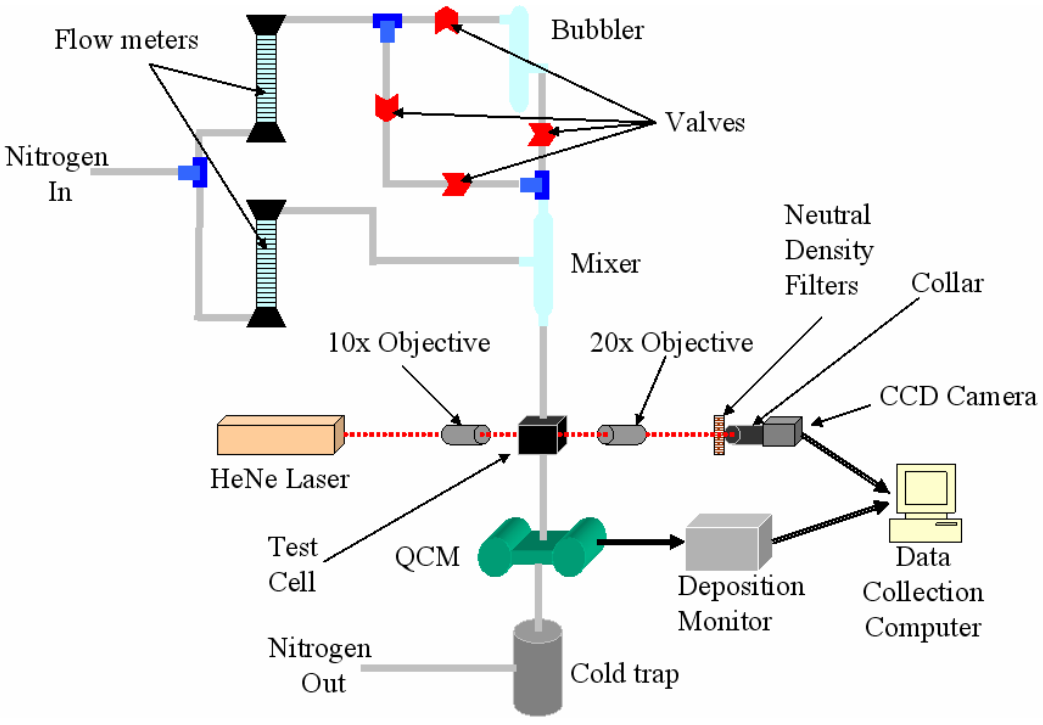

Figure 32 Test setup for interferometric sensors.

Two approaches were taken when applying the sense agent. The agent was either spin coated over the entire substrate or a photodefinable polymer was used. In the case of the photodefinable polymer, the agent was patterned and only left on the sense arm. Ideally, the sense agent should be under the upper cladding layer to balance the sense arm more closely with the reference arm of the interferometer. For the preliminary test, this balancing was sacrificed for the fabrication simplicity of applying the sense layer last. Once any and all sense layers were applied to the interferometer, the structures were ready for testing.

Two different sense agents were used during the work in this thesis. Those two materials were Teflon AF and bis-trifluoromethyl carbinol-substituted polynorbornene (HFAPNB). Teflon AF proved difficult to work with as nothing would adhere to the cured film. This caused patterning to be impossible and a suitable method was not found for dispensing the polymer in one location. HFAPNB was the polymer primarily used in this work. It was a photosensitive polymer that could be applied and patterned using basic photolithography techniques. Three different types of materials were detected during this research. They included water, benzene, and alcohol. HFAPNB absorbed all of these materials. The absorption of these materials caused an index change to occur within the film. The index change was then used to determine the concentration of the material being detected.

A diagram of the test setup for all tests on the interferometers can be seen in Figure 32. The laser source used for these experiments was a Spectra Physics Stabilite Model 120s HeNe laser. The output of this laser was 15 mW. This laser output was free-space coupled into the interferometric sensors using a Mitutoyo M Plan Apo 10x

objective lens. The output modal pattern of the sensor was imaged on a Hitachi CCD camera using a Mitutoyo M Plan Apo 20x objective lens. Neutral density filters were used to control the intensity level of the light incident on the camera. An anodized aluminum collar was also mounted on the camera to reduce its field of view in order to improve the camera's sensitivity to changes within the modal pattern. This was achieved by limiting the external stimulus to the camera, ensuring that any change at a pixel is due to a change in the signal. The camera had a frame rate of 10 frames per second and 768 x 494 effective pixels. The pixel pitch was 8.4 x 9.8 μm. The output of the camera was monitored using a LabView program on a computer in the lab. The data it collected was processed by assigning a numeric value to each pixel as a function of intensity and displayed in order to enable real-time monitoring.

The interferometers were mounted in a hermetic test cell designed for these experiments. The cell was constructed of anodized aluminum. Quartz windows were mounted on opposite sides of the cell for coupling into and out of the test cell. Two ports were also designed into the test cell to allow for input and output of a gas stream.

A gas delivery and monitoring system was also included with the optical components of the setup. The carrier gas of the system was nitrogen. Nitrogen gas flow was controlled by two flow meters. The two gas streams output by the flow meters were mixed and then delivered to the test cell. One of the streams feeding into the mixer could be diverted from its path to a line containing a bubbler. The bubbler line could then be used when a chemical was needed to be delivered to the test cell for detection by flowing the nitrogen gas through the analyte. Once a gas was delivered to the test cell, it exited the cell out of the output port. This exiting stream was fed into a quartz crystal

microbalance (QCM). In a QCM, the frequency of a quartz crystal is monitored. Any change to the surface of the crystal is reflected in a change in the frequency of the crystal. For each test, a crystal was coated with the sensing layer that was being evaluated. As the sensing layer absorbed the chemical being detected, a change in the frequency of the crystal was detected. This data could then be used to determine the amount of the chemical that reacts with the sensing layer in the experiments. An Inficon deposition monitor was used to monitor the QCM frequency data and it was then collected by a computer in the lab. Gas exiting the QCM was passed to a cold trap, where the chemical was removed from the nitrogen stream. The cleaned nitrogen stream was then vented into the building exhaust.

Figure 33 shows two modal patterns collected over time of an interferometer coated with HFAPNB as the sense agent. The changes in modal patterns track associated changes in the sensing layer on the sensing arm of the interferometer. The changes are due to changing humidity in the test cell. The change in humidity was caused by

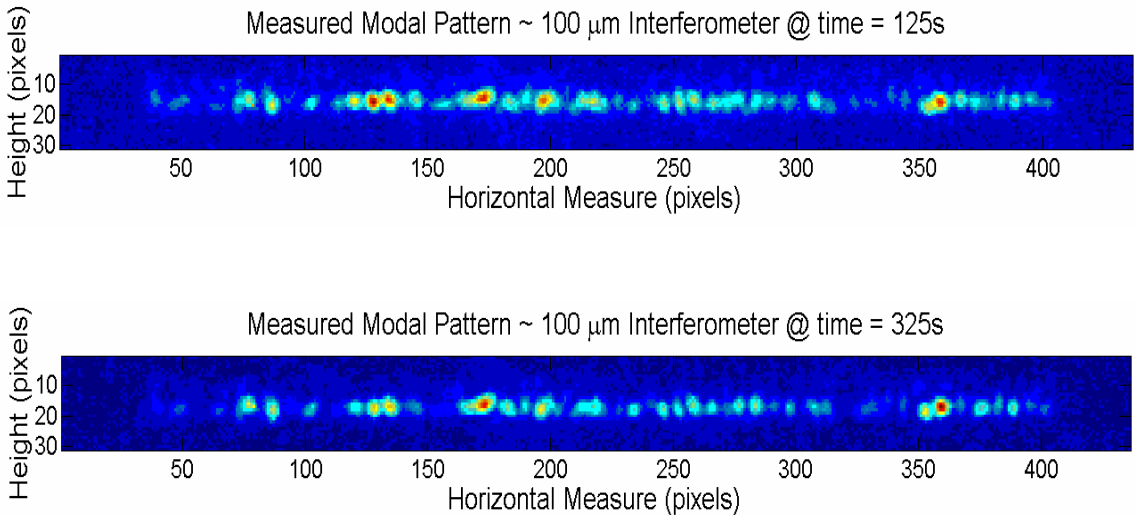

Figure 33 Interferometric sensor modal patterns.

introducing water vapor to the test cell using the bubbler. The modal pattern at 125s represents the interferometric output of the sensor with no water vapor present. The modal pattern at 325s shows the output after water vapor was introduced to the cell. A clear change in the modal pattern was seen in these two images.

There are several sources of noise in the patterns. Noise in the system came primarily from source fluctuations, shot noise, read noise, and dark current noise. [71] The source noise is a result of instabilities in the laser that cause drift. This noise can be corrected by using a feedback stabilized laser. Photogenerated electrons are collected in a capacitive structure called a well in CMOS detectors. Shot noise variance is directly related to the random arrival time of photon and scale directly with the mean number of photoelectrons in the well. Shot noise variance is much larger under high intensity due to the fact that the number of photogenerated electrons is proportional to the optical power. Shot noise becomes the dominant noise source under high intensities for the system. Read noise, also called the noise floor, is the fundamental noise of the electrical components in the system. It can be reduced by introducing a larger well in the CMOS detector. Dark current is the fundamental noise floor from the detector itself. As stated before, under sufficiently high intensities, shot noise dominate the noise figure. Under lower intensities, dark current and read noise play a much more important part.

The index sensitivity of the interferometric sensor was also determined. [71] This was accomplished by tracking the aggregated normalized power of the pixels as there was an index change in the sensing layer. The index of refraction was measured using a high speed, spectroscopic ellipsometer. Four agents where characterized in this way: methanol, water, benzene, and isopropanol. The smallest change that could be made,

resulting in a measurable index change was ~450 parts per billion vapor (ppbv) for methanol, 15 ppbv for isopropanol, 30 ppbv for benzene, and 150 ppbv for water. [71] These sensitivities were ultimately limited by the coupling fluctuations in the external coupling of the source laser. The proposed integrated sensor solution would improve on these sensitivities.

An optimized integrated sensor system would allow for improved index sensitivity. First the estimated noise in the system was lowered in the fully integrated system versus the system that was used to make the previously reported measurements. This can be seen in Figure 34. [71] The measured sensor data was limited by noise generated by source fluctuations. The fully integrated sensor would be limited by shot noise, read noise, and dark current noise. The estimated sensor showed a 4 to 6 times reduction in noise. The pixel size of the integrated sensor would also reduce the index sensitivity. A reasonable CMOS pixel pitch was 2.8 μm. Compared to the CCD camera array, this pixel size reduced the index sensitivity by a factor of two. Also, optimizing the waveguide core thickness improved the index sensitivity. The majority of tested interferometric sensors had a core thickness of 0.2 μm. The optimal core thickness was determined to be 0.13 μm. At this thickness, the evanescent field in the sensing layer was maximized. By changing the core thickness, the index sensitivity was improved by 20%. [71] Taking these factors into account, the index sensitivity of the fully integrated sensor was estimated to be 170, 6, 12, 57 ppbv for methanol, isopropanol, benzene, and water, respectively. [71] A significant improvement over the measured system data was shown.

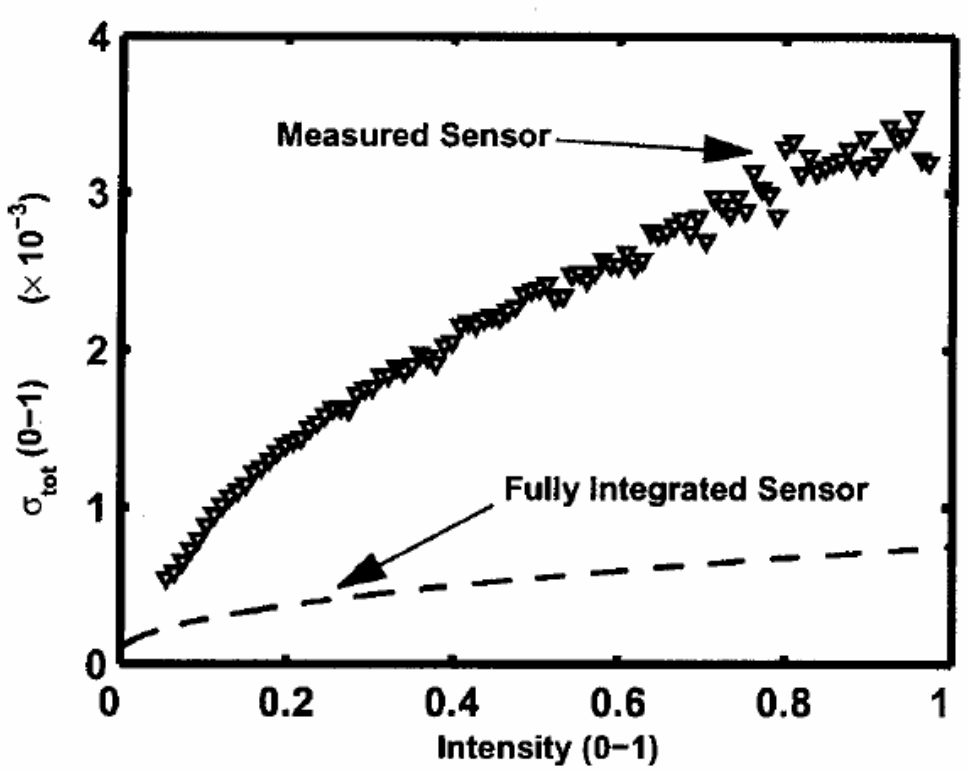

Figure 34 Plot of the standard deviation versus intensity of the actual measured sensor system and the estimated fully integrated sensor. [71]

Further test were performed in order to demonstrate sensor operation on-wafer. [71] Figure 35 shows pixel data captured from the interferometric sensor using the CCD camera setup described earlier. A representative multimode pattern and its corresponding one-dimensional intensity profile are presented in Figure 35a and 35b, respectively. Figure 35c shows the difference between intensity patterns for 0 ppbv and 37 ppbv. Figure 35d shows the intensity change seen over time for a CCD pixel with no concentration change, which represents the noise of the system. The noise of the system compared to the signal generated by the system differed by several orders of magnitude. The large difference achieved with only a 37 ppmv change in concentration indicated that a highly sensitive sensor system was possible. In order to quantify these results into a

useful metric, a figure of merit was chosen which would collect the pixel data into a reliable measurement of agent concentration. The figure of merit used in this work was the root-mean-square signal-to-noise ratio for all of the pixels of the CCD array. The root-mean-square SNR is given by [71]

$$S(t) = \left[\sum_{j=1}^{N} \frac{(\Delta P)^2 (t, j)}{\sigma_j^2} \right]^{1/2} \qquad [19]$$

where $(\Delta P)^2(t,j)$ is the square of the pixel power change, t is the time, j is the pixel number, and σ_j^2 is the variance of the jth pixel. Figure 36 illustrated the calibrated of the response of the interferometric sensor using this figure of merit. The values listed at each plateau represent the agent concentration level in ppbv. Chemical vapor concentrations from 8 ppmv to 149 ppmv were used in this test. Examining the data, it is noted that the sensor response is fairly inearly for values less than 80 ppmv. The response of the 15 ppmv plateau was approximately half of the 30 ppmv plateau. Above 800 ppmv, the sensor appeared to have a slightly nonlinear response which was due to the cyclic response of the multimode pattern. [71] The noise in the system was attributed to the MFCs used in the system. From this plot, it is seen that a quantifiable concentration measure using interferometric sensors was developed.

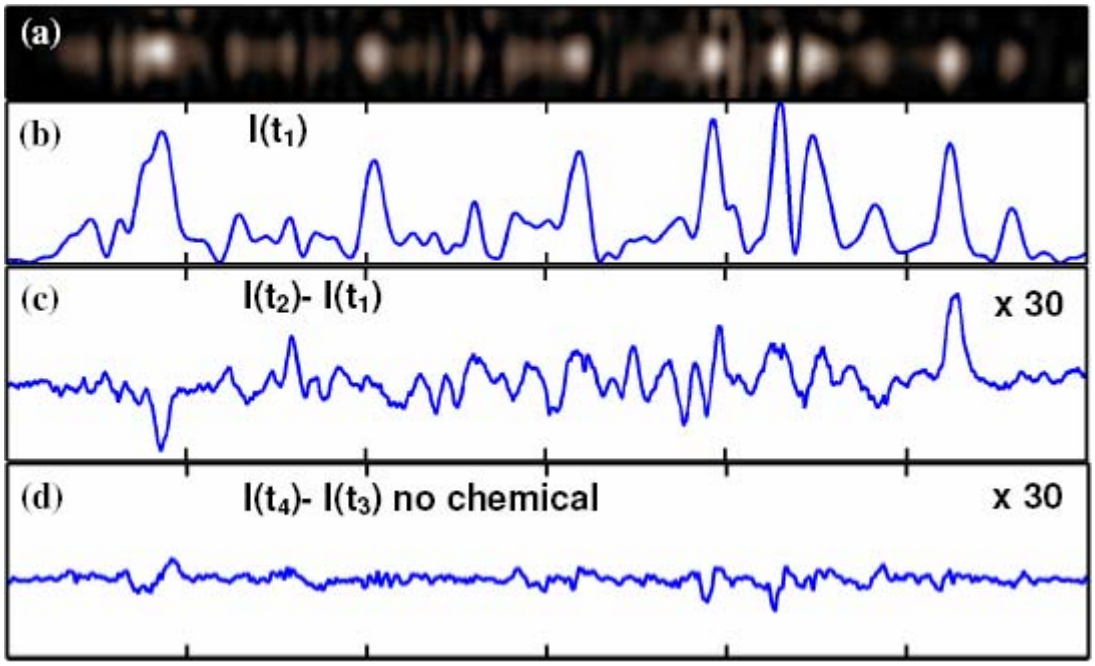

Figure 35 Representative multimode patterns from an interferometric sensor capture by a CCD camera. (a) Typical CCD image. (b) Corresponding 1-D intensity profile. (c) Intensity difference profile between 0 and 37 ppbv methanol. (d) Pixel power diffence over time for no agent inserted into the system. [71]

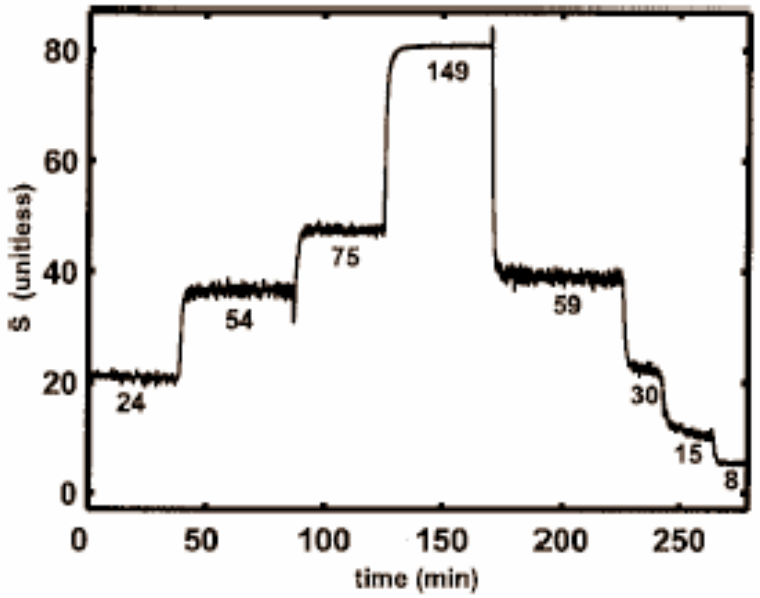

Figure 36 Aggregate responses of all pixels, as quantified by the root-mean-square signal-to-noise ratio of all the pixels (S). Agent concentration over time is indicated at the plot plateaus. [71]

4.2 Integration of Optical Components on Si CMOS

As mentioned previously, a fully integrated sensor solution would provide a superior performance over a non-integrated sensor. Key to that integration was the CMOS circuitry that the interferometric sensor was integrated on. These CMOS circuits provided lateral pnp bipolar junction transistor (BJT) photodetector arrays and low noise analog front-ends for signal conditioning and photodetector support. The CMOS output was handled by an array of parallel mixed-signal oversampled noise-shaping analog-to-digital converters (ADC). [72] The BJT photodetector array had a detector pitch-to-pitch of 8 μm, an array width of 192 μm, and a well size of 8x 8 μm^2. The detectors had a measured responsivity of 0.12 A/W at λ=632.8 nm and a dark current less than 10 pA. [41] The front-ends were used to stabilize voltage biasing using photocurrent feedback. The ADCs were Delta-Sigma modulators. These ADCs provided a multibit resolution, highly linear digital output of the photocurrent signal of the photodetectors. [72]

A process for integrating the interferometric sensors on the Si CMOS circuits has been developed for this thesis. The process began by spin coating Cyclotene 4022 advanced electronic resin (photosensitive BCB) on Si CMOS circuits. One of the key considerations in the selection of BCB was its relatively low cure tepurature, 240 °C. At this temperature, there was little to no impact on the performance of the CMOS circuitry. This layer of BCB was used to protect the circuit pads and the electronics on the circuit during the subsequent processing steps. The photosensitive BCB is patterned to protect these areas while removing it from the areas that will hold the interferometers. The BCB was then cured using the profile detailed in Table 1. Following the cure, a protective

Table 2 BCB cure cycle.

Initial	1 ^{0}C/min to 50 ^{0}C	5 min
Ramp	3 ^{0}C/min to 100 ^{0}C	15 min
Ramp	3 ^{0}C/min to 150 ^{0}C	15 min
Final Cure	2 ^{0}C/min to 240 ^{0}C	60 min

layer of approximately 3 μm thick BCB remained over the pads and the electronics. The waveguide layers were then deposited on the circuit using an STS PECVD. A lower cladding layer of silicon dioxide with a thickness of 1 μm was deposited first. The waveguiding core of silicon nitride was deposited next. This layer varied in thickness depending on the design of the sensor, but typically a thickness of 0.5 μm was used. A final layer of 1 μm thick silicon dioxide was deposited to complete the structure. The interferometers were then defined by etching out on the surface of the circuit, following the patterning of photoresist on the surface of the waveguide layers. A PlasmaTherm ICP was used to etch out these structures. The etches performed in the ICP were all timed etches. The etch rates of the materials etched were well known and made this the easiest method for performing these etches. Care was taken to etch completely through the waveguide layers since the electrical contact pads must be accessible upon completion of the integration. The circuit was then patterned again using photoresist, and channels were etched into one of the arms of each interferometer using the ICP. These channels defined one arm as a sensing arm. This etch removed the silicon dioxide layer from the sense arm. An oxygen plasma was then used to remove the BCB protective layer in a PlamaTherm RIE. Finally, a sensing layer was selectively deposited using standard photolithography techniques. The use of standard photolithography produced a well-defined sensing layers that are easily integrated into the fabrication process. A Si CMOS integrated circuit with integrated MZI sensors can be seen in Figure 37.

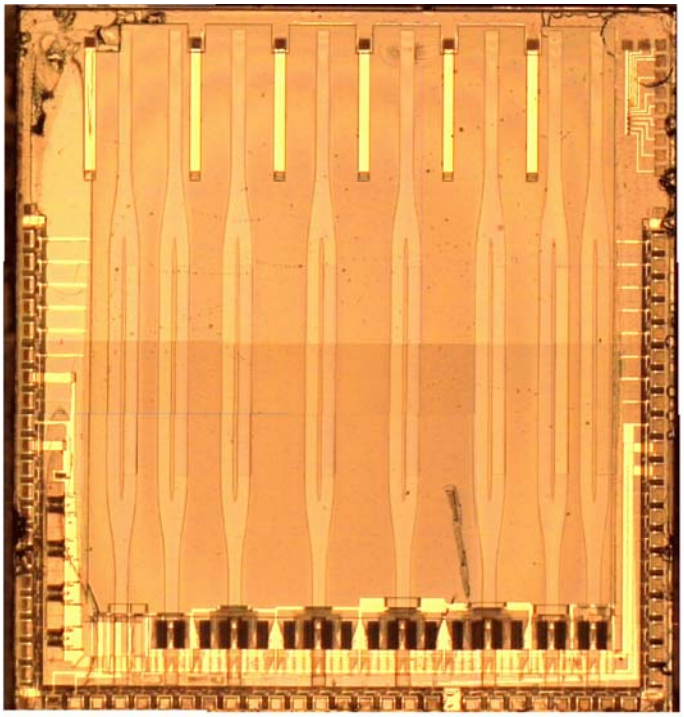

Figure 37 Integrated Si CMOS circuit with integrated Mach-Zehnder interferometric sensors.

The CMOS circuits were tested electrically and optically prior to integration with the interferometric sensors. Electrically, the sensitivity of the circuit was determined. Current biasing was provided by two Keithly 236 source and measurement units. A Tektronix DG2020A pattern generator was used as the clock and a National Instruments PCI-DIO-32HS digital data acquisition unit was used as a data sink. The electrical sensitivity of the circuit was found to be less than 10 pA. This limit was not necessarily that of the circuit as the current source accuracy used in the measurement was less than 230 pA for the measurement range. [73] The circuits were also tested optically. A lensed single mode fiber was used to couple 850 nm laser light into a photodetector in the detector array. The laser power was calibrated using a Newport 1835-C optical power meter. The delta-sigma converter output from the detectors was then recorded and analyzed. The circuit was found to have an optical sensitivity less than 10 nW. Assuming the circuits were linear, it was possible to extrapolate that the circuits ultimately could detect 100 pW optical power against the noise. [73]

Results were not obtained from these integrated circuits. The interferometric sensors on these circuits were coated with HFAPNB on their sensing arms. The sensors were then used to simply measure the changing humidity in the test chamber. No meaningful data was recorded. The failure of these tests was most likely due to a lack of coupling between the circuits and the interferometric sensor. As stated earlier, the main coupling mechanism used in this research was evanescent coupling. As designed, the field in the interferometric sensors extended approximately 1 μm outside of the waveguide core. The CMOS detectors used in this work were located 2 μm below the surface of the circuit. Due to this discrepancy, there was no communication possible between the sensors and the circuit. Though it is believed that the integration scheme illustrated in this thesis can successfully be used to integrate Si CMOS circuitry with interferometric sensors; it was not possible to show that the integration scheme worked.

4.3 Thin-Film Laser Development

Thin-film lasers offered several advantages over on-wafer lasers during the course of this research. First and foremost, thin-film lasers lend themselves to heterogeneous integration more readily than on-wafer lasers. A heterogeneous approach allows for optimization of the optical components versus the non-optical components. In this work, all of the processing circuitry was fabricated in silicon, the waveguides were constructed out of dielectrics, while the active laser components were fabricated in the GaAs/AlGaAs system. On-wafer lasers also required wire bonds to be integrated into a heterogeneous system. These wire bonds are subject to parasitics at high speeds which increase the power consumption of the entire system. Thin-film lasers do no suffer from these same parasitic as they can be bonded directly to the substrate and powered without the use of

wire bonds. Thin-film lasers also provided a higher ease of integration with a multi-material system than the on-wafer lasers. The size of the thin-film device was on the order of optical components used in the system and allowed for simple coupling methods to be used with the waveguides. On-wafer lasers were much larger and required more components to couple light into a waveguide.

The first step in thin-film laser development involved a review of current GaAs laser technology. The purpose of this review was to find a suitable laser structure for this research. The sensor required a coherent light source. Speed requirements were in the MHz range in order to produce a sensor that would detect at a reasonable rate. The power budget called for a 1-5 mW source. These power levels would be sufficient for powering the sensor and a average laser of these spec would have relatively low threshold currents and power consumption. A structure that met all of these requirements was found [74] and this structure was adapted for thin-film integration. Figure 38 details the final structure submitted for epitaxial growth. These epitaxial layers were grown on a bulk n-type GaAs substrate. The main difference between this design and the reference paper was the presence of a thin layer of AlAs. This layer of AlAs was used as a sacrificial layer during substrate removal in the thin-film process. Other than this subtle change, the two structures are identical.

	Layers	Thickness in μm
13	p^+ - GaAs -2×10^{18}	0.2
12	p - $Al_{0.55}Ga_{0.45}As$ - 6×10^{17}	1.3
11	$Al_{0.35}Ga_{0.65}As$	0.065
10	GaAs	0.0075
9	$Al_{0.35}Ga_{0.65}As$	0.008
8	GaAs	0.0075
7	$Al_{0.35}Ga_{0.65}As$	0.008
6	GaAs	0.0075
5	$Al_{0.35}Ga_{0.65}As$	0.065
4	n - $Al_{0.55}Ga_{0.45}As$ - 1×10^{17}	1.3
3	n^+ - GaAs – 1×10^{18}	0.2
2	n^+ - AlAs - 1×10^{18}	0.2
1	n - GaAs - 1×10^{18}	0.5

Figure 38 Layer structure of GaAs multiple quantum well laser grown by molecular beam epitaxy for use in thin-film laser development

In preparation for thin-film development, on-wafer lasers were fabricated to verify the quality of the material and build a process that could be adapted for the thin-film process. Samples approximately 5 mm on a side were cleaved from the laser wafer. Negative photolithography was then performed to pattern the laser contacts. The stripes measured 243 or 343 microns in width and are spaced 100 microns apart. The electron beam evaporator was then used to deposit 250 Å of Ti and 2250 Å of gold as the contacts. The Ti layer promotes adherence of the gold contact layer to the semiconductor material. Metal liftoff was then performed by immersing the sample in acetone. The samples were soaked overnight and the undeveloped photoresist was dissolved. The metal in these areas lifts off of the sample, leaving TiAu only where the contacts are supposed to be. BCB was then deposited on the sample following the application of a BCB adhesion promoter, AP3000. Dow CYCLOTENE is the BCB that is used. The BCB was spun on at 4000 rpm for 30 seconds. This obtained a layer of BCB that was approximately 1.1 μm. The BCB provided electrical isolation of the contact pads as well

as planarization of the surface of the semiconductor. The BCB was then cured using the process detailed in Table 1. The cure drove out any of the remaining solvent in the polymer and hardened the film so that it would be resistant to the subsequent processing steps. Aluminum was then deposited on the sample using a thermal resistance evaporator. This aluminum layer was used to protect the BCB in the subsequent etch steps. Negative photolithography was performed to define a via to the contact pads beneath the BCB. The via was 10 microns in width. The via was etched out of the aluminum using PAN etch. The via was then etched through the BCB using an SF_6:O_2 (90:10) plasma in a PlasmaTherm reactive ion etcher (RIE). Upon completion of the via etch, the stripe contact pad was patterned on the samples using negative photolithography. This broad area contact made probing the laser stripe easier. The ebeam evaporator was used to deposit Ti/Pt/Au (250Å/250Å/2500Å) on the laser sample. Metal liftoff was performed to finish the contact patterning. The laser sample was then placed in a rapid thermal processing (RTP) system and a low temperature (30 minutes at 210 °C) anneal was performed. The purpose of this anneal was to improve the ohmic contacts formed between the metal and the material. Improved ohmic contacts will result in better electrical conductivity and lower threshold currents. After the anneal, the laser sample was cleaved into bars of approximately 300 microns in length. A cross-section view of the on-wafer laser can be seen in Figure 39.

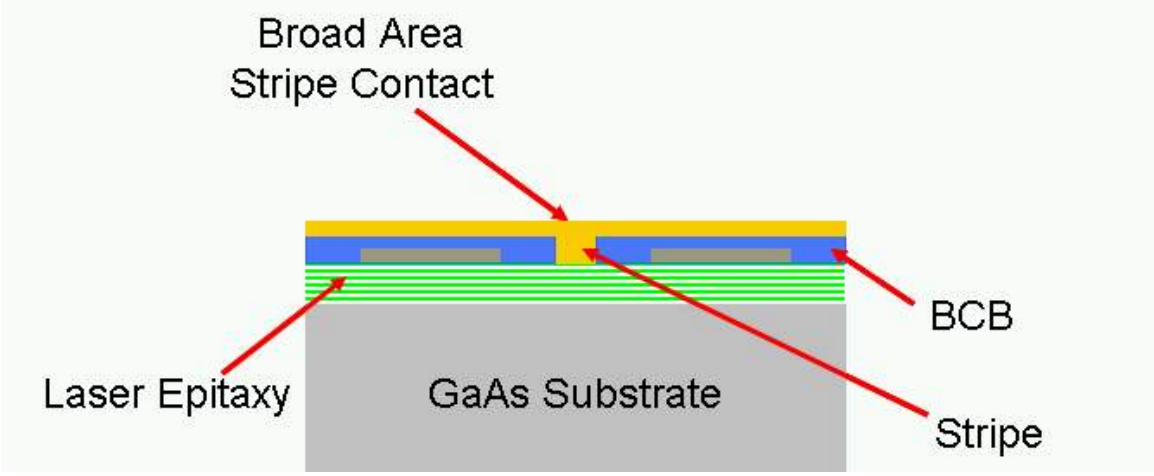

Figure 39 Cross section of a completed broad area laser.

Each laser bar was then tested to verify its operation. Each bar consisted of 4 or 5 lasers separated by 100 microns. The non-metallized side of the bar was mounted on the edge of a copper block using indium solder. Each laser was probed by contacting the common indium solder contact and the appropriate stripe contact. An ILX Lightwave LDP-3811 was used to drive the lasers. A 100 μs pulse was used with a 20% duty cycle. Light was collected by a large-area silicon detector that was mounted as close as possible to the edge of the lasers. The detector was connected to a Tektronix oscilloscope and the current output from the detector was monitored. Using the responsivity of the detector, which had been measured prior to the experiment, it was possible to determine the output power of the laser. A typical LI curve measured during these test can be seen in Figure 40. The threshold current is approximately 60 mA and the output power is well within the requirements of the sensor. After successful fabrication of an on-wafer laser, thin-film laser development began.

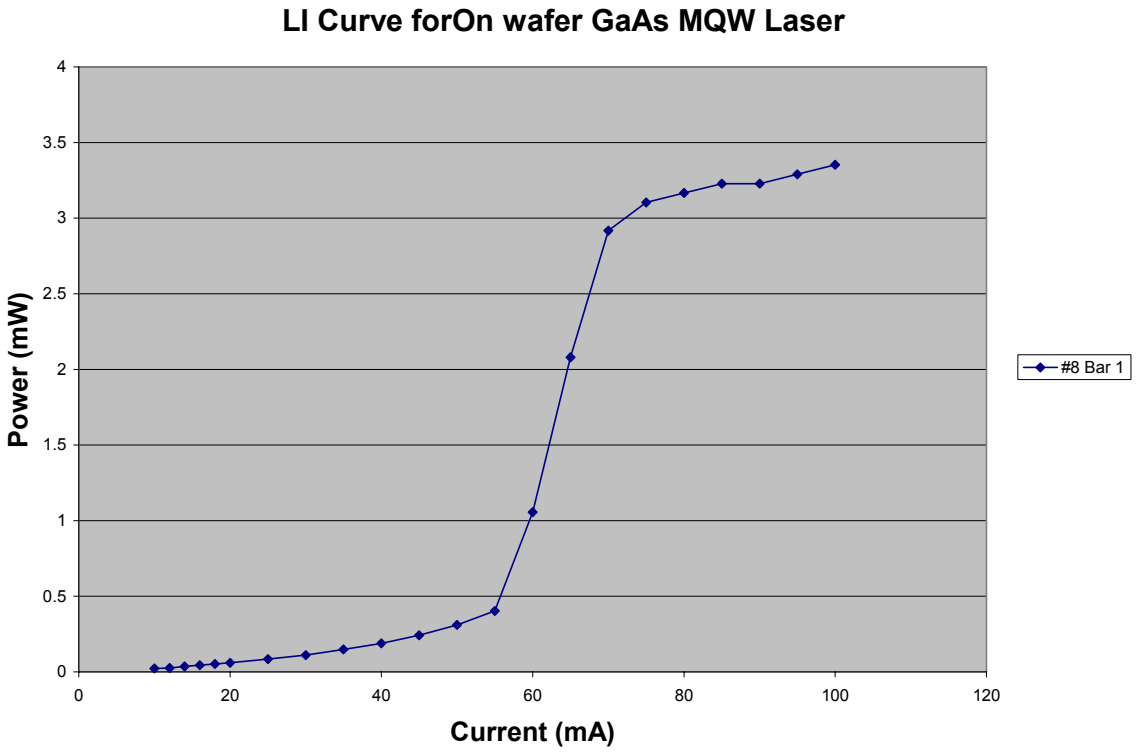

Figure 40 LI curve for an on wafer GaAs MQW laser.

A process for fabricating and integrating thin-film lasers has also been developed. The thin-film laser process begins by cleaving a sample of the semiconductor laser material from the wafer. The sample is then mounted to a glass slide using Apiezon W black wax. This is done to enable easier handling of the sample. The sample is then cleaned using trichloroethylene (TCE), acetone, and methanol. The solvent clean removes any organic films or residues that are on the wafer. Next, a negative photolithographic process is performed to pattern contacts on the bare semiconductor. The contacts measure 300 microns in width and are spaced 100 microns apart. Lengths of the contacts are determined by the spacing the wedges used to assist in laser cleaving. Each wedge was approximately 100 μm in length. The mask set used has laser lengths of 300, 400, and 500 μm. Following the photolithography, the electron-beam evaporator

was used to deposit Ti/Au on the sample. Two hundred fifty angstroms of titanium is deposited followed by approximately 3000 Å of gold. Metal liftoff is then performed. Individual laser bars are then isolated from each other by a mesa etch. The mesa etch used for GaAs based devices is H_2SO_4:H_2O_2:H_2O (1:8:200). The device structure is etched down to the AlAs sacrificial layer. The etch used was a timed etch as the etch does not stop on AlAs. First a short etch was performed to determine the etch rate of the AlAs in the solution. After the etch rate was determined, the remaining structure was etched to the final depth of 3.1685 μm, the total thickness of the epitaxial laser structure. Once the devices are isolated, Apiezon W black wax is melted on top of the samples. The wax is used as a handling layer for lasers following substrate removal and laser cleaving. Substrate removal is achieved by immersing the samples in 10% HF for at least six hours. There is a large selectivity ($>10^8$) [75] between the GaAs layers and the AlAs layer. This allows the AlAs layer to be selectively and laterally etched without affecting the surrounding GaAs material. Once the AlAs is completely etched away, the black wax encased device floats away from the GaAs substrate. The thin-film devices are removed from the etch and are then attached to a thin piece of flexible metal. The metal is used to flex the laser bars along the crystal axis. The wedge cuts in the material promote cleaving at those locations. The devices are then placed on a transfer diaphragm. The transfer diaphragm is simply a silicon ring with a transparent mylar film stretched across the opening. The mylar is attached with baked photoresist. The devices are attached to the transfer diaphragm using a drop of de-ionized water and they are allowed to dry. The black wax is removed by immersing the diaphragm in TCE. Once all the wax is

removed, cleaved lasers remained on the transfer diaphragm. The lasers are then ready to be transferred to various substrates for integration.

Thin-film laser integration began with the deposition of a bottom laser contact on a silicon substrate. This is achieved by using negative photolithography to define the contact location. The ebeam evaporator was then used to deposit 250 Å of titanium followed by 2250 Å of gold. Liftoff procedures were then employed to define the TiAu pads. Lasers were transferred to these pads using the Mylar transfer diaphragm. Polyimide was then deposited on the sample following the transfer of the laser to the bottom contact pad. HD Microsystems PI2610 is used. The polyimide was spun on at 4000 rpm for 45 seconds. At this viscosity, a layer of polyimide that was approximately 1.1 μm is obtained. The polyimide provided electrical isolation of the contact pads. The polyimide, hypothetically, also improved electrical connectivity by pushing the device completely down on the pads. The polyimide was then cured in order to ensure resistance to the subsequent processing steps. This cure is detailed in Table 2.

Table 3 Polyimide cure cycle

Temperature Ramp	3°C/min.
Initial Process	130°C for 30min.
Pre-cure	250°C for 30min.
Final cure	350°C for 60min.

Aluminum was then deposited on the polyimide coated surface using the thermal resistance evaporator. This Al layer was used as a mask layer for subsequent processing steps. Negative photolithography was again performed to pattern the stripe on the surface. The photoresist was then used as a mask, while a stripe window in the Al is etched using PAN etch. The polyimide was then etched using a SF_6/O_2 plasma in the

RIE. Once the stripe was open in the polyimide, the aluminum mask was removed using Microposit 351 developer. Negative photolithography was then performed to define to the top contact. AuGe/Ag/Au was deposited as a top contact using the thermal resistance evaporator. Metal liftoff was again performed to pattern the AuGe/Ag/Au contact. A rapid thermal anneal was then performed to improve the ohmic contacts. This completed the integration of the thin-film laser. A cross-sectional view of the laser can be seen in Figure 41.

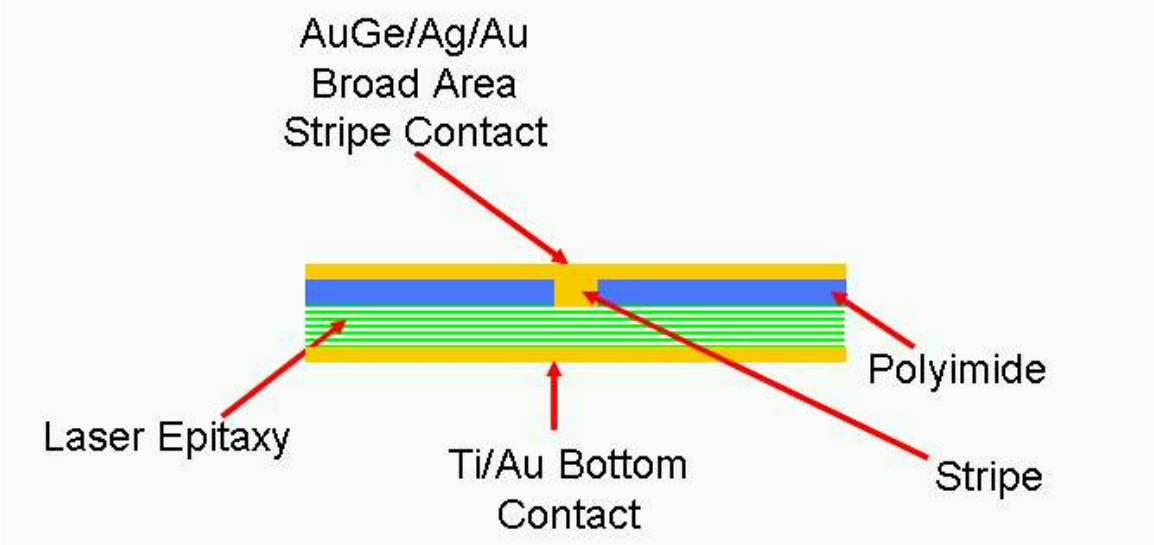

Figure 41 Cross sectional view of fabricated tin film laser.

Figure 42 illustrates a fabricated thin-film laser. Figure 42a shows the fabricated lasers while Figure 42b shows the illuminated laser under bias. Figure 43 shows the LI curve obtained during operation of the laser. The laser was pulsed using an ILX Lightwave IDP-3811 current source. A 100 μs pulse length and a 20% duty cycle was used. Light was collected using an integrating sphere and measured using a Newport 1835-C optical power meter with a calibrated photodetector. Two distinct slopes are

present in the curve and a knee is present. While it possible that the device is lasing, without measuring the spectrum of the device, it is not possible to say definitively. Regardless, the poor LI curve is due to low thermal diffusivity of the thin-film device. [76-78] By removing the substrate, the thermal diffusivity of the device decreases by 5-7 times. Since heat is no longer transferred efficiently through the device, the build up in heat cause degradation in the device performance. Several researchers have shown this phenomenon in the literature. [79-81] The results of this work show similar trends.

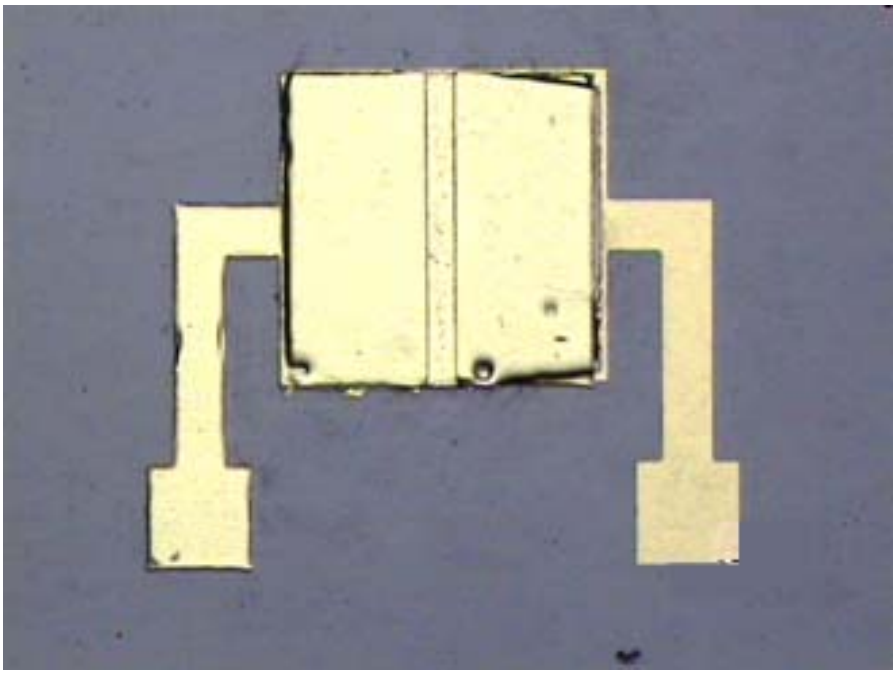

(a)

(b)

Figure 42 Thin-film laser. (a) Completely fabricated laser. (b) Illuminated laser under forward bias.

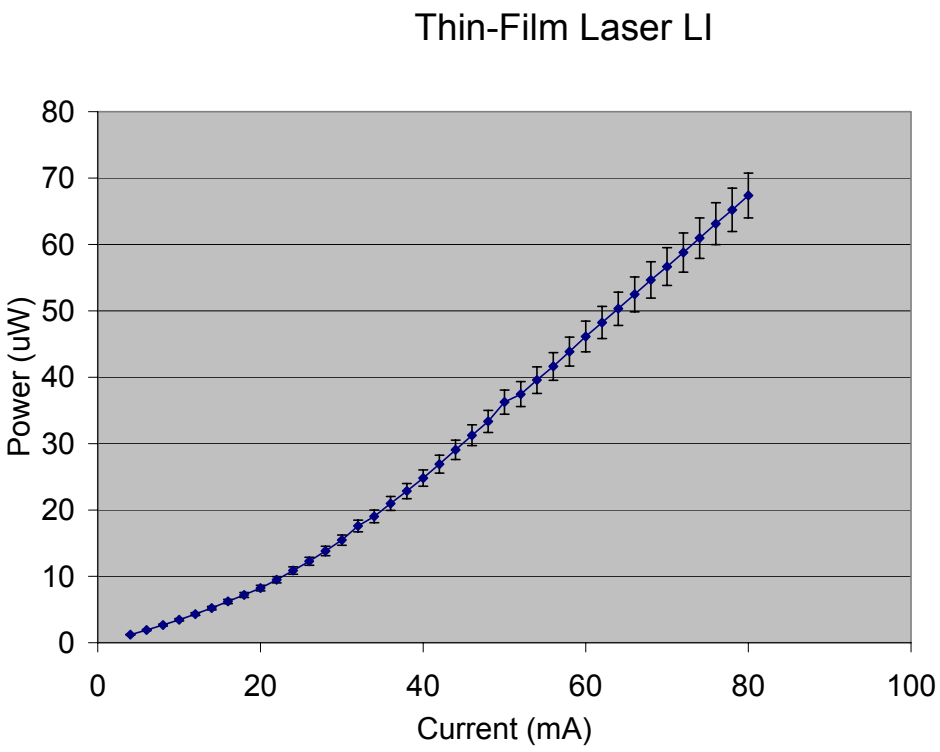

Figure 43 Li curve for thin-film laser diode.

4.4 Summary and Discussion

The fabrication of the relevant sensor technology used in this dissertation was presented in this chapter. The first section reviewed the fabrication techniques used in the creation of the waveguide interferometers used in this research. Also presented is a discussion of the sensing layer and the testing methodology used in the research. Results obtained from the interferometric sensor created were also presented. The second section detailed the results obtained when integrated the interferometric sensor onto silicon CMOS circuitry. The integration process is detailed and the results obtained from the integration were discussed. Ultimately, the integration was unsuccessful perhaps, due to the CMOS detectors being to far from the surface of the circuit. The evanescent field does not extend far enough outside the waveguide to intersect with the detector. The final section looked at the fabrication and characterization of the thin-film MQW edge emitting lasers. Each fabrication step was detailed and the results obtained for the original on-wafer laser and the thin-film devices were presented.

Chapter 5

Theoretical Model of the Integrated Sensor

5.1 Laser simulation

5.1.1 Simulation methodology

Laser simulations were performed using ALDS. ALDS stands for advanced laser diode simulator. [82] Physically, ALDS views a semiconductor laser as a block diagram,

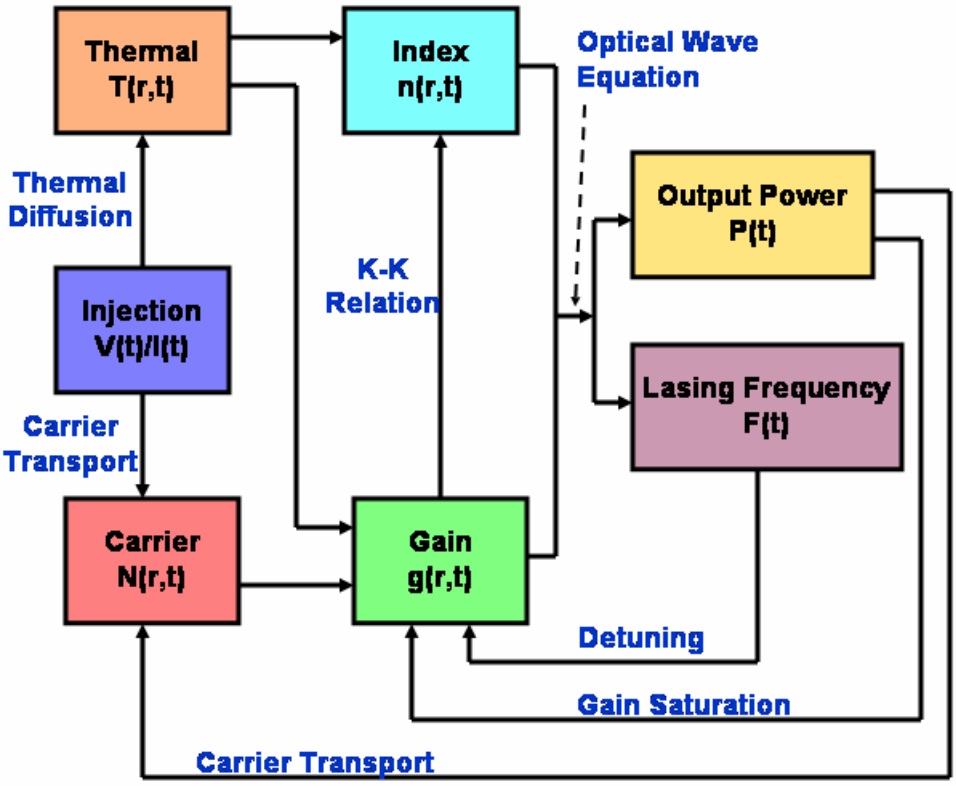

Figure 44 Schematic drawing of a general semiconductor laser model. [82]

as shown in Figure 44. In this analysis, current is injected into the laser through the laser contact. The current generates electron-hole pairs in the laser cavity. These electron hole pairs can recombine radiatively (gain) or non-radiatively (thermal). Heat generated during non-radiative recombination can lead to changes in the index of refraction of the lasing materials and can impact the overall gain of the lasing medium. Variations in the gain directly impact the index of the lasing material. By taking into account, material refractive index and the gain function of the lasing structure, the output power and the lasing frequency can be determined. Feedback from these two blocks directly impacts the gain of the laser, while the output power also impacts the carrier concentration of the laser medium. Each of the relationships outlined above are clearly defined in equation form. For this research, light-current relationships were established for several different lasing geometries. A brief discussion of the equations and methodology relevant to these simulations will be detailed below.

ALDS uses a hierarchical approach in solving simulation problems. [82] This approach is used to decouple the localized cross-sectional equations from the fast-varying global longitudinal equations along the light propagation direction. To achieve this goal, the simulation is divided into several different levels. Calculations can be made at each level with less complicated constraints and verification of the results can be done far more easily than in a unified approach since the levels are decoupled from each other. An added robustness of this approach is that missing parameters do not immediately cause the simulation to fail. As long as these parameters are simulated by another block in the simulation or entered before the end of the simulation, a self consistent solution can still be obtained. Even omitting some parameters does not invalidate the results. Since

the various characteristics of the simulated device are independently contained within discrete blocks, the overall solution can still be obtained without the missing data.

The layout of the data input engine of ALDS can be seen in Figure 45. The first

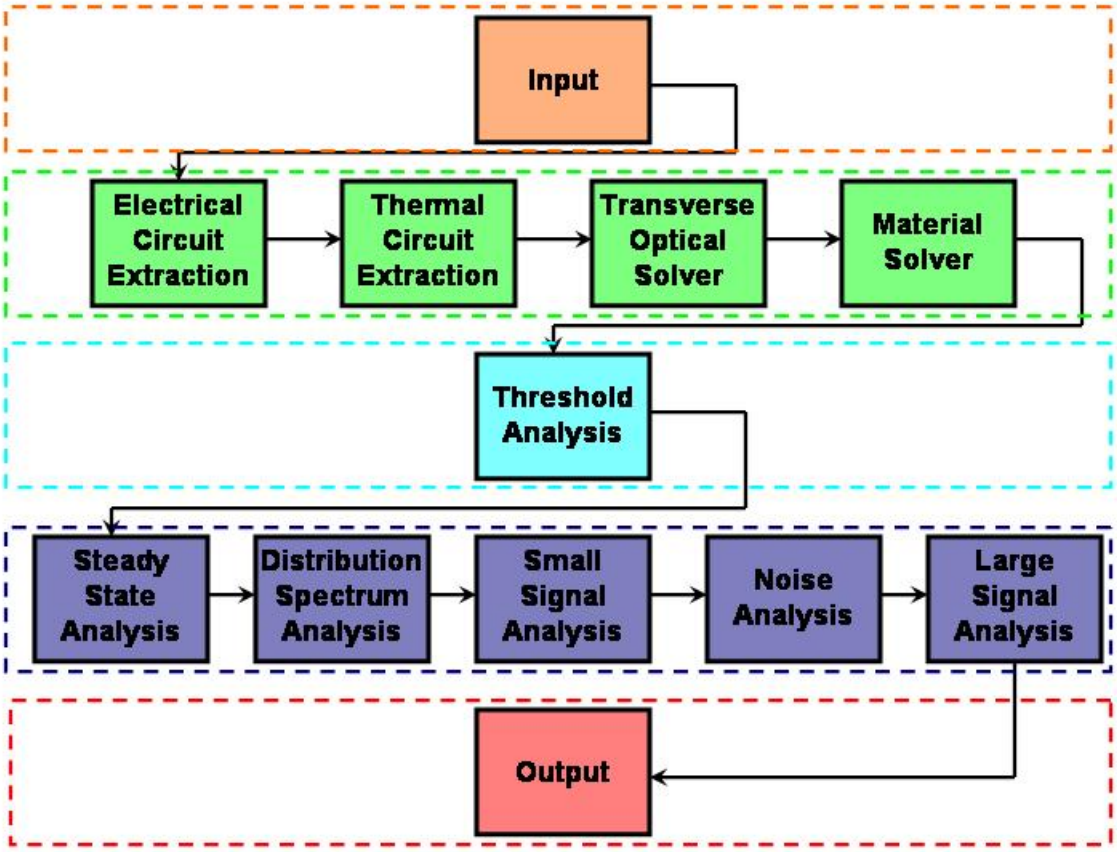

Figure 45 Layout of the ALDS data input engines.

data block represented by orange contains all the data relevant to structural input. The green modules are responsible for making calculations concerning the structure and the material. The turquoise data block handles threshold analysis. The blue modules calculate parameters regarding system performance. The last block is responsible for outputting the data in a graphical format. The blocks must be run in order as the

simulation data is built from inputs of previous blocks. For this research, the flow was followed all the way to the small signal analysis tool.

The first data input into the ALDS engine are the geometric dimensions of the structure and the underlying material system. The length of the active region is input, as well as the reflectivities of the mirrored facets of the laser. This is all the data required for a 1-D treatment of the laser. For three dimensional treatments, it is necessary to input individual material layers and their respective thicknesses. The AlGaAs/GaAs system is included in the material library of the simulator. Using this library, physical parameters such as band gap, index of refraction, and strain are calculated. The doping concentration of the material layer is taken into account. Specific parameters for the AlGaAs layers are calculated as a function of aluminum concentration. The geometry of the laser contact is also input, along with the contact material system. This is the bare minimum user input required to run the ALDS tool. This data is passed to the material and structure solver to calculate the basic lasing parameters.

The most relevant modules used in this research are the transverse optical solver, the material solver, the threshold analysis module, and the steady state analysis module. The underlying equations solved in these modules will be discussed below. The transverse optical solver calculates the optical modal parameters. These include the cross-sectional mode profile, the effective index, the group index, the confinement factor, the index and the gain/loss coupling coefficients. The far field patterns are also calculated.

The general governing equations of the optical field distributions in semiconductor lasers is given as [83]

$$\nabla^2\Psi(r,t)+k^2\left[n^2(r)-j\frac{\bar{n}}{k}\alpha(r)+\frac{\bar{n}}{k}g(r,t)\right]\Psi(r,t)=j\frac{2\overline{nn}_g\omega}{c^2}\frac{\partial}{\partial t}\Psi(r,t)-\mu_o\omega^2 f_s(r,t)$$

[20]

where Ψ is the slowing varying dominant component for the transverse electric field and r is the position vector expressed in rectangular coordinates and *k* is the reference wavenumber, *2π/λ*.. In this configuration, the laser waveguide axis lies along the z axis. The laser optical frequency is given by ω, c is the speed of light in free space, and μ_0 is the magnetic permeability in free space. The functions g(r,t), f_s(r,t), and α(r) are the optical gain distribution, the spontaneous emission noise, and the optical loss distribution respectively. The last two parameters are given by $\bar{n}$ and $\overline{n_g}$. These two parameters are the average index and the average group index respectively and are given by

$$\bar{n}=\int_0^L\int_\Sigma n(r)dv/L\Sigma \qquad [21]$$

$$\bar{n}_g=\int_0^L\int_\Sigma n_g(r)dv/L\Sigma \qquad [22]$$

where L is the cavity length and Σ is the cross sectional area of the laser. The total optical field in the laser cavity may be expressed as [83]

$$\Psi(r,t)=\sum_m C_m\sqrt{S_m(t)}\exp\{j\varphi_m(t)\}\Phi_m(z)E(x,y) \qquad [23]$$

where E(x,y) is the transverse optical field profile of the local mode, Φ_m(z) is the longitudinal optical field amplitude, and S_m(t) and φ_m(t) are the photon number and phase numbers respectively. C_m is a normalization factor. By substituting Equation 23 into

Equation 20, an eigenvalue equation can be obtained. The transverse optical solver solves this eigenvalue equation using the finite difference method, which is given by [83]

$$\nabla_t^2 E(x,y) + k^2 \left[n^2(x,y,z) - n_{eff}^2(z) \right] E(x,y) = 0 \qquad [24]$$

where $n_{eff}(z)$ was the local modal effective index of the laser waveguide. The solutions of this equation gave the cross sectional optical field and the effective index. The module calculated the far field pattern from this data using a fast Fourier transform (FFT) combined with a polishing algorithm based on the sampling theory used by ALDS. The polishing algorithm repaired data imperfections so the FFT would not have to deal with data outliers and noise in the analysis. This data smoothing allowed for simpler calculations and faster data analysis. The other parameters are determined by calculating the overlap integrals of these functions.

The next module used was the material solver. This block calculated the cross sectional material optical gain, the index change, the linewidth enhancement factors, and the material optical losses of the laser. In order to determine these values, the wave functions and E-k (energy-momentum) dispersion relations in the conduction band were determined by solving the Schrödinger equation. The wave functions and the E-k dispersion relations in the valence band were calculated by solving coupled Schrödinger equations. The calculated wave functions and E-k relations are then used to calculate the material optical TE and TM gain using

$$g(\omega) = \frac{q^2}{c\varepsilon m_0^2 \omega L_z} \sum_{n,\sigma} \sum_{l,m} \int_0^\infty k dk M_{lm}^{\eta\sigma}(k) \frac{\left(f_c^1 - f_{v,\sigma}^m \right) \Gamma_t / (2\pi)}{\left[E_l^c(k) - E_m^{v,\sigma}(k) - E_g - \hbar\omega \right]^2 + \left(\Gamma_t / 2 \right)^2} \qquad [25]$$

where Γ_t is the Lorenzian linewidth broadening factor caused by intra-band scatterings, L_z is the well width, σ is the upper and lower blocks of the Hamiltonian, η is the electron spin state, l,m are the sub-band indices, $M_{lm}^{\eta\sigma}$ is the optical dipole matrix element between the lth sub-band in the conduction band with a spin state η and the mth sub-band in the valence band of the 2x2 Hamiltonian H^{σ}, $f_c^1, f_{v,\sigma}^m$ are the Fermi functions for the lth sub-band in the conduction band and the mth sub-band in the valence band of H^{σ}, respectively, and $E_c^1, E_m^{v,\sigma}$ are the lth sub-band energy in the conduction band and the mth sub-band energy in the valence band of H^{σ} at k, respectively. The material index change is calculated using the Kramers-Kronig (K-K) transformation given by

$$\Delta n(\omega) = -\frac{c}{2\pi\omega}\int_{-\infty}^{+\infty}\frac{g(\omega')}{\omega'-\omega}d\omega' \qquad [26]$$

The linewidth enhancement factor can then be calculated using

$$\alpha(\omega) = \frac{\frac{2\omega}{c}\left[\frac{\partial\Delta n(\omega)}{\partial N}\right]}{\left[\frac{\partial g(\omega)}{\partial N}\right]} \qquad [27]$$

Once these calculations are completed, the material optical losses are calculated. The following five guidelines are used for these calculations: 1. Excitations from the conduction band minimum into higher-lying minima, excitations from the donor levels into the conduction band are neglected; 2. Free carrier absorption due to semi-classical plasma effects; 3. Excitations from lower lying bands into holes near the valence band maximum; 4. Excitations from the valence band into acceptor levels; 5. Optical scattering loss in the waveguide. Using those guidelines, the material losses can be calculated by

performing an overlap integral between the total material loss distribution and the optical field intensity distribution over the entire cross section of the laser structure.

Threshold analysis is then performed in the next block. Threshold current and spectral information of the laser are calculated. The information from the previous blocks is used to make these calculations. Using these parameters the coupled mode equations, the photon number and the photon phase rate equations, and the carrier rate equations are solved self consistently. The coupled mode equations are given by [83]

$$\frac{d}{dz}R_m(z) = -j\gamma_m(z)R_m(z) - j\kappa_m L_m(z) \qquad [28]$$

$$\frac{d}{dz}L_m(z) = j\gamma_m(z)L_m(z) - j\kappa_m R_m(z) \qquad [29]$$

where γ_m (z) is the complex gain, κ_m(z) is the complex coupling coefficient, and R_m(z) and L_m(z) are the amplitudes of the forward and backward propagating waves in the laser chamber. The photon phase rate equations are given by [83]

$$\frac{d}{dt}S_m(t) = \frac{\omega}{\overline{nn_g}}\mathrm{Im}(\xi_m)S_m(t) + \frac{c}{\overline{n_g}}\sum_n \mathrm{Im}\left\{\frac{\int_0^L \Delta g^{\mathrm{mod}\,al}(z,t)\Phi_m(z)\Phi_n(z)dz}{\int_0^L \Phi_m^2(z)dz}\right\}S_n(t) + R_m^{sp}(t) \qquad [30]$$

$$\frac{d}{dt}\varphi_m(t) = \frac{\omega}{2\overline{nn_g}}\mathrm{Re}(\xi_m) + \frac{c}{2\overline{n_g}}\sum_n \mathrm{Re}\left\{\frac{\int_0^L \Delta g^{\mathrm{mod}\,al}(z,t)\Phi_m(z)\Phi_n(z)dz}{\int_0^L \Phi_m^2(z)dz}\right\} \qquad [31]$$

where g^{modal}(z) is the modal gain, $R_m^{sp}(t)$ is the spontaneous noise emission rate, ξ_m is the eigen value of the mth longitudinal mode. The carrier rate equations for a MQW active

region are defined according the different sections of the laser structure. The areas include the top separate confinement double heterostructure (SCH) layers, the well regions, the barrier region, and the bottom SCH layer. The top and the bottom SCH are assumed to be adjacent to the upper and lower cladding regions in the laser structure. The wells and the barriers are located in between the two SCH layers. Given this structural arrangement, the carrier rate equations are given by

1. The top SCH layers

$$\frac{d}{dt}N_{SCH}^{T}(z,t)=\frac{I_{ar}(z,t)-I_{l}}{q\sum_{SCH}^{T}L}-\frac{N_{SCH}^{T}(z,t)}{\tau_{d}}+\frac{N_{Wl}^{3D}(z,t)}{\tau_{d}}-R_{nr}\left[N_{SCH}^{T}(z,t)\right] \quad [32]$$

2. The jth well (j=1,2,3…N_w)

$$\frac{d}{dt}N_{Wj}^{3D}(z,t)=\frac{X}{\tau_{d}\left(D_{Wj}/D_{SCH}^{T}\right)}-\frac{2N_{Wj}^{3D}(z,t)}{\tau_{d}\left(D_{Wj}/D_{SCH}^{T}\right)}+\frac{N_{Bj(z,t)}}{\tau_{d}\left(D_{Wj}/D_{SCH}^{T}\right)} \quad [33]$$
$$-\frac{N_{Wj}^{3D}}{\tau_{j}^{C}}+\frac{N_{Wj}^{2D}}{\tau_{j}^{E}}+R_{nr}\left[N_{Wj}^{3D}(z,t)\right]$$

$$\frac{d}{dt}N_{Wj}^{2D}(z,t)=\frac{N_{Wj}^{3D}}{\tau_{j}^{C}}-\frac{N_{Wj}^{2D}}{\tau_{j}^{E}}-R_{nr}\left[N_{Wj}^{2D}(z,t)\right]-R_{st}\left[N_{Wj}^{2D}(z,t)\right] \quad [34]$$

3. The jth barrier (j=1,2,3…N_w)

$$\frac{d}{dt}N_{Bj}(z,t)=\frac{N_{Wj}^{3D}(z,t)}{\tau_{d}\left(D_{Bj}/D_{SCH}^{T}\right)}-\frac{2N_{Bj(z,t)}}{\tau_{d}\left(D_{Bj}/D_{SCH}^{T}\right)}+\frac{N_{Wj+1}^{3D}(z,t)}{\tau_{d}\left(D_{Bj}/D_{SCH}^{T}\right)} \quad [35]$$
$$-R_{nr}\left[N_{Bj}^{3D}(z,t)\right]$$

4. The bottom SCH layers

$$\frac{d}{dt}N_{SCH}^{B}(z,t) = -\frac{N_{SCH}^{B}(z,t)}{\tau_d\left(D_{SCH}^{B}/D_{SCH}^{T}\right)} - \frac{N_{WN_w}^{3D}(z,t)}{\tau_d\left(D_{SCH}^{B}/D_{SCH}^{T}\right)} - R_{nr}\left[N_{SCH}^{B}(z,t)\right] \qquad [36]$$

where N_w is the total number of quantum wells in the laser structure, X = $N_{SCH}^{T}(z,t)$ for the 1st well and X = $N_{Bj-1}(z,t)$ for the jth well. The subscripts Wj and Bj denote the jth well and the jth barrier, respectively, while the subscript SCH combined with T or B designations denotes the top and bottom SCH layers. $N_{Wj}^{3D,2D}(z,t)$ represents the three dimensional and two dimensional carrier densities for the jth well, respectively. The carrier densities in the two SCH regions are all three dimensional. The terms D_{SCH}^{T}, D_{SCH}^{B}, D_{Wj}, and D_{Bj} represent the depths of the top SCH layer, the bottom SCH layers, the jth well, and the jth barriers respectively. The carrier transport time in the top SCH layer is given by τ_d. The carrier capture time and the carrier escape time of the jth well are given by τ_j^C and τ_j^E respectively. These equations assume that the wells and the barriers have the same type of doping as the top SCH layers. If this is not true, the net driving term $[I_{ar}(z,t) - I_l(z,t)]/q\Sigma_{SCH}^{T}L$ should be changed to $[I_{ar}(z,t) - I_l(z,t)]/q\Sigma_{SCH}^{B}L$ and placed on the right side of Equation 36 instead of the right side of Equation 32. The top and bottom SCH layers are assumed to be adjacent to the top and bottom cladding layers respectively, with the well and barriers sandwiched between them. Additionally, all the carrier densities are locally normalized.

The equations above are solved using a damped iteration algorithm in ALDS. The equations are solved at discrete bias points. The parameters generated in the

previous blocks are used as input into the computations. In order to reach optimized computation efficiency, an adaptive step size technique is used during the bias looping procedure in the various iterations. The calculations are concluded when the threshold current for the simulated laser is computed.

Following the completion of the calculations in the threshold analysis block, the final analysis performed using ALDS is the steady state analysis. This block is used to calculate the device static performances as functions of bias current. Using the same techniques described in the threshold analysis block, the performances are calculated over a range of bias currents specified from the user. The light-intensity curves for the laser are the output that is extracted from this block.

5.1.2 Simulation Results

Several different on-wafer and thin-film laser structures were simulated using the ALDS software. The layer structure described in Chapter 4 Figure 38 was input into the software interface for the on-wafer devices. ALDS contained a library of material parameters for common laser materials such as GaAs and AlGaAs. Parameters were extrapolated for the AlGaAs layers as a function of aluminum and gallium composition. Layer doping was also accounted for in this step. For each run performed, the end facet reflectivities and the cavity length were varied. The cavity lengths that were examined are 300, 400, and 500 microns. The Fresnel reflectivity for a GaAs based edge-emitting laser is 32%. Mirror reflectivities upward of 90% can be achieved using coatings on the facets, which can improve the quantum efficiency and thermal characteristics of the laser and lower the threshold current. [84, 85] Due to these considerations, reflectivities of 30,

40, and 50 percent were also examined. A brief overview of the results can be seen in Chart 3.

Table 4 Tabulated simulation results.

Cavity Length (μm)	Reflectivities (%)	Threshold Current (mA)
300	30-30	88.8555
300	40-40	63.6255
300	50-50	49.0855
300	30-40	71.7555
300	30-50	64.3455
300	40-50	55.1155
400	30-30	83.0406
400	40-40	64.7206
400	50-50	53.3206
400	30-40	70.7506
400	30-50	65.2306
400	40-50	58.1206
500	30-30	83.9658
500	40-40	68.8258
500	50-50	58.9758
500	30-40	73.8558
500	30-50	69.2258
500	40-50	63.1458

Figure 46 looks at the effects of varying the facet reflectivities of the lasers. The laser cavity was held at 500 microns and the reflectivity was varied between 30, 40, and 50 percent. The slope efficiencies for each plot are (a) 26.6% (b) 35.7% and 51.6% (c) 31.3% and 63.2% (d) 47.9% (e) 39.1% and 54.7% (f) 44.5%.

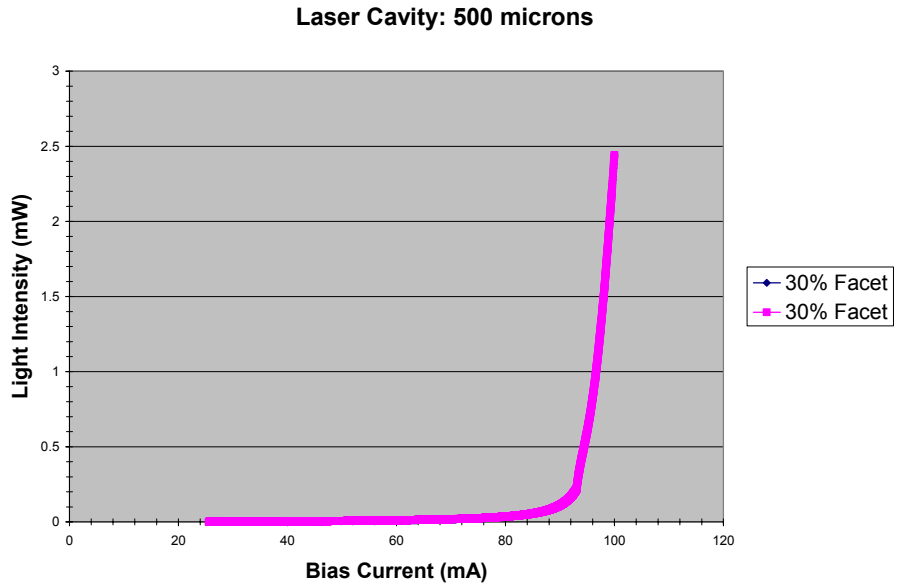
Laser Cavity: 500 microns
Light Intensity (mW)
Bias Current (mA)
30% Facet
30% Facet

(a)

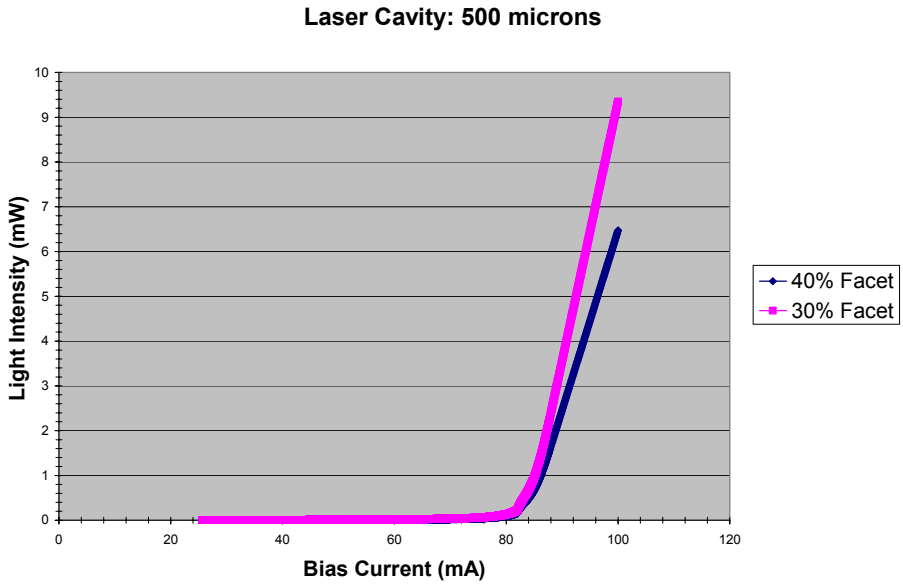
Laser Cavity: 500 microns
Light Intensity (mW)
Bias Current (mA)
40% Facet
30% Facet

(b)

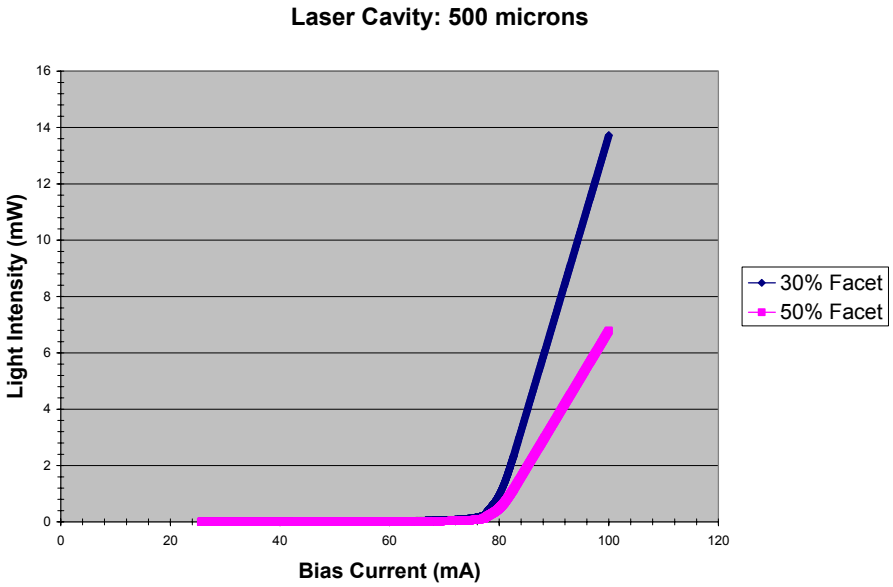
Laser Cavity: 500 microns
Light Intensity (mW)
Bias Current (mA)
0
2
4
6
8
10
12
14
16
0
20
40
60
80
100
120
30% Facet
50% Facet

(c)

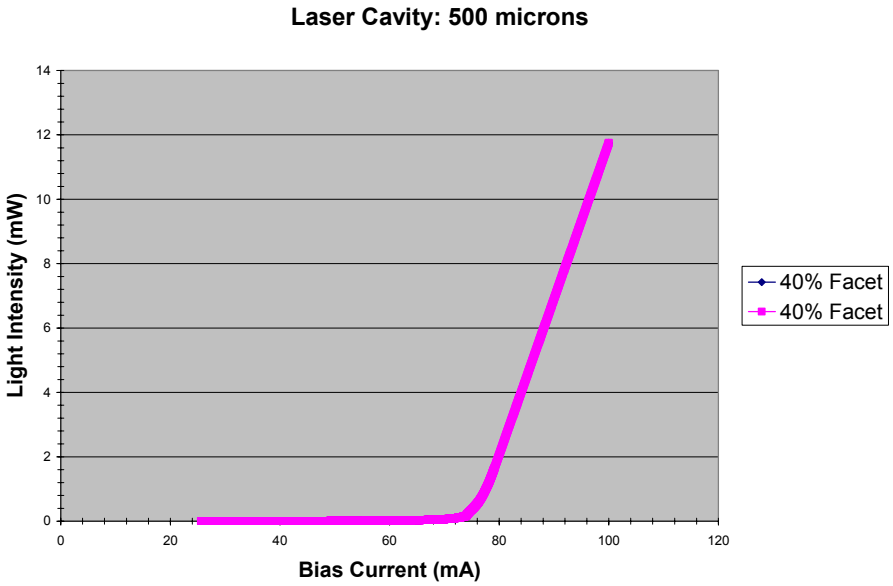
Laser Cavity: 500 microns
Light Intensity (mW)
Bias Current (mA)
0
2
4
6
8
10
12
14
0
20
40
60
80
100
120
40% Facet
40% Facet

(d)

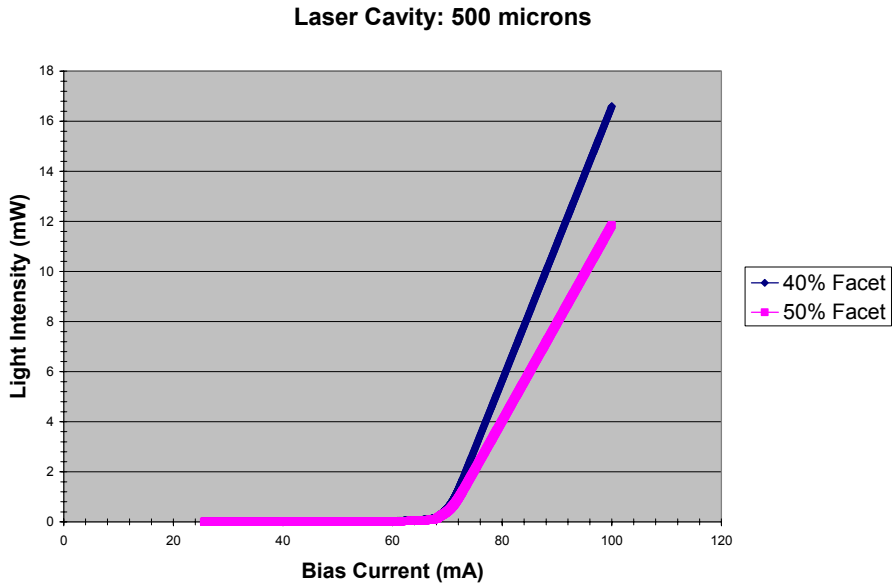

(e)

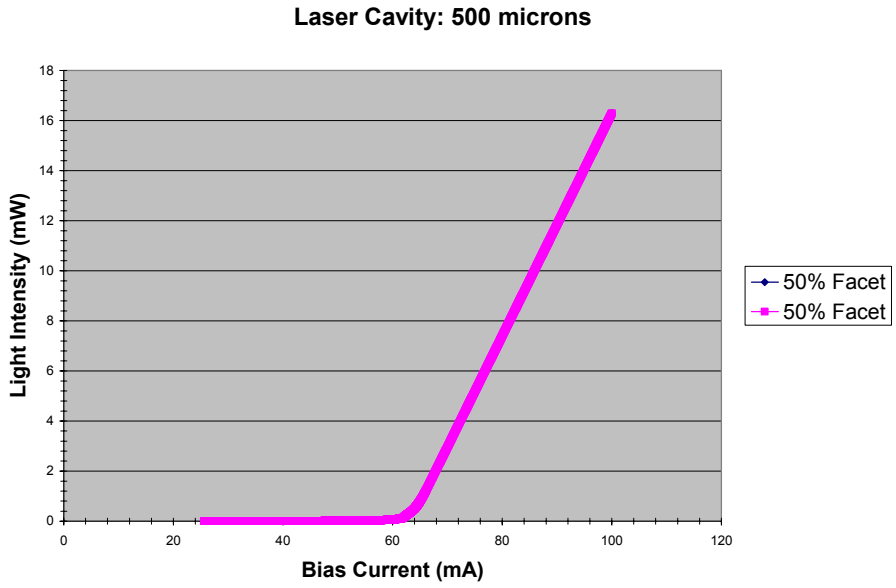

(f)

Figure 46 Simulated LI curves for lasers with a cavity length of 500 µm and varying mirror reflectivities. The reflectivities are as follows (a) 30/30 (b) 30/40 (c) 30/50 (d)40/40 (e) 40/50 (f) 50/50.

The facet reflectivities were held at 30 percent and the cavity length was varied between 300, 400, and 500 microns. The results can be seen in Figure 47. The laser efficiencies fore each plot are (a) .845% (b) 19.5% and (c) 26.6%.

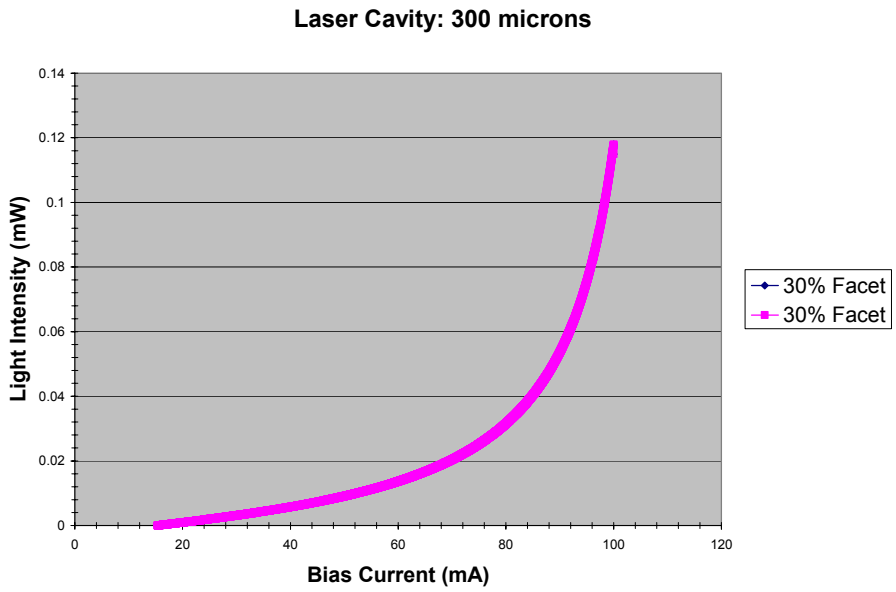

(a)

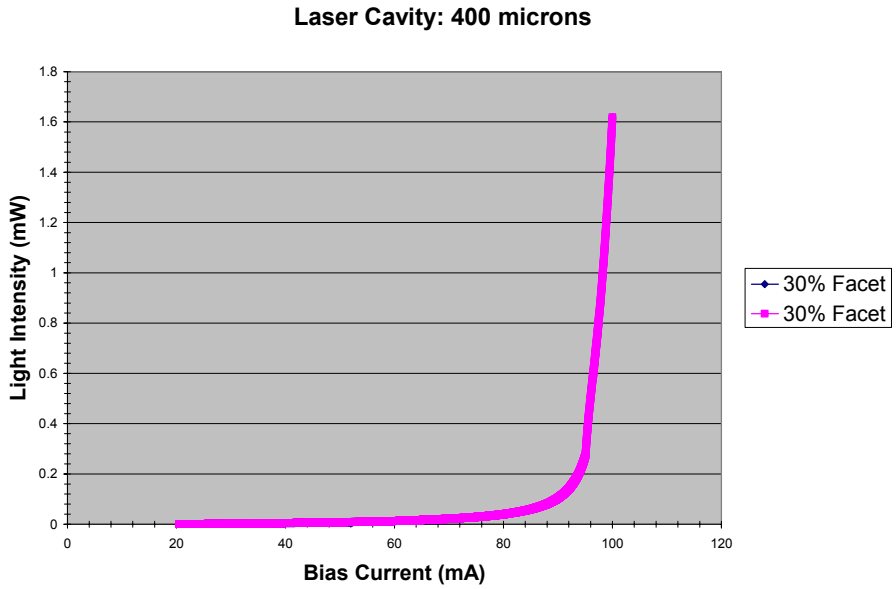

(b)

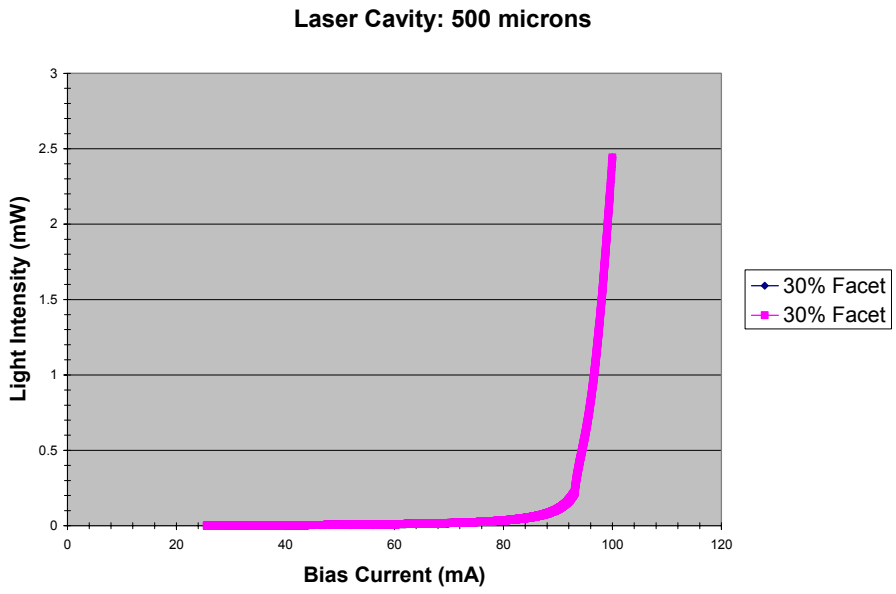

(c)

Figure 47 Simulated LI laser results for laser diodes with 30/30 mirror reflectivities. The cavity length is varied as follows (a) 300 (b) 400 (c) 500.

Upon completion of theses results, ALDS was used to simulate thin-film laser results. These results are summarized in the chart below.

Table 5 Thin-film laser simulation results.

Cavity Length (μm)	Reflectivities (%)	Threshold Current (mA)
300	30-30	133.2080
300	40-40	95.3482
300	50-50	73.5382
300	30-40	111.2580
300	30-50	96.4582
300	40-50	82.5882

5.1.3 Simulation vs. Experimental and Conclusions

The experimental results obtained for on-wafer and thin-film lasers were presented in Chapter 4. While general shape is similar in both the experimental and

theoretical results, there are differences with regard to threshold current and total output power. While some of these differences can be attributed to minor difference in mirror reflectivity, a large degree of the error can be attributed to thermal heating in the device. During the experimental tests for the onwafer lasers, no active cooling methods were applied. The lasers were simply mounted on a copper chuck and tested. The error caused by heat between the thin-film experimental and theoretical results is a bit more pronounced.

Central to the error between the thin-film results is the thermal diffusivity of the thin-film device. Thermal diffusivity is the ratio between the thermal conductivity and the volumetric heat capacity. The thermal conductivity tracks the ability of a material to conduct heat, while the volumetric heat capacity describes the ability of a given volume of a material to store heat while undergoing a given temperature change. Given these definitions, the higher the thermal diffusivity the greater the ability of a material to adjust its temperature toward the temperature of its environment. Several authors have shown that the thermal diffusivity of thin-film materials is often smaller than their bulk counterparts. [76, 78, 86-89] Chen et al. have shown that removing the substrate can decrease the thermal diffusivity by a factor of five to seven. [77] In the thin-film devices, device performance degradation is increased by the same size factor. The performance hit can be seen in the experimental and the theoretical data. Differences between the experimental and theoretical results can also be attributed to the bonding mechanism between the thin-film laser and the silicon substrate. This mechanism creates an insulating interface, which prohibits vertical conduction between the laser and the

substrate. [22] The authors also showed that this insulating interface can be overcome by usually well designed metal contacts.

5.2 Laser-Waveguide Coupling

5.2.1 Simulation methodology

All simulations between the thin-film laser and the interferometric waveguide structures were performed using APSS (Apollo Photonic Solutions Suite). [90] APSS was used to perform two specific functions. First, the modal profiles of the laser structures and the interferometric waveguide structures were generated using the finite-difference method. Using these results, an overlap integral between the laser and the waveguide was performed in order to calculate the coupling between the two under various conditions. This section will outline the theoretical background necessary to perform these calculations.

The modal profiles of each structure are calculated using the finite-difference method. The calculation begins with three sets of equations which can be used to describe a waveguide, full-vector wave equations, semi-vector wave equations, and the scalar Helmholtz equation. These equations can all be derived from the Maxwell equations. The full-vector wave equation in terms of the transverse electrics fields for anisotropic waveguides is given as [90]

$$\begin{pmatrix} P_{xx} & P_{xy} \\ P_{yx} & P_{yy} \end{pmatrix} \begin{pmatrix} E_x \\ E_y \end{pmatrix} = \beta^2 \begin{pmatrix} E_x \\ E_y \end{pmatrix} \qquad [37]$$

where the operators are given by [90]

$$P_{xx}E_x = n_{xx}^2 k^2 E_x + \frac{\partial}{\partial x}\left[\frac{1}{n_{xx}^2}\frac{\partial}{\partial x}\left(n_{xx}^2 E_x\right)\right] + \frac{\partial^2 E_x}{\partial y^2} \qquad [38]$$

$$P_{yy}E_y = n_{yy}^2 k^2 E_y + \frac{\partial}{\partial y}\left[\frac{1}{n_{yy}^2}\frac{\partial}{\partial y}\left(n_{yy}^2 E_y\right)\right] + \frac{\partial^2 E_y}{\partial x^2} \quad [39]$$

$$P_{xy}E_y = n_{xy}^2 k^2 E_y + \frac{\partial}{\partial x}\left[\frac{1}{n_{zz}^2}\frac{\partial}{\partial y}\left(n_{yy}^2 E_y\right)\right] + \frac{\partial^2 E_y}{\partial x \partial y} \quad [40]$$

$$P_{yx}E_x = n_{yx}^2 k^2 E_x + \frac{\partial}{\partial y}\left[\frac{1}{n_{zz}^2}\frac{\partial}{\partial x}\left(n_{xx}^2 E_x\right)\right] + \frac{\partial^2 E_x}{\partial x \partial y} \quad [41]$$

The full-vector wave equation in terms of the transverse magnetic fields can also be derived. It is given as [90]

$$\begin{pmatrix} Q_{xx} & Q_{xy} \\ Q_{yx} & Q_{yy} \end{pmatrix}\begin{pmatrix} H_x \\ H_y \end{pmatrix} = \beta^2 \begin{pmatrix} H_x \\ H_y \end{pmatrix} \quad [42]$$

where the operators are defined as [90]

$$Q_{xx}H_x = n_{yy}^2 k^2 H_x + \frac{\partial^2 H_x}{\partial x^2} + n_{yy}^2 \frac{\partial}{\partial y}\left[\frac{1}{n_{zz}^2}\frac{\partial H_x}{\partial x}\right] \quad [43]$$

$$Q_{yy}H_y = n_{xx}^2 k^2 H_y + \frac{\partial^2 H_y}{\partial y^2} + n_{xx}^2 \frac{\partial}{\partial x}\left[\frac{1}{n_{zz}^2}\frac{\partial H_y}{\partial y}\right] \quad [44]$$

$$Q_{xy}H_y = n_{yx}^2 k^2 H_y + \frac{\partial^2 H_y}{\partial x \partial y} + n_{yy}^2 \frac{\partial}{\partial y}\left[\frac{1}{n_{zz}^2}\frac{\partial H_y}{\partial x}\right] \quad [45]$$

$$Q_{yx}H_x = n_{xy}^2 k^2 H_x + \frac{\partial^2 H_x}{\partial x \partial y} + n_{xx}^2 \frac{\partial}{\partial x}\left[\frac{1}{n_{zz}^2}\frac{\partial H_x}{\partial y}\right] \quad [46]$$

The full-vector wave equation is a complete description of all conditions of the waveguide. It considers polarization dependence ($P_{xx} \neq P_{yy}$ and $Q_{xx} \neq Q_{yy}$) and the polarization coupling ($P_{xy} \neq 0$, $P_{yx} \neq 0$, $Q_{xy} \neq 0$, and $Q_{yx} \neq 0$). Both the polarization dependence and the polarization coupling are dependent on waveguide geometry and

material composition. These polarization dependence and coupling become only dependent on waveguide geometry if the waveguide is isotropic ($n_{xx}^2 = n_{yy}^2 = n_{zz}^2 = n^2$ and $n_{xy}^2 = n_{yx}^2 = 0$).

The semi-vector wave equations and the Scalar Helmholtz equation are special cases of the full-vector wave equations. [90] For the semi-vector wave equations, the polarization coupling of the waveguide is weak and can be neglected. This condition exists in many practical optical waveguides. In this condition, the full-vector wave equations can be reduce to two decoupled equations for the electric fields given as [90]

$$P_{xx}E_x = \beta_x^2 E_x \quad [47]$$

$$P_{yy}E_y = \beta_y^2 E_y \quad [48]$$

The magnetic field version of the equations is given by [90]

$$Q_{xx}H_x = \beta_x^2 H_x \quad [49]$$

$$Q_{yy}H_y = \beta_y^2 H_y \quad [50]$$

For the scalar Helmholtz equations, the guide is assumed to be so weakly guided that polarization dependence can be ignored. In this scenario the two semi-vector equations reduce to a single scalar wave equation given by [90]

$$PE = \beta^2 E \quad [51]$$

where the scalar operative is given by [90]

$$P = n^2 k^2 E + \frac{\partial^2 E}{\partial y^2} + \frac{\partial^2 E}{\partial x^2} \quad [52]$$

During the finite-difference method, all of the equations defined above undergo discretization. The results is a system of linear equations in the form [90]

$$AE = \beta^2 E \qquad [53]$$

where A is a sparse matrix. The power method is used to solve for the eigen-values and eigenvectors of the sparse matrix. These solutions correspond to the propagation constants and the modal field profiles of the calculated modes. These results can be used to generate a modal field pattern which can then be passed on to the overlap integral calculation.

5.2.2 Simulation Results

The overlap integral calculates the total power that couples from one waveguide mode to another waveguide mode. In order to simplify the calculation, only the first order mode was considered for this simulation. This assumption was made due to the majority of the laser power being contained in the fundamental mode. A thin-film laser with a 10 µm stripe was simulated and the calculated mode was launched into a silicon oxynitride/silicon dioxide waveguide. Three different core thicknesses were simulated; 0.25 µm, 0.35 µm, and 0.50 µm. These core diameters were chosen because evanescent coupling will still be viable at these diameters. Waveguides larger than these will to

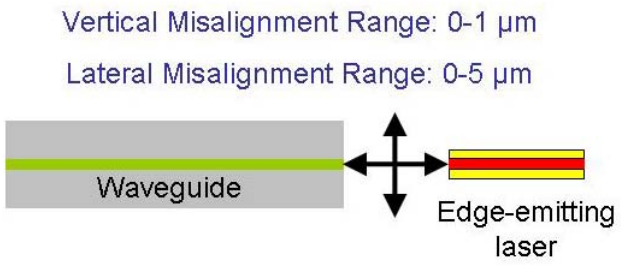

Figure 48 Schematic of simulated waveguide and laser coupling.

tightly confine the light to the core and the sensitivity of a sensor of this design would drop dramatically as there would be little interaction between the light and the sense layer due to a small evanescent tail. At these dimensions, the waveguide would be single-mode in the vertical and multimode in the horizontal. The silicon oxynitride core had a refractive index of 1.922, while the silicon dioxide cladding had a refractive index of 1.465. The simulation also examined the effects of vertical misalignment between the laser and the waveguide. Due to fabrication variations, a range of 0-1 μm vertical misalignment was simulated. Finally, the simulation was also used to examine the effect of waveguide separation from the laser. Gaps of 0, 1, 2, and 5 microns were used in the simulation. The experimental schematic can be seen in Figure 48.

A quick summary of the lateral misalignment results can be seen in Table 5. This data shows that very little misalignment can be tolerated in the integrated system. Under ideal conditions, the maximum coupling between the waveguide and the laser is 22.375%. This value falls off rapidly as the lateral misalignment is increased. With a 1 μm gap between the laser and the waveguide, coupling is reduced by half for all of the various waveguide core diameters. By time the misalignment is increased to 5 microns, the coupling decreases to approximately 4% for all core diameters. Differences in modal profile between the waveguide and the laser are largely responsible for this small coupling efficiency.

Table 6 Summary of coupling results obtained when simulating lateral misalignment between the laser and the waveguide.

Waveguide Core Diameter (μm)	Lateral Misalignment (μm)	Coupling
0.25	0	0.22375

Table 6 Continued

0.25	1	0.1198
0.25	2	0.07876
0.25	5	0.03988
0.35	0	0.21129
0.35	1	0.11728
0.35	2	0.07748
0.35	5	0.03911
0.5	0	0.21422
0.5	1	0.11645
0.5	2	0.07688
0.5	5	0.03883

A more detailed looked at these simulation results shows how sensitive this implementation is to vertical misalignment. Figure 49 demonstrates graphically the alignment tolerance of the system at various gaps between the waveguide and the laser. The reason that the peak of the coupling efficiency does not occur at 0 μm of vertical misalignment is due to the structure definition in the software. The lower left edge of the core is set to (0,0) for all of the structures, so the actual perfect alignment of the waveguide and the laser structure is at slightly different nonzero values depending on waveguide core thickness. It is apparent that from these plots that there is an exponential drop off which occurs rapidly with slight misalignments. For the 0 μm gap sample, the 3 dB drop-off occurs with 0.25 μm vertical misalignment. There is a slight improvement of

the 3 dB coupling data point at larger gap distances, but this comes at the expense of coupling efficiency.

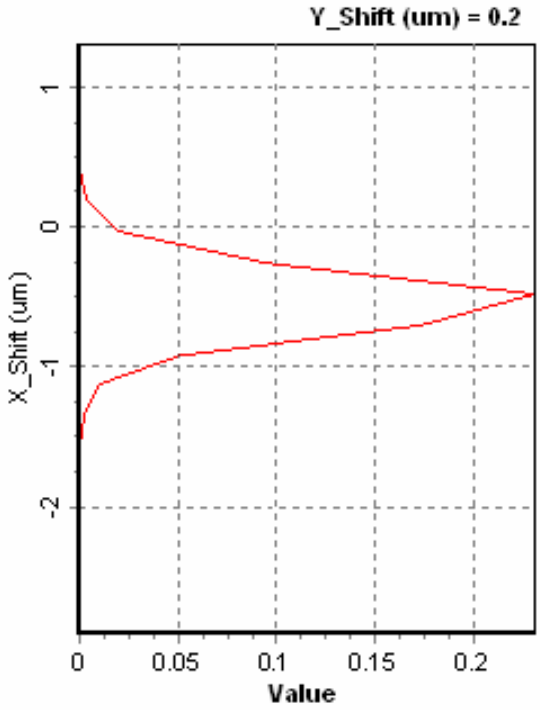

(a)

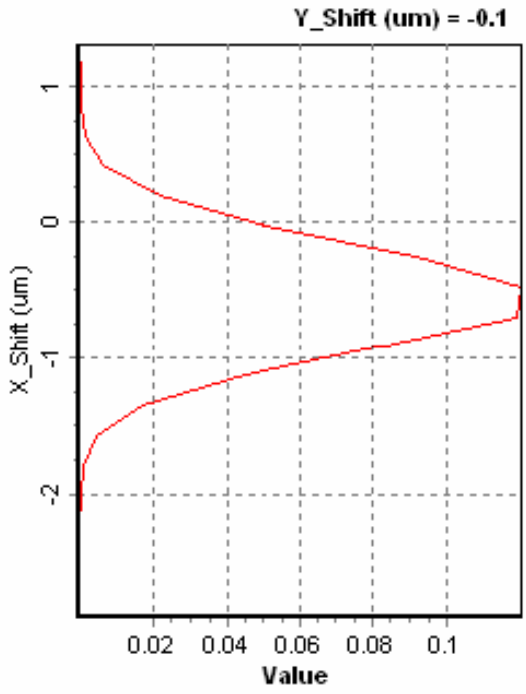

(b)

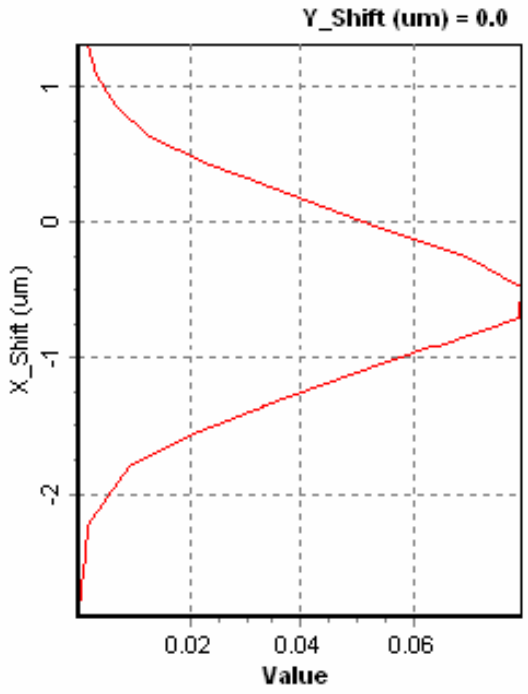

(c)

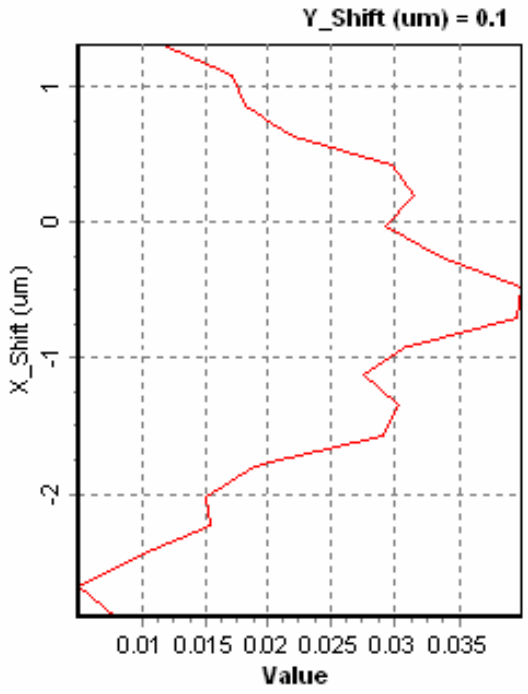

(d)

Figure 49 Simulation results showing the impact of vertical misalignment and different gap thicknesses. (a) 0 µm (b) 1 µm (c) 3 µm (d) 5 µm.

5.2.3 Conclusions

As evidenced from the results detailed above, the entire sensor system is highly sensitive to vertical or lateral misalignment between the laser and the waveguide. Even perfectly aligned, the system only can reach 22% coupling efficiency as currently designed. As lateral alignment is increased, the system rapidly falls off, reaching 4% at a lateral separation of 5 μm. These coupling values are largely due to modal mismatch between the laser active region and the waveguide core. Vertical misalignment show the same sort of sensitivity as coupling efficiency drops rapidly with increasing misalignment. All simulations show a 3 dB drop-off of coupling efficiency in less than 1 μm of vertical misalignment. These results indicate that a system designed in this manner would be high difficult to build and would require very stringent processing controls as the tolerances are extremely tight.

5.3 Summary and Discussions

A theoretical analysis of the optically embedded sensor is presented is presented in this chapter. The first detail examines the thin-film lasers fabricated in Chapter 4. The ALDS software package is presented and the analysis techniques used by the software are examined. Various lasers designs were simulated and compared to the fabricated devices. While the shape of the theoretical curves was similar to the fabricated results, the software was unable to account for the thermal impact in the laser testing. This was particularly evident in the thin-film laser simulations. The software was unable to properly account for the lack of heat transfer due to the substrate removal. The second section looked at the coupling between the thin-film laser and the waveguide interferometer. APSS was used to simulate the coupling in between these two

components. The simulation methodology of APSS was presented and the coupling efficiency between the laser and the waveguide was calculated. A maximum coupling efficiency of approximately 22% was calculated for ideal conditions. This efficiency decreased to 4% with an air gap of 5 μm between the waveguide and the laser. Lateral alignment also proved critical as a 3 dB drop could be seen with less than 1 μm misalignment for all scenarios.

Chapter 6

Conclusions and Recommendations

The design and fabrication of thin-film edge emitting lasers and chemical/biological sensors are contributions to the field of embedded optical sensors and systems. This dissertation details the first heterogeneously integrated chemical/biological CMOS sensor system. To achieve that goal, thin-film edge emitting GaAs lasers were developed. A dielectric waveguide sensor scheme was also developed and demonstrated. The first section of this chapter details the significant results reported in this thesis. The second section details the future research directions of this work.

6.1 Summary of the Results

6.1.1 Design and Fabrication of Optically Embedded Interferometric Sensors

In this dissertation, a fabrication plan for an integrated sensor system was described and demonstrated. The major components of the system were a thin-film edge emitting laser, a Mach-Zehnder interferometric waveguide sensor, and CMOS circuitry. A fabrication plan for the thin-film lasers based on the wedge-induced facet cleaving method was outlined. On-wafer lasers were first produced to demonstrate the performance of the laser material. These lasers showed a threshold of 60 mA and an output power of 3 mW with a 10 μm strip contact. All results were obtained under pulsed conditions. The thin-film laser results were not particularly good. Extreme heat degradation caused the laser to perform very poorly.

A detailed fabrication process for the interferometric waveguide sensor was also detailed in this dissertation. The sensor was first fabricated on silicon wafers to

demonstrate sensor operation. Clear modal changes were observed when various chemicals were introduced into the completed sensor structure.

6.1.2 Theoretical Analysis of Optically Embedded Interferometric Sensor Technology

A theoretical analysis of the thin-film edge emitting lasers and the coupling between the laser and the waveguide sensor was presented. Laser of varying cavity length and mirror reflectivity were simulated. Results of these simulations were tabulated and presented. It was shown that while the shape of the actual curves, matched their theoretical counterpart, the threshold current and the laser power did not. This was shown to be due to device overheating in the case of on-wafer lasers and thermal diffusivity in the case of thin-film laser.

6.2 Future Research

Throughout the pursuit of this research, several areas have been identified which require future research to improve upon the design and functionality of the sensors described within this thesis. The work presented in this thesis details a first effort to realize sensors of this design. Optimization of the components of the system would be necessary in any future designs. The following paragraphs will describe several areas that should be explored when forwarding this work.

One of the major stumbling blocks of this work was the inability to couple successfully from the sensor interferometers to the underlying CMOS detectors. The main mechanism of coupling used was evanescent coupling. This coupling mechanism was chosen due to its simplicity and fabrication ease. More efficient coupling mechanisms can be fabricated at the cost of increased overall system complexity. For future endeavors, it would be prudent to use grating couplers to achieve this goal.

Several research groups have reported grating couplers used in this manner. [91-96] High coupling efficiencies have been reported with these structures and these efficiency levels will allow for a smaller power budget for the overall system. The main difficulty with this approach is how to integrate it into the current design. Patterning could be achieved through ebeam lithography, but a compatible material system would have to be chosen for the gratings.

Another coupling difficulty arose between the laser and the waveguide sensors. Simulations showed that significant mode mismatch existed between the laser and the waveguide facets. Similar with the detector coupling, this problem could be solved with grating couplers. It may also be beneficial to examine adiabatic waveguide tapers. These taper have been used extensively to convert the mode of one waveguide to match the mode shape and size of another waveguide. The majority of this work has been focused on coupling between semiconductor waveguides and single mode fiber, though there has been a small amount of work done involving dielectric waveguides. [97-102] A careful analysis of the mode profile of the laser would have to be performed. After this is completed, an adiabatic taper could be designed which would accept the mode profile of thee laser. Almost all the research done in this area involves monolithic approaches performed in semiconductor systems. This technology would have to be adapted to a heterogeneous dielectric implementation. Once adapted, it is possible that high coupling could be achieved between the lasers and the waveguide sensors. Another major hurdle of this approach is that the adiabatic taper usually requires a great deal of space. The taper has to occur over a great distance to minimize the loss that occurs during the mode conversion. Since this work involves minimizing the sensor onto a single CMOS circuit,

topology constraints must be strictly adhered to. Space concerns would have to be alleviated before the tapers could be integrated into the system.

The temperature dependence of the lasers fabricated for this work will also require further study. As indicated above, van der Waals bonding acts as a block for efficient heat transfer between the thin-film device and the sensor substrate. As a result of this lack of heat transfer, the increased heat of the laser decreases the output power of the laser and increases its threshold current. Two different solutions merit investigation. The first involves investigating and integrated thermal cooler for the thin-film laser. Coolers of this nature have been examined thoroughly in the literature. [103-107] The main challenge would be how to adapt this technology to thin-film devices. The lack of a substrate make those devices particularly fragile, thus handling after fabrication is very difficult. Any cooler would have to be integrated into the process so that the handling of the thin-film device is minimized. The second solution involves using on wafer laser instead of thin-film devices. The presence of the device substrate would lessen the need for device cooling though it still may be required. This solution would add difficulty with integration of the system and would have to be carefully considered. Regardless, a more rigorous cooling solution would have to be implanted in any future sensor system of this design.

The optical source chose for this work was a thin-film edge emitting laser. The original Hartman sensor used a packaged VCSEL. It might be advantageous to explore integrating a thin-film VCSEL into the sensor system. The low power consumption of the VCSEL would lead to a device which generates less heat, so cooling, while still a concern, would not be as sever a problem as it is with the edge emitting device. A

VCSEL would also integrate very well with a grating coupler, eliminating the need for an adiabatic taper on the waveguide. The added complexity of the VCSEL structure would add some fabrication difficulties, but consideration of the VCSEL source could prove worth the time.

References

[1] E. O'Reilly, *Quantum Theory of Solids*, 1st ed. New York: Taylor & Francis, 2002.

[2] G. P. Agrawal and N. K. Dutta, *Semiconductor Lasers*, 2nd ed. New York: Van Nostrand Reinhold, 1993.

[3] R. Schatz and C. G. Bethea, "Steady state model for facet heating leading to thermal runaway in semiconductor lasers," *Journal of Applied Physics*, vol. 76, pp. 2509, 1994.

[4] J. S. Yoo, S. Fang, and H. H. Lee, "Condition for no thermal runaway in CW semiconductor lasers," *Journal of Applied Physics*, vol. 74, pp. 6503, 1993.

[5] W. Both, G. Erbert, A. Klehr, R. Rimpler, G. Stadermann, and U. Zeimer, "Catastrophic optical damage in GaAlAs/GaAs laser diodes," *IEE Proceedings J (Optoelectronics)*, vol. 134, pp. 95, 1987.

[6] B. L. Meadows, F. Amzajerdian, B. W. Barnes, N. R. Baker, R. P. Baggott, U. N. Singh, and M. J. Kavaya, "Reliability of long pulsewidth high power laser diode arrays," presented at Advanced Devices and Materials for Laser Remote Sensing. Symposium, San Francisco, CA, USA, 2005.

[7] B. L. Meadows, F. Amzajerdian, N. R. Baker, V. Sudesh, U. N. Singh, and M. J. Kavaya, "Thermal characteristics of high-power long-pulsewidth quasi-CW laser diode arrays," *Proc. SPIE - Int. Soc. Opt. Eng.*, vol. 5336, pp. 203, 2004.

[8] J. J. Huddle, L. C. Chow, S. Lei, A. Marcos, D. P. Rini, S. J. Lindauer, II, M. Bass, and P. J. Delfyett, "Thermal management of diode laser arrays," presented at Sixteenth Annual IEEE Semiconductor Thermal Measurement and Management Symposium, San Jose, CA, USA, 2000.

[9] K. Aiki, M. Nakamura, T. Kuroda, and J. Umeda, "Channeled-substrate planar structure (Al,Ga)As injection lasers," *Applied Physics Letters*, vol. 30, pp. 649, 1977.

[10] H. Kawaguchi and T. Kawakami, "Transverse-mode control in an injection laser by a strip-loaded waveguide," *IEEE Journal of Quantum Electronics*, vol. QE-13, pp. 556, 1977.

[11] T. P. Lee, C. A. Burrus, B. I. Miller, and R. A. Logan, "Al_xGa_{1-x}As double heterostructure rib-waveguide injection laser," *IEEE Journal of Quantum Electronics*, vol. QE-11, pp. 432, 1975.

[12] R. Dingle, W. Wiegmann, and C. H. Henry, "Quantum states of confined carriers in very thin Al_xGa_{1-x}As-GaAs-Al_xGa_{1-x}As heterostructures," *Physical Review Letters*, vol. 33, pp. 827, 1974.

[13] N. Holonyak, Jr., R. M. Kolbas, R. D. Dupuis, and P. D. Dapkus, "Quantum well heterostructure lasers," *IEEE Journal of Quantum Electronics*, vol. QE-16, pp. 170, 1980.

[14] A. Yariv, "Quantum well semiconductor lasers are taking over," *IEEE Circuits and Devices Magazine*, vol. 5, pp. 25, 1989.

[15] Y. Arakawa and A. Yariv, "Quantum well lasers-gain, spectra, dynamics," *IEEE Journal of Quantum Electronics*, vol. QE-22, pp. 1887, 1986.

[16] Y. Arakawa and A. Yariv, "Theory of gain, modulation response, and spectral linewidth in AlGaAs quantum well lasers," *IEEE Journal of Quantum Electronics*, vol. QE-21, pp. 1666, 1985.

[17] T. Ohtoshi, K. Uomi, N. Chinone, T. Kajimura, and Y. Murayama, "Calculated gain and spontaneous spectra of multi-quantum-well lasers," *Journal of Applied Physics*, vol. 57, pp. 992, 1985.

[18] D. Kasemset, C. S. Hong, N. B. Patel, and P. D. Dapkus, "Graded barrier single quantum well lasers-theory and experiment," Ottawa, Ont., Canada, 1983.

[19] G. Lasher and F. Stern, "Spontaneous and stimulated recombination radiation in semiconductors," *Physical Review*, vol. 133, pp. A553-A563, 1964.

[20] N. K. Dutta, "Calculated threshold current of GaAs quantum well lasers," *Journal of Applied Physics*, vol. 53, pp. 7211, 1982.

[21] S. L. Chuang, *Physics of Optoelectronic Devices*, 1st ed. New York: John Wiley & Sons, Inc., 1995.

[22] J. C. Fan, K. Y. Chen, G. Lin, and C. P. Lee, "Stripe-geometry GaAs-InGaAs laser diode with back-side contact on silicon by epitaxial lift-off," *Electronics Letters*, vol. 33, pp. 1095-1096, 1997.

[23] I. Pollentier, L. Buydens, P. Van Daele, and P. Demeester, "Fabrication of a GaAs-AlGaAs GRIN-SCH SQW laser diode on silicon by epitaxial lift-off," *IEEE Photonics Technology Letters*, vol. 3, pp. 115-117, 1991.

[24] C. L. Shieh, J. Y. Chi, C. A. Armiento, P. O. Haugsjaa, A. Negri, and W. I. Wang, "1.3 mu m InGaAsP ridge waveguide laser on GaAs and silicon substrates by thin film transfer," *Electronics Letters*, vol. 27, pp. 850-851, 1991.

[25] E. Yablonovitch, E. Kapon, T. J. Gmitter, C. P. Yun, and R. Bhat, "Double heterostructure GaAs/AlGaAs thin film diode lasers on glass substrates," *IEEE Photonics Technology Letters*, vol. 1, pp. 41-42, 1989.

[26] M. Yanagisawa, H. Terui, K. Shuto, T. Miya, and M. Kobayashi, "Film-level hybrid integration of AlGaAs laser diode with glass waveguide on Si substrate," *IEEE Photonics Technology Letters*, vol. 4, pp. 21-23, 1992.

[27] A. Ackaert, L. Buydens, D. Lootens, P. Van Daele, and P. Demeester, "Crack formation and thermal stress relaxation of GaAs on Si growth by metalorganic vapor phase epitaxy," *Applied Physics Letters*, vol. 55, pp. 2187, 1989.

[28] F. L. Pedrotti and L. S. Predrotti, *Introduction to Optics*, 2nd ed. Englewood Cliffs: Prentice Hall, 1993.

[29] C. R. Pollock, *Fundamentals of Optoelectronics*. Chicago: Richard D. Irwin, Inc., 1995.

[30] A. Yariv, *Optical Electronics in Modern Communications*, 5th ed. New York: Oxford University Press, 1997.

[31] F. T. S. Yu and X. Yang, *Introduction to Optical Engineering*. New York: Cambridge University Press, 1997.

[32] N. F. Hartman, J. C. Wyvill, D. Campbell, and P. Edmonds, "Rapid response biosensor for detection and identification of common foodborne pathogens," *Proceedings of the SPIE*, vol. 2345, pp. 128-137, 1995.

[33] T. V. Clapp, L. W. Cahill, and W. A. Crossland, "Waveguide strategies for optical interconnect on CMOS," presented at 15th Annual Meeting of the IEEE Lasers and Electro-Optics Society, Glasgow, UK, 2002.

[34] J. W. Goodman, F. J. Leonberger, S.-Y. Kung, and R. A. Athale, "Optical Interconnections for VLSI Systems," *Proceedings of the IEEE*, vol. 72, pp. 850-866, 1984.

[35] Y. Liu, L. Lin, C. Choi, B. Bihari, and R. T. Chen, "Optoelectronic integration of polymer waveguide array and metal-semiconductor-metal photodetector through micromirror couplers," *IEEE Photonics Technology Letters*, vol. 13, pp. 355, 2001.

[36] F. Gouin, L. Robitaille, C. L. Callender, J. Noad, and C. Almeida, "A 4*4 optoelectronic switch matrix integrating an MSM array with polyimide optical waveguides," *Proceedings of the SPIE*, vol. 3290, pp. 287-295, 1997.

[37] L. Robitaille, C. L. Callender, J. P. Noad, F. Gouin, and C. A. Almeida, "Integration of optoelectronic switch matrices using metal-semiconductor-metal

protectors and polyimide waveguide circuitry," *Optical Engineering*, vol. 37, pp. 1157-1163, 1998.

[38] R. Muller, P. Obreja, V. Banu, I. Pavelescu, and D. Dascalu, "Silicon-compatible waveguides used for an integrated opto-mechanical pressure sensor," *Optical Materials*, vol. 17, pp. 255-258, 2001.

[39] U. Hilleringmann and K. Goser, "Optoelectronic system integration on silicon: waveguides, photodetectors, and VLSI CMOS circuits on one chip," *IEEE Transactions on Electron Devices*, vol. 42, pp. 841-846, 1995.

[40] R. T. Chen, L. Wu, L. Lin, C. Choi, Y. Liu, B. Bihari, S. Tang, R. Wickman, B. Picor, and Y. S. Liu, "Guided-wave Si CMOS process-compatible optical interconnects," presented at 1999 International Semiconductor Conference, Sinaia, Romania, 1999.

[41] S.-Y. Cho, M. Thomas, D.-I. Kim, N. M. Jokerst, and M. Brooke, "Polymer waveguide optical interconnections on Si CMOS circuits," presented at Conference on Lasers and Electro-Optics 2002, Long Beach, CA, USA, 2002.

[42] R. T. Chen, L. Lei, C. Chulchae, Y. J. Liu, B. Bihari, L. Wu, S. Tang, R. Wickman, B. Picor, M. K. Hibb-Brenner, J. Bristow, and Y. S. Liu, "Fully embedded board-level guided-wave optoelectronic interconnects," *Proceedings of the IEEE*, vol. 88, pp. 780-793, 2000.

[43] T. Sakamoto, H. Tsuda, M. Hikita, T. Kagawa, K. Tateno, and C. Amano, "Optical interconnection using VCSELs and polymeric waveguide circuits," *Journal of Lightwave Technology*, vol. 18, pp. 1487-1492, 2000.

[44] F. Mederer, R. Jager, H. J. Unold, R. Michalzik, K. J. Ebeling, S. Lehmacher, A. Neyer, and E. Griese, "3-Gb/s data transmission with GaAs VCSELs over PCB integrated polymer waveguides," *IEEE Photonics Technology Letters*, vol. 13, pp. 1032-1034, 2001.

[45] S.-Y. Cho, S.-W. Seo, M. A. Brooke, and N. M. Jokerst, "Integrated detectors for embedded optical interconnections on electrical boards, modules, and integrated circuits," *IEEE Journal of Selected Topics in Quantum Electronics*, vol. 8, pp. 1427-1434, 2002.

[46] H. Ribot, P. Sansonetti, and A. Carenco, "Improved design for the monolithic integration of a laser and an optical waveguide coupled by an evanescent field," *IEEE Journal of Quantum Electronics*, vol. 26, pp. 1930-1941, 1990.

[47] H.-F. Kuo, S.-Y. Cho, J. Hall, and N. M. Jokerst, "InP/InGaAsP MQW thin film edge emitting lasers for embedded waveguide chip to chip optical interconnections," Tucson, AZ, USA, 2003.

[48] H.-F. Kuo, S.-Y. Cho, and N. M. Jokerst, "Heterogeneous integration of InP/InGaAsP MQW thin film edge emitting lasers and polymer waveguides," Las Vegas, NV, USA, 2004.

[49] S.-W. Seo, S.-y. Cho, H.-F. Kuo, T. Ogawa, and N. M. Jokerst, "Optical interconnection using embedded thin film edge emitting lasers, photodetectors, and polymer waveguides," San Diego, CA, USA, 2004.

[50] S. Kollakowski, E. Droge, E. H. Bottcher, A. Strittmatter, O. Reimann, and D. Bimberg, "Waveguide-integrated InP/InGaAs/InAlGaAs MSM photodetector for operation at 1.3 and 1.55 mu m," presented at 1998 International Conference on Indium Phosphide and Related Materials, Tsukuba, Japan, 1998.

[51] O. Vendier, N. M. Jokerst, and R. P. Leavitt, "Thin-film inverted MSM photodetectors," *IEEE Photonics Technology Letters*, vol. 8, pp. 266-268, 1996.

[52] S.-Y. Cho, M. A. Brooke, and N. M. Jokerst, "Optical interconnections on electrical boards using embedded active optoelectronic components," *IEEE Journal of Selected Topics in Quantum Electronics*, vol. 9, pp. 465, 2003.

[53] S.-Y. Cho, S.-W. Seo, N. M. Jokerst, and M. Brooke, "Comparative high speed optical interconnections using thin film photodetectors embedded in polymer waveguides," presented at 2005 Proceedings. 55th Electronic Components and Technology, Lake Buena Vista, FL, USA, 2005.

[54] S.-Y. Cho, S.-W. Seo, N. M. Jokerst, and M. A. Brooke, "High-speed optical interconnection using thin film PDs embedded in polymer waveguides on electrical boards," *Proceedings of the SPIE - The International Society for Optical Engineering*, vol. 5353, pp. 57, 2004.

[55] S.-W. Seo, S.-Y. Cho, and N. M. Jokerst, "A thin-film laser, polymer waveguide, and thin-film photodetector cointegrated onto a silicon substrate," *IEEE Photonics Technology Letters*, vol. 17, pp. 2197, 2005.

[56] H. Helmers, P. Greco, R. Rustad, R. Kherrat, G. Bouvier, and P. Benech, "Performance of a compact, hybrid optical evanescent-wave sensor for chemical and biological applications," *Applied Optics*, vol. 35, pp. 676-680, 1996.

[57] B. J. Luff, J. S. Wilkinson, J. Piehler, U. Hollenbach, J. Ingenhoff, and N. Fabricius, "Integrated optical Mach-Zehnder biosensor," *Journal of Lightwave Technology*, vol. 16, pp. 583-592, 1998.

[58] W. Lukosz, "Integrated optical chemical and direct biochemical sensors," *Sensors and Actuators B*, vol. B29, pp. 37-50, 1995.

[59] Q. Zhi-Mei, N. Matsuda, K. Itoh, M. Murabayashi, and C. R. Lavers, "A design for improving the sensitivity of a Mach-Zehnder interferometer to chemical and biological measurands," *Sensors and Actuators B*, vol. B81, pp. 254-258, 2002.

[60] D. P. Campbell, D. S. Gottfried, and J. M. Cobb-Sullivan, "Groundwater monitoring of VOCs with an interferometric optical waveguide sensor," *Proceedings of the SPIE - The International Society for Optical Engineering*, vol. 5586, pp. 136, 2004.

[61] C. Manning, M. Gross, T. Hanshaw, R. L. Kirlin, and A. Samuels, "Compact interferometers for chemical and biological agent detection," *Proceedings of the SPIE - The International Society for Optical Engineering*, vol. 5268, pp. 125, 2003.

[62] N. F. Hartman, J. Cobb, J. G. Edwards, X. Yang, P. Katila, M. J. Leppihalme, A. Tervonen, and N. Peyghambarian, "Optical system-on-a-chip for chemical and biochemical sensing: the platform," *Proceedings of the SPIE*, vol. 3537, pp. 302-309, 1999.

[63] D. P. Campbell, N. F. Hartman, J. L. Moore, J. V. Suggs, and J. M. Cobb, "Reversible integrated optic evanescent field biosensor using chemical amplification for added sensitivity," *Proceedings of the SPIE*, vol. 3253, pp. 20-26, 1998.

[64] D. P. Campbell, J. L. Moore, J. M. Cobb, N. F. Hartman, B. H. Schneider, and M. G. Venugopal, "Optical system-on-a-chip for chemical and biochemical sensing: the chemistry," *Proceedings of the SPIE*, vol. 3540, pp. 153-161, 1999.

[65] A. A. Boiarski, R. W. Ridgway, J. R. Busch, G. Turhan-Sayan, and L. S. Miller, "Integrated optic biosensor for environmental monitoring," *Proceedings of the SPIE*, vol. 1587, pp. 114-128, 1992.

[66] N. Fabricius, G. Gauglitz, and J. Ingenhoff, "A gas sensor based on an integrated optical Mach-Zehnder interferometer," *Sensors and Actuators B*, vol. B7, pp. 672-676, 1992.

[67] J. Ingenhoff, B. Drapp, and G. Gaulitz, "Biosensors using integrated optical devices," *Journal of Analytical Chemistry*, vol. 346, pp. 580-583, 1993.

[68] Y. Liu, P. Hering, and M. O. Scully, "An integrated optical sensor for measuring glucose concentration," *Applied Physics B*, vol. B54, pp. 18-23, 1992.

[69] H. Mertens, K. N. Andersen, and W. E. Svendsen, "Optical loss analysis of silicon rich nitride waveguides," presented at ECOC 2002. 28th European Conference on Optical Communication, Copenhagen, Denmark, 2002.

[70] S. Sriram, W. D. Partlow, and C. S. Liu, "Low-loss optical waveguides using plasma-deposited silicon nitride," *Applied Optics*, vol. 22, pp. 26645, 1983.

[71] J. J. Lillie, M. A. Thomas, N.-M. Jokerst, S. E. Ralph, K. A. Dennis, and C. L. Henderson, "Multimode interferometric sensors on silicon optimized for fully integrated complementary-metal-oxide-semiconductor chemical-biological sensor

systems," *Journal of the Optical Society of America B: Optical Physics*, vol. 23, pp. 642, 2006.

[72] D. D. Kim, M. A. Brooke, N. M. Jokerst, J. J. Lillie, M. A. Thomas, and S. E. Ralph, "Data acquisition sensitivity determination of a sensor-on-a-chip integrated microsystem," presented at IEEE Sensors 2004, Vienna, Austria, 2004.

[73] D. D. Kim, M. A. Thomas, J. J. Lillie, K. S. Dennis, B. M. Comeau, M. A. Brooke, N. M. Jokerst, S. E. Ralph, and C. L. Henderson, "Integrated mixed-signal optoelectronic system-on-a-chip sensor," presented at IEEE International Symposium on Circuits and Systems (ISCAS), Kobe, Japan, 2005.

[74] H. Lang, H. D. Wolf, L. Korte, H. Hedrich, C. Hoyler, and C. Thanner, "GaAs/AlGaAs quantum well laser for high-speed applications," *IEE Proceedings J*, vol. 138, pp. 117-121, 1991.

[75] E. Yablonovitch, D. M. Hwang, T. J. Gmitter, L. T. Florez, and J. P. Harbison, "Van der Waals bonding of GaAs epitaxial liftoff films onto arbitrary substrates," *Applied Physics Letters*, vol. 56, pp. 2419, 1990.

[76] G. Chen, "Size and interface effects on thermal conductivity of superlattices and periodic thin-film structures," *Transactions of the ASME. Journal of Heat Transfer*, vol. 119, pp. 220, 1997.

[77] G. Chen, C. L. Tien, X. Wu, and J. S. Smith, "Thermal diffusivity measurement of GaAs/AlGaAs thin-film structures," *Transactions of the ASME. Journal of Heat Transfer*, vol. 116, pp. 325, 1994.

[78] R. P. Tye and A. Maesono, "Thermal properties evaluation of thin films, wafers and substrates," presented at Electronic Packaging Materials Science V. Symposium, Boston, MA, USA, 1991.

[79] A. Katsnelson, V. Tokranov, M. Yakimov, M. Lamberti, and S. Oktyabrsky, "Hybrid integration of III-V optoelectronic devices on Si platform using BCB," presented at Nano- and Microelectromechanical Systems (NEMS and MEMS) and Molecular Machines, Boston, MA, USA, 2003.

[80] A. Katsnelson, V. Tokranov, M. Yakimov, and S. Oktyabrsky, "Integration of III-V optoelectronic components on Si platform," presented at Materials, Integration and Packaging Issues for High-Frequency Devices Symposium, Boston, MA, USA, 2004.

[81] J. Piprek, H. Wenzel, and G. Sztefka, "Modeling thermal effects on the light vs. current characteristic of gain-guided vertical-cavity surface-emitting lasers," *IEEE Photonics Technology Letters*, vol. 6, pp. 139, 1994.

[82] "Advanced Laser Diode Simulator User Manual," Apollo, Inc., 2003, pp. 213.

[83] X. Li, A. D. Sadovnikov, W. P. Huang, and T. Makino, "A physics-based three-dimensional model for distributed feedback laser diodes," *IEEE Journal of Quantum Electronics*, vol. 34, pp. 1545, 1998.

[84] R. Bedford and M. Fallahi, "Analysis of high-reflectivity metal-dielectric mirrors for edge-emitting lasers," *Optics Letters*, vol. 29, pp. 1010, 2004.

[85] R. Bedford and M. Fallahi, "Metal/dielectric high-reflectivity facet coating for semiconductor lasers," presented at 2003 IEEE LEOS Annual Meeting, Tucson, AZ, USA, 2003.

[86] D. G. Cahill, H. E. Fischer, T. Klitsner, E. T. Swartz, and R. O. Pohl, "Thermal conductivity of thin films: measurements and understanding," *J. Vac. Sci. Technol. A*, vol. 7, pp. 1259, 1989.

[87] D. L. Decker, L. G. Koshigoe, and E. J. Ashley, "THERMAL PROPERTIES OF OPTICAL THIN FILM MATERIALS," *National Bureau of Standards, Special Publication*, pp. 291, 1986.

[88] J. C. Lambropoulos, S. D. Jacobs, S. J. Burns, L. Shaw-Klein, and S. S. Hwang, "Thermal conductivity of thin films. Measurement and microstructural effects," *American Society of Mechanical Engineers, Heat Transfer Division*, vol. 184, pp. 21, 1991.

[89] C. L. Tien and G. Chen, "Challenges in microscale conductive and radiative heat transfer," *Transactions of the ASME. Journal of Heat Transfer*, vol. 116, pp. 799, 1994.

[90] "Apollo Photonic Solutions Suite User Manual," Apollo, Inc., 2004, pp. 185.

[91] A. Aboudou, E. Goutain, J. P. Vilcot, M. Francois, L. Joannes, and D. Decoster, "Monolithic integration of GaAs MSM photodetector and SiO₂/Si₃N₄ dielectric optical waveguide," *Electronics Letters*, vol. 28, pp. 52, 1992.

[92] H. P. LeBlanc, J. B. D. Soole, A. Scherer, N. C. Andreadakis, C. Caneau, R. Bhat, and M. A. Koza, "Integration of InP grating-based DEMUX with p-i-n array for monolithic WDM detection," *Proceedings of the SPIE - The International Society for Optical Engineering*, vol. 1788, pp. 84, 1993.

[93] W. Lukosz, T. Brenner, V. Briguet, P. M. Nellen, and P. Zeller, "Output grating couplers on planar waveguides as integrated optical sensors," *Proceedings of the SPIE - The International Society for Optical Engineering*, vol. 1141, pp. 192, 1989.

[94] L. Lundqvist, J. Y. Andersson, Z. F. Paska, J. Borglind, and D. Haga, "Efficiency of grating coupled AlGaAs/GaAs quantum well infrared detectors," *Applied Physics Letters*, vol. 63, pp. 3361, 1993.

[95] H. Sakata, "Optimally designed layer formation for wavelength-selective photodetectors based on grating-assisted coupling," *Optical and Quantum Electronics*, vol. 28, pp. 1129, 1996.

[96] M. D. Watson, M. Abushagur, P. R. Ashley, and H. Johnson-Cole, "Polymer waveguide output coupler," *Proceedings of the SPIE - The International Society for Optical Engineering*, vol. 2532, pp. 131, 1995.

[97] M. T. Doan, C. F. Tsang, B. R. Murthy, B. Narayanan, C. Chang Kuo, S. Singh, K. P. Yap, and D. R. Lim, "Spot size mode converter for efficient coupling to SiN waveguides," *Proceedings of SPIE - The International Society for Optical Engineering*, vol. 5577, pp. 221, 2004.

[98] T. Mizuno, T. Kitoh, M. Itoh, T. Saida, T. Shibata, and Y. Hibino, "Optical spotsize converter using narrow laterally tapered waveguide for planar lightwave circuits," *Journal of Lightwave Technology*, vol. 22, pp. 833, 2004.

[99] I. Moerman, P. P. Van Daele, and P. M. Demeester, "A review on fabrication technologies for the monolithic integration of tapers with III-V semiconductor devices," *IEEE Journal of Selected Topics in Quantum Electronics*, vol. 3, pp. 1308, 1997.

[100] I. Moerman, G. Vermeire, M. D'Hondt, W. Vanderbauwhede, J. Blondelle, G. Coudenys, P. Van Daele, and P. Demeester, "III-V semiconductor waveguiding devices using adiabatic tapers," *Microelectronics Journal*, vol. 25, pp. 675, 1994.

[101] R. E. Smith, C. T. Sullivan, G. A. Vawter, G. R. Hadley, J. R. Wendt, M. B. Snipes, and J. F. Klem, "Reduced coupling loss using a tapered-rib adiabatic-following fiber coupler," *IEEE Photonics Technology Letters*, vol. 8, pp. 1052, 1996.

[102] G. A. Vawter, T. Bakke, S. Mukherjee, and C. Sullivan, "Adiabatic mode converters for photonic integrated circuits and devices," *Proceedings of SPIE - The International Society for Optical Engineering*, vol. 5355, pp. 129, 2004.

[103] D. K. Johnstone, "Thermal management in optoelectronics," *International Journal of High Speed Electronics and Systems*, vol. 12, pp. 501, 2002.

[104] C. D. Knighton and G. Estep, "Optimize thermoelectric coolers to improve system performance," *Laser Focus World*, vol. 31, pp. 8, 1995.

[105] C. LaBounty, A. Shakouri, P. Abraham, and J. E. Bowers, "Integrated cooling for optoelectronic devices," *Proceedings of SPIE - The International Society for Optical Engineering*, vol. 3950, pp. 69, 2000.

[106] C. LaBounty, A. Shakouri, P. Abraham, and J. E. Bowers, "Monolithic integration of thin-film coolers with optoelectronic devices," *Optical Engineering*, vol. 39, pp. 2847, 2000.

[107] R. Srinivasan, R. Miller, K. Kuppuswamy, T. Nguyen, Y. Hu, H. Li, D. Brown, T. Towe, T. Crum, B. Morris, E. Wolak, and J. Harrison, "Next-generation active and passive heatsink design for diode lasers," *Proceedings of SPIE - The International Society for Optical Engineering*, vol. 6456, pp. 64561, 2007.

VITA

Mikkel Andrey Thomas received the Bachelor of Science in Electrical Engineering and the Masters of Science in Electrical Engineering from the Georgia Institute of Technology, Atlanta, Georgia in 1997 and 1999 respectively. During that time, he worked at AT&T Labs – Research as an intern concentrating on short haul fiber optic networks. He received an NSF Fellowship and an AT&T Labs - Research Fellowship in 1998. He is a member of the Institute of Electrical and Electronics Engineers (IEEE) and the Lasers and Electro-Optics Society (LEOS)